STACKING UV-SELECTED LYMAN-BREAK GALAXIES IN THE ALMA FRONTIER FIELDS

Rodrigo Alonso Carvajal Pizarro

PONTIFICIA
UNIVERSIDAD
CATÓLICA
DE CHILE

FACULTAD DE FÍSICA
INSTITUTO DE ASTROFÍSICA

STACKING UV-SELECTED LYMAN-BREAK GALAXIES IN THE ALMA FRONTIER FIELDS

BY

RODRIGO ALONSO CARVAJAL PIZARRO

Thesis submitted to the Faculty of Physics at
Pontificia Universidad Católica de Chile in partial fulfillment
of the requirements for the degree of Master of Science in Astrophysics

Thesis Advisor

FRANZ E. BAUER

Santiago de Chile, March 2019

© MMXIX, RODRIGO CARVAJAL

Se autoriza la reproducción total o parcial, con fines académicos, por cualquier medio o procedimiento, incluyendo la cita bibliográfica del documento.

PONTIFICIA
UNIVERSIDAD
CATÓLICA
DE CHILE

FACULTAD DE FÍSICA

INSTITUTO DE ASTROFÍSICA

STACKING UV-SELECTED LYMAN-BREAK GALAXIES IN THE ALMA FRONTIER FIELDS

BY

RODRIGO ALONSO CARVAJAL PIZARRO

Members of the Committee

FRANZ E. BAUER	(IA - PUC)
EZEQUIEL TREISTER	(IA - PUC)
L. FELIPE BARRIENTOS	(IA - PUC)

Santiago de Chile, March 2019

© MMXIX, RODRIGO CARVAJAL

When I heard the learn'd astronomer,
When the proofs, the figures, were ranged in columns before me,
When I was shown the charts and diagrams, to add, divide, and measure them,
When I sitting heard the astronomer where he lectured with much applause in the lecture-room,
How soon unaccountable I became tired and sick,
Till rising and gliding out I wander'd off by myself,
In the mystical moist night-air, and from time to time,
Look'd up in perfect silence at the stars.

Walt Whitman - When I heard the Learn'd Astronomer - Leaves of Grass

ACKNOWLEDGEMENTS

Arriving to this point in my career (and life, in a broader sense) did not lack for obstacles but many people have helped me in different ways to reach it and will surely be part of what is yet to come.

In first place, Franz Bauer, my advisor, helped and supported me during all these years at PUC. Witouth his unrivalled patience and lucid explanations, I would have not completed this work successfully. This extends to Jorge-González-López from UDP and Rychard Bouwens from Leiden University, who helped us to finish this thesis satisfactorily.

In an equivalent degree, I would like to acknowledge my family, and specially my mother, for being there whenever I wanted. Dealing with me everyday must be recognized as a very demanding task. I am thankful for all the efforts and good moments.

Equally, Fernanda, my partner and best friend for the last and best years of my life. Probably nothing would have happened without her firm –yet full of love– encouragement. I thank her for putting many of her troubles and worries aside during these last months to avoid distressing me. I will surely recompense her forbearance.

My fellow students at PUC have also helped me to achieve this goal. In no particular order, Jonathan, Diego, Gergely, Felipe, Katerine, Lucie, Ignacio, Camila, and Camila made me look many issues from a different perspective as well as *sparked joy* in some blue moments.

In the same manner, I would like to thank the presence of all the people at IA who helped in some degree to make these years even more fruitful that they would have been without them.

We acknowledge support from CONICYT-Chile grants Basal-CATA PFB-06/2007 and AFB-170002, FONDECYT Regular 1141218, and from VRI Internationalization grant.

This thesis makes use of the following ALMA data: ADS/JAO.ALMA#2013.1.00999.S, ADS/JAO.ALMA#2015.1.01425.S. ALMA is a partnership of ESO (representing its member

states), NSF (USA) and NINS (Japan), together with NRC (Canada), NSC and ASIAA (Taiwan), and KASI (Republic of Korea), in cooperation with the Republic of Chile. The Joint ALMA Observatory is operated by ESO, AUI/NRAO and NAOJ.

Part of this work is based on observations obtained with the NASA/ESA Hubble Space Telescope, retrieved from the Mikulski Archive for Space Telescopes (MAST) at the Space Telescope Science Institute (STScI). STScI is operated by the Association of Universities for Research in Astronomy, Inc. under NASA contract NAS 5-26555.

This work utilizes gravitational lensing models produced by PIs Bradač, Natarajan & Kneib (CATS), Merten & Zitrin, Sharon, Williams, Keeton, Bernstein and Diego, and the GLAFIC group. This lens modeling was partially funded by the HST Frontier Fields program conducted by STScI. STScI is operated by the Association of Universities for Research in Astronomy, Inc. under NASA contract NAS 5-26555. The lens models were obtained from the MAST.

This research made use of `Astropy`, a community-developed core `Python` package for Astronomy (Astropy Collaboration et al., 2013), `matplotlib`, a `Python` library for publication quality graphics (Hunter, 2007), `APLpy`, an open-source plotting package for `Python` (Robitaille and Bressert, 2012) and NASA's Astrophysics Data System.

CONTENTS

LIST OF TABLES ix

LIST OF FIGURES x

1 INTRODUCTION 1

2 DATA AND DERIVED QUANTITIES 10

2.1 ALMA data 10

2.2 ALMA Stacking Considerations 12

2.3 LBG candidates 17

2.4 Photometric redshifts 18

2.5 Magnification factors 19

2.6 UV-continuum slope 21

2.7 Stellar Mass 23

2.8 (Specific) Star Formation Rates 25

2.9 ALMA primary-beam corrections 27

2.10 ALMA peak fluxes 28

2.11 UV Luminosities 31

2.12 IR Luminosities 32

2.13 IRX relations 33

3 METHODS 36

3.1 ALMA image retrieval 36

3.2 Target final sample 38

3.3 Stacking 39

4 RESULTS **45**

4.1 Individual results 45

4.1.1 Individual ALMA peak fluxes 45

4.1.2 Individual UV and IR luminosities 48

4.1.3 Individual IRX-β relation 50

4.1.4 Individual IRX-$M_\star$ relation 53

4.2 Stacking results 53

4.2.1 Detected LBGs Stacking 55

4.2.2 Upper Limits ALMA Stacking 57

4.2.3 Stacked IRX-β relation 60

4.2.4 Stacked IRX-M$_\star$ relation 62

5 DISCUSSION **63**

5.1 Individual constraints 63

5.1.1 Detected LBGs 64

5.1.2 Upper Limits and previous works 64

IRX-β and previous results 64

IRX-$M_\star$ and previous results 66

5.1.3 $M_\star$-β correlation 68

5.1.4 Candidates with $\log(M_\star/M_\odot) < 6.0$ 69

5.2 Stacked properties 70

5.2.1 Considerations on stacking weighting 70

5.3 LBG density 72

6 CONCLUSIONS **73**

APPENDICES **88**

A Stacking Results **89**

A.1 UV slope binning 89

A.2 Stellar mass binning 89

B Individual Properties **100**

C Detected LBG Candidates **105**

LIST OF TABLES

2.1 ALMA Properties of observed clusters 11

3.1 LBG Candidate Selection Criteria 40

4.1 Properties for detected LBG candidates 46
4.2 uv-stacking for detected LBGs 55

A.1 uv-stacking results with UV-slope and redshift bins 90
A.2 uv-stacking results with mid-stellar mass and redshift bins 93
A.3 uv-stacking results with high-stellar mass and redshift bins 96
A.4 Properties of low stellar mass stacked LBG candidates 99

B.1 HST photometry from LBG candidates 101
B.2 ALMA properties from LBG candidates 102
B.3 Derived properties from LBG candidates 103
B.4 FAST properties from LBG candidates 104
B.5 Luminosities from LBG candidates 104

LIST OF FIGURES

1.1 LBG SED example 7

2.1 ALMA image of A370 with LBG candidates 12
2.2 ALMA image of A2744 with LBG candidates 13
2.3 ALMA image of AS1063 with LBG candidates 14
2.4 ALMA image of MACSJ0416 with LBG candidates 15
2.5 ALMA image of MACSJ1149 with LBG candidates 16
2.6 Comparison of photometric redshifts between `EAZY` and `BPZ` 20
2.7 Distribution of luminosity distances 21
2.8 Distribution of magnification factors 22
2.9 UV-slopes vs. UV magnitudes 24
2.10 Distribution of β values 25
2.11 Distribution of stellar mass 26
2.12 Distribution of star formation rates 27
2.13 Distribution of intrinsic star formation rates 28
2.14 False detection rate for ALMA maps 30

3.1 Selection of LBG candidates in UV-slope and redshift 43
3.2 Selection of LBG candidates in stellar mass and redshift 44

4.1 Distribution of peak SNR 47
4.2 Distribution of mean SNR 48
4.3 Distribution of ALMA peak fluxes 49
4.4 Distribution of UV luminosities 50
4.5 Distribution of IR luminosities 51

4.6 Infrared excess vs. UV-slope 52
4.7 Infrared excess vs. stellar mass 54
4.8 ALMA uv-stacked LBG detections 56
4.9 Example uv-stacked LBG candidates in UV-slope bins 58
4.10 Example uv-stacked LBG candidates in stellar mass bins 59
4.11 Stacked infrared excess ratios vs. UV-slope 61
4.12 Stacked infrared excess ratios vs. stellar mass 62

5.1 UV-slope vs. stellar mass for the studied sample 68
5.2 UV fluxes vs. UV luminosities of LBG candidates 71

C.1 Detected LBG candidates 106

ABSTRACT

The Frontier Fields offer an exceptionally deep window into the high-redshift universe; covering a substantially larger area than the Hubble Ultra-Deep field at low magnification and probing 1–2 mags deeper in exceptional high magnification regions. This unique parameter space, coupled with the exceptional multi-wavelength ancillary data, can allow useful insights into distant galaxy populations.

We leverage ALMA band 6 ($\approx$263 GHz) mosaics in the central portions of five Frontier Fields to characterise the IR properties of 1821 UV-selected Lyman-Break Galaxies (LBGs) at redshifts of $z\sim$2–8. We investigate individual and stacked fluxes and infrared excess (IRX) values of the LBG sample functions of stellar mass, redshift, UV luminosity, and lensing magnification.

LBG samples are color-selected based on *HST* photometry, with photometric redshift confirmation. Using SED-templates, we obtain luminosities, stellar masses and star formation rates for our LBG samples. From the ALMA images, we obtain individual fluxes and IRX estimates, as well as stacked averages from image and *uv*-stacking of the ALMA visibilities.

Three LBGs are individually detected above a significance of 4.1$-\sigma$, while stacked samples of the remaining LBGs yield no significant detections. We investigate our detections and upper limits in the context of the IRX vs. stellar mass and IRX vs. UV slope β relations. Our upper limits help to exclude large portions of parameter space, which may be useful for modeling purposes. For a handful of cases, our limits are sufficiently deep to create mild tension with the typically assumed consensus relations.

Keywords: high-redshift galaxies, submillimetre galaxies, galaxy clusters.

RESUMEN

Los campos *Frontier Fields* (FF) ofrecen una ventana inusualmente profunda hacia el universo de alto corrimiento al rojo. Lo logran cubriendo un área sustancialmente más grande que el campo *Hubble Ultra-Deep*, que posee baja magnificación, sondeando 1–2 magnitudes más profundas en regiones con magnificaciones singularmente más altas. Este espacio de parámetros único, junto con excepcionales datos en múltiples longitudes de onda, permiten una mejor comprensión de las poblaciones de galaxias distantes.

Se obtuvieron mosaicos en la banda 6 de ALMA ($\approx$263 GHz) en las porciones centrales de cinco campos FF para caracterizar las propiedades infrarrojas de 1821 *Lyman-Break Galaxies* (LBG), con corrimientos al rojo de $z\sim$2–8, seleccionadas a través de observaciones en el ultravioleta. Investigamos flujos y excesos infrarrojos (*IRX*) tanto individuales como acumulados para la muestra de LBG en función de masas estelares, corrimientos al rojo, luminosidades ultravioleta y magnificaciones por lentes gravitacionales.

Las muestras de LBG se han escogido con base en fotometría realizada con *HST* y confirmación fotométrica de corrimiento al rojo. Con plantillas de distribución espectral de energía (*SED*), obtenemos luminosidades, masas estelares y tasas de formación estelar para nuestros LBG. De las imágenes de ALMA, obtenemos flujos individuales y estimaciones de IRX así como valores medios de los cálculos acumulados en imágenes y visibilidades de ALMA.

Tres LBG son detectados, individualmente, sobre un nivel de significancia de 4,1$-\sigma$, mientras las muestras acumuladas de los restantes LBG no entregan valores relevantes. Investigamos nuestras detecciones y límites superiores en el contexto de las relaciones entre IRX y masa estelar y entre IRX y la pendiente ultravioleta (β). Nuestros límites superiores ayudan a excluir grandes porciones del espacio de parámetros, lo que puede ser útil para modelización. En ciertos casos, nuestros límites son suficientemente profundos para crear una leve tensión con las, típicamente asumidas, relaciones de consenso en la literatura.

Palabras Clave: galaxias de alto corrimiento al rojo, galaxias submilimétricas, cúmulos de galaxias.

1

Introduction

A fundamental goal of modern astrophysics is to understand the conditions that led to the formation of the first galaxies in the early Universe. One way to attain this is via the direct study of the earliest galaxies we can observe with our current technology.

It has been suggested that early star-forming galaxies are predominantly responsible for a large fraction of the reionization of intergalactic hydrogen. Therefore, it is relevant to understand, as much as possible, the properties of these galaxies. Among these properties, the growth of galaxies and their energy production are two of the most relevant since they are directly related to the extent of the influence of galaxies on the overall intergalactic reionization.

Obtaining information from these galaxies is not an easy task. Many obstacles arise from their large distances and subsequent faint fluxes. Since their light has to travel immense distances, any information might become dimmer due to all the intervening elements on their path to us and because of the cosmological effects of observing objects at very high redshifts.

Intervening systems along the line-of-sight, predominantly comprised of hydrogen clouds, absorb photons with wavelengths close to that of the 912Å Lyman-α lines –transitions around the ground state of hydrogen–. The farther away galaxies are, the more intervening clouds can be present between them and the observer. Since these clouds are located at different redshifts, Lyman absorption may be observed at wavelengths blueward of 912Å in the rest-frame spectrum of the galaxy.

Such Lyman absorption features can be of great help to determine the high-redshift nature of star-forming galaxies. If a galaxy shows these features, it is likely to lie at high redshift.

Successive absorption features will be superimposed and, consequently, a prominent trough could be detected –it can be as extreme as to show no emission whatsoever–. This trough is called the Lyman Break or ultraviolet (UV) drop (see an example of this break in Fig 1.1). Galaxies where this broad spectral feature is observed, generally as a strong change between photometric bands, are known as Lyman-Break Galaxies (LBGs)

The wavelength at which this spectrum discontinuity occurs allows astronomers to establish a rough redshift estimate for the observed galaxy.

Occasionally, in higher redshift galaxies –z~5–6 and beyond (Dunlop, 2013)–, Lyman-α absorption can be strong enough to impact the continuum between rest-frame wavelengths of 1216Å (which is part of the Lyman Series as well) and 912Å, and suppress all the light from the galaxy at $\lambda < 1216$Å. This secondary break becomes the dominant feature when considering LBGs at higher redshifts.

Apart from intervening clouds, the break –the rise of emission at 912Å– is produced by the ionization energy of the hydrogen atom in the ground state inside the galaxy. Since high-redshift galaxies are expected to be a source of reionization, this feature should be strong when studying their UV spectra (Giavalisco, 2002; Pelló, 2016; Dunlop, 2013). This Lyman Continuum –LyC– radiation, released from young star-forming regions within galaxies, ionizes their intergalactic surroundings (Stark, 2016). In this way, and in absence of significant quantities of dust, star-forming galaxies will have blue continuum spectra, powered by massive O and B stars.

To fully study distant LBGs, particularly in the face of potential dust obscuration, multi-wavelength observations are generally needed. Acquiring these can be a challenge due to the large distances and, consequently, faint observed magnitudes of LBGs. The initial approach of combining deep optical and UV imaging, for instance, allowed estimates of the observed (i.e., unobscured) properties of LBGs. First results were obtained using observations of star-forming galaxies in the range $2.3 \leq z \leq 3.4$ from the *Hubble* Deep Field (HDF; Steidel, Giavalisco, Dickinson, et al., 1996; Steidel, Adelberger, et al., 1999; Shapley et al., 2003) and with observations of selected z~3 galaxies observed with the United Kingdom In-

frared Telescope (UKIRT), Keck and the Very Large Telescope (VLT) (Pettini, Kellogg, et al., 1998; Pettini, Shapley, et al., 2001). Later observations were performed with *HST*'s Wide Field Camera 3 (WFC3) –e.g. $z\sim7$ and $z\sim8$ galaxies in the *Hubble* Ultra Deep Field, HUDF, in Bouwens, Illingworth, Oesch, Labbé, Trenti, et al. (2011)–. In general terms, the installation of the WFC3 in *HST* in 2009 led to the identification of many faint star-forming galaxies in the range $6 < z < 9$. To assess the obscured attributes of galaxies, however, infrared observations are essential, but until recently, have not allowed us to reach relevant spatial and spectral resolutions.

One instrument which has allowed observations at infrared –specifically mid-infrared (MIR)– wavelengths is the Multiband Imaging Photometer for Spitzer (MIPS). It was in use in Spitzer Space Telescope from 2003 until 2009, and equipped with detectors at 24μm, 70μm and 160μm. The 24μm channel was the most sensitive and enabled various large legacy survey observations (i.e., sky regions that have been extensively observed by a variety of telescopes). Selection of MIR sources is more complex than in other wavelengths since the rest-frame 24μm emission is dominated by hot dust and various strong emission and absorption line features, compared to smoother spectra at longer wavelengths from canonically colder dust. This can lead to apparent discrepancies in the properties derived from MIR observations and those from other wavelengths –For a review, see Casey, Narayanan, et al. (2014)–. A few notable early studies that used MIPS data were Le Floc'h et al. (2005) and Bell et al. (2005), who analyzed around 2600 MIPS 24μm sources in the Chandra Deep Field-South (CDF-S) up to $z\sim1$. The observations were able to characterize Luminous and Ultraluminous IR Galaxies (LIRGs and ULIRGs, respectively) with a Star Formation Rate (SFR) $\gtrsim3M_{\odot}yr^{-1}$. Observations in the mid-IR wavelengths can be extremely useful to complement multi-band studies. One example that retrieves data from MIPS was that of Reddy, Steidel, Fadda, et al. (2006), who examined more than 200 $z\sim2$ spectroscopically identified, optically selected LBGs in the GOODS-N field at 8μJy depths, using the Using 24μm observations as an independent probe of dust extinction in this strongly star-forming population.

For far-infrared and submillimeter observations of galaxies, key progress was made

thanks to the use of *Herschel* Space Observatory. The Spectral and Photometric Imaging Receiver (SPIRE) and Photodetector Array Camera and Spectrometer (PACS) allowed observations in bands at 250μm, 350μm and 500μm for SPIRE and at 70μm, 100μm and 160μm for PACS. These bands cover the peak of the redshifted thermal Spectral Energy Distribution (SED) of interstellar dust. *Herschel* enabled a new era for studies of high-redshift sources, since it enabled high-quality observations of dust-related features from them. One large sample of extragalactic sources was produced by Oliver et al. (2012), who retrieved information from more than 100 000 galaxies as part of the legacy (*Herschel* Multi-tiered Extragalactic Survey (HerMES) using data from SPIRE and PACS.

While Spitzer and *Herschel* both provided fundamental insight into high-redshift star-forming galaxies, their designs and technical capabilities were generally insufficient to reach very faint sources in very early epochs. For example, *Herschel* SPIRE hits the confusion limits around ~5mJy due to its large beam (e.g. Oliver et al., 2012).

A key source of uncertainty in the observations of such early galaxies is related to interstellar extinction from the host galaxy. This extinction can affect the determination of important galactic properties such as the SFR. To assess SFRs in galaxies, we must account for extinction by gas and dust in order to extract the intrinsic amount of the UV light emitted by the underlying stellar population. Deep near-infrared, optical and UV surveys now routinely allow us to estimate unobscured SFRs down to a few $M_{\odot}\,\mathrm{yr}^{-1}$ in galaxies at z~6–10 (e.g., Bouwens, Illingworth, Oesch, Trenti, et al., 2015; McLeod et al., 2016; Santini et al., 2017; Oesch et al., 2018). A straightforward way to measure the extinction from these sources is to estimate the steepness of their UV spectra (e.g., Bouwens, Illingworth, Oesch, Franx, et al., 2012; Bouwens, Illingworth, Oesch, Labbé, van Dokkum, et al., 2014), generally characterized by fitting a power law, $f_{\lambda}\sim\lambda^{\beta}$, to two or more rest-frame UV bands depending on the available observations. A synthetic stellar population with solar metallicity and an age of $\gtrsim$100 Myr should have intrinsic β (slope) values in the range of ~ -2.0 to -2.2. Redward –higher β– deviations from the mentioned values should relate to the amount of dust extinction, or reddening, and scattering that light from massive stars suffers after its emission. Blueward

(lower β; e.g., $\beta\sim-3$) deviations likely imply a very young and/or metal-deficient stellar population (e.g., Heap, 2012; Stark, 2016).The SFR itself does not play a major role in the deviations of β from the standard LBG values since, as the UV spectrum is produced by massive O and B stars, their contribution is considered "instantaneous" and does not constrain the past history of star growth.

Detailed spectroscopic observations are generally required to break degeneracies between extinction, stellar age, and metallicity (e.g., Stark et al., 2013), all of which ultimately contribute to the observed stellar flux slope β. However, for fainter and/or more distant galaxies, this remains quite challenging (e.g., Laporte et al., 2017; Bowler, McLure, et al., 2017; Hoag et al., 2018; Hashimoto et al., 2018). Such degeneracies become particularly problematic at high redshifts, where the likelihood of young, metal-poor stellar populations, and hence the uncertainties, are largest (e.g., Anders and Fritze-v. Alvensleben, 2003; Schaerer and de Barros, 2009; Eldridge et al., 2017).

A second approach to assess extinction, as well as to examine the potential for either highly or completely obscured regions of star formation, is to measure the rest-frame infrared luminosity. Until recently, such observations were strongly limited in sensitivity and/or spatial and spectral resolution, effectively only probing down to SFRs of $\sim$10–100 $M_\odot\,\mathrm{yr}^{-1}$ at $z\sim$1–2 (e.g., Magnelli et al., 2013). The materialization of ALMA, with its large collecting area and high spatial resolution capabilities, now provides the opportunity to narrow considerably the SFR gap between the UV/optical and FIR/mm bands for galaxies across a large redshift range, and hence make a fair comparison between the obscured and visible light that is being generated. These high-resolution observations might exhibit relevant spectral features at FIR/mm frequencies in the observed frame –i.e. after being redshifted–, such as [CII] and CO, which, if strong enough, can bypass the need for optical/UV spectroscopic observations to confirm the presence of high-redshift galaxies.

Numerous observational studies of $z\gtrsim1$ star-forming galaxies have been made over the years, comparing the above two approaches to well-known $z\sim0$ correlations (e.g., Meurer et al., 1999, hereafter M99; Reddy, Steidel, Fadda, et al., 2006; Bouwens, Illingworth, Franx, et al.,

2009; Bouwens, Aravena, et al., 2016, hereafter B16; Boquien et al., 2012; Capak et al., 2015; Álvarez-Márquez et al., 2016; McLure et al., 2018; Koprowski et al., 2018). Many observers have focused on the relationships between the so-called 'infrared excess' (IRX$\equiv L_{\rm IR}/L_{\rm UV}$) and UV-continuum slope or stellar mass ($M_\star$); such relations are often invoked to make dust extinction corrections out to high redshifts. Most critically, while such correlations appear to be confirmed out to $z\sim$1–2, based on a variety of multi-wavelength data (Reddy, Steidel, Fadda, et al., 2006; Reddy, Steidel, Pettini, et al., 2008; Reddy, Erb, et al., 2010; Daddi, Dickinson, et al., 2007; Daddi, Alexander, et al., 2007; Pannella et al., 2009), it remains unclear how applicable they are at earlier times (e.g., Bouwens, Aravena, et al., 2016).

To generate large samples of high-redshift star-forming LBGs, we can make use of their most recognizable feature: the UV drop. The most precise method to measure the UV drop consists of obtaining a UV spectrum of the studied object to search for a discontinuity at either 912Å or 1216Å in rest-frame wavelength –the value depending on the redshift of the object– . However, for remote objects, this is highly impractical since obtaining such information would require excessively long exposure times with very sensitive instruments.

A less expensive approach to detect LBGs is the so-called 'drop-out' technique. Here, at least three distinct photometric band observations are needed for each LBG candidate. Two filters are used to detect the flux difference –the break– and the third one allows confirmation of the spectral slope redward of the break. This technique needs less observation time than obtaining a full spectrum for every LBG candidate. This method was utilized successfully for the first time by Steidel, Giavalisco, Pettini, et al. (1996) and Steidel, Giavalisco, Dickinson, et al. (1996). Given its simplicity, it has been used extensively over the last two decades with observations in both narrow and wide fields. In Fig. 1.1, an example SED of an LBG has been plotted along with some *HST* filters to show how differences in the flux in each band can lead to the detection of LBGs. In this case, the flux rise is strongly detected with the filter F435W, redward of the rest-frame wavelength of 912Å.

For redshift values above $z\sim$6, it becomes more laborious to obtain useful observations of LBGs. At these values, Lyman-α absorption attenuates light below 1.2μm meaning that

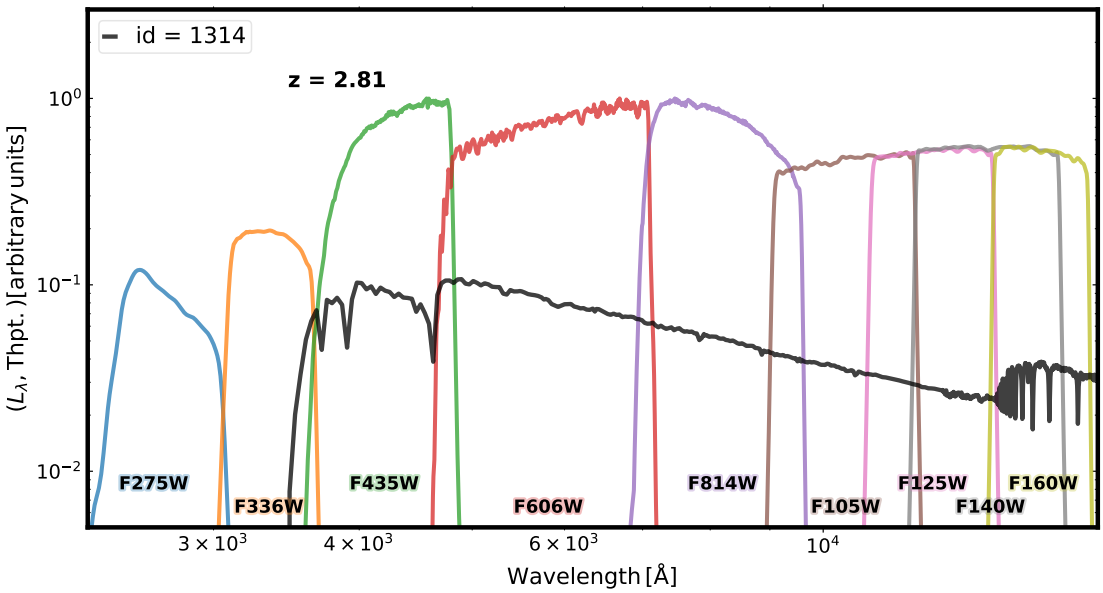

Figure 1.1: In black, example Spectral Energy Distribution (SED) for a model LBG at redshift $z = 2.81$, in units of luminosity. In colors, the transmission curves –throughput– from the HST filters used for this work (see §2.3) with their respective names.

only one *HST* filter –F160W, also called H_{160}– is left with enough information to detect the galaxies. From that point, observations with ground-based near-infrared instruments (e.g., using K and medium band filters) or space-based MIR instruments (e.g., Spitzer/IRAC) are necessary to constrain the flux properties from the LBG candidates. However, the limited spectral coverage and poorer spatial resolution and leads to larger photometric uncertainties and higher potential for contamination from, e.g., brown dwarfs.

To obtain a large sample of LBGs spanning a broad range of redshifts, luminosities and positions requires observations of large areas of the sky observed with an adequate number of independent photometric bands. Such task is, with no doubt, demanding. One manner to address this problem is using legacy field survey observations. Archive data can alleviate the need for multiple observations from a particular area of the sky.

With fields covering large areas in the sky, and given the advantages mentioned above, a positive feedback loop can occur. Since these large regions have been selected for extensive

study, more interest is drawn to them. As a consequence, more analyses are performed which contribute with more observations in different wavelengths of the same area. From this, studying large fields conveys advantages that cannot be easily established with other areas of the sky.

One such legacy survey is the Frontier Fields (FFs)[1], which corresponds to a series of six $3' \times 3'$ fields which harbor one massive galaxy cluster each (as well as accompanying adjacent parallel fields). They were initially observed as *Hubble* (*Hubble* Frontier Fields, HFF[2], PI. J. Lotz) and *Spitzer* Space Telescope Director's discretionary campaigns. A key selling point is the large area of high magnification –from strong gravitational lensing effects– and a large number of member galaxies in each field. These clusters were chosen to form part of the FF survey after a selection process that took into account different cluster properties such as lensing power, sky brightness, galactic extinction, and –space and ground-based– observability (Coe et al., 2015; Lotz et al., 2017). In this work, we study five of the six fields –detailed information in §2–. These fields have since been observed across the full electromagnetic spectrum with, e.g. *Chandra*, VLT/MUSE, JVLA (Karl G. Jansky Very Large Array) and, of particular relevance here, ALMA.

In interferometric radio astronomy observations, the coordinates in the visibility plane (u, v, w) –uv-plane, for short– correspond to a convenient transformation of the spatial coordinates –hour angles and declinations– which trace the movement of a specific antenna, part of an interferometric array, when observing a sky source (cf. §4.1; Thompson et al., 2017, and references therein). Then, the interferometer measures the interference pattern –delays– between the antennas. This pattern is related to the source brightness, since measured visibility corresponds to the Fourier transform of the brightness on the sky, which is the quantity we can retrieve applying deconvolution algorithms.

Even though ALMA offers some of the best observing capabilities to date, high-redshift LBGs have low submm/mm fluxes which can be difficult to detect. In order to obtain higher

[1] `https://frontierfields.org`

[2] `http://www.stsci.edu/hst/campaigns/frontier-fields/`

quality or higher sensitivity data from them, we employ stacking, which consists of adding up several images of the same object –or different objects if that is the case– to, statistically, reduce their noise levels and increase the quality of their signal. This allows the study of the average properties of objects well below the noise limits of individual observations. As with other interferometric instruments, the process of deconvolution and image retrieval from ALMA observations can add some extra noise to the images. For this reason, we adopt a new method to stack observations in the uv-plane; uv-stacking. It allows the stacking of data before obtaining images from ALMA observations, reducing the number of error sources and, ultimately, increasing the stacked image quality (see §3.3).

The goal of the work presented here is to characterize the infrared emission –individually and as stacked-averages– for robust samples of LBG candidates at $z\sim2-8$ found in the Frontier Fields survey. This is intended to be done via fitting SED template models to our photometry and, from this, obtain some of their properties, such as stellar mass and star formation rates. We also aim to combine the data from all our LBG targets to enhance the values we can obtain from ALMA and, statistically, try to understand the correlation, if any, between the infrared and ultraviolet emission they exhibit and compare them with relations which have been previously developed from $z\sim0$ objects.

This thesis is structured as follows. In §2, we describe the ALMA FFs observations, the LBG candidates and their derived properties. In §3, we discuss the selection criteria we applied to our candidates and the stacking procedures we utilized –ALMA image stacking and IRX stacking–. In §4, we present the individual properties that we obtain for our sample, as well as the stacked values for luminosities and IRXs. §5 provides a comparison of our results with previously published works, as well as results not covered fully in preceding sections. Finally, we summarize our work and present our conclusions in §6. Unless otherwise stated, throughout this work we assumed a cosmology with $H_0 = 70$ km s^{-1} Mpc^{-1}, $\Omega_m = 0.3$ and $\Omega_\Lambda = 0.7$.

2

Data and Derived Quantities

2.1 ALMA data

The inner ~2′×2′ regions of the FFs, centered on the massive clusters to benefit most strongly from the boost from gravitational lensing, were observed in band 6 (1.14mm) by ALMA through two projects, 2013.1.00999.S (PI Bauer; cycle 2) and 2015.1.01425.S (PI Bauer; cycle 3). Although all six FFs clusters were observed, only five were considered completed by ALMA and thus used here. These include, from cycle 2, Abell 2744, MACSJ0416.1−2403 and MACSJ1149.5+2223 observed in 2014 and 2015 (hereafter A2744, MACSJ0416, and MACSJ1149, respectively) and, from cycle 3, Abell 370 and Abell S1063 —also designed as RXJ2248−4431— observed in 2016 (hereafter A370 and AS1063, respectively). As stated in González-López, Bauer, Aravena, et al. (2017), MACSJ0717.5+3745 was only partially observed –just 1 out of 9 planned executions– and, given its substantially worse sensitivity and calibration, is not useful for this work.

The mosaic data were reduced and calibrated using the Common Astronomy Software Applications (CASA v4.2.2; McMullin et al. 2007)[1]; details can be found in González-López, Bauer, Romero-Cañizales, et al. (2017). Automatic reduction with the CASA-generated pipelines for A2744 and MACSJ1149 presented problems, and hence manual and ad-hoc pipelines were used to reduce the data. For MACSJ0416, A370, and AS1063, the CASA-generated pipelines worked smoothly and were, thus, used. CASA was also used to image the mosaic data, adopting both natural and taper weightings in `CLEAN` (see §3). This resulted in

[1] `https://casa.nrao.edu`

Table 2.1: ALMA Properties of observed clusters. Positions correspond to the mosaic centers. Major and minor axes of synthesized beam, in arcseconds.

Cluster Name	R.A. [J2000] [hh:mm:ss.s]	Dec. [J2000] [±dd:mm:ss.s]	z	Observation Date Range	rms [μJy]	$b_{\rm max} \times b_{\rm min}$ [$''\times''$]
Abell 2744	00:14:21.2	-30:23:50.1	0.308	29-Jun-2014/31-Dec-2014	55	0.63×0.49
Abell 370	02:39:52.9	-01:34:36.5	0.375	05-Jan-2016/17-Jan-2016	61	1.25×0.99
Abell S1063	22:48:44.4	-44:31:48.8	0.348	16-Jan-2016/02-Apr-2016	67	0.96×0.79
MACSJ0416.1-2403	04:16:08.9	-24:04:28.7	0.396	04-Jan-2015/02-May-2015	59	1.52×0.85
MACSJ1149.5+2223	11:49:36.3	+22:23:58.1	0.543	14-Jan-2015/22-Apr-2015	71	1.22×1.08

natural-weight rms[2] errors of 55, 61, 67, 59 and 71 μJy beam^{-1} for FFs A2744, A370, AS1063, MACSJ0416 and MACSJ1149, respectively. The resulting maps have relatively uniform rms properties over the central regions, but exhibit strong attenuation at the edges due to the effects of the primary beam. For the purposes of this work, we limit our analysis to regions of each mosaic with a primary beam correction factor, `pb_cor`, above 0.5. However, portions of the MACSJ0416 and MACSJ1149 mosaics exhibit rms variations by as much as ∼15–20% (for details, see §2.4 and Fig. 4 of González-López, Bauer, Romero-Cañizales, et al., 2017). These variations are captured in the `pb_cor` values used to weight individual sources in our stacking procedure (see §3.3).

Some basic properties of each dataset, including central position, are listed on Table 2.1. ALMA maps from our five clusters are shown, along with our selected LBG candidates and outlines for the magnification maps in Figs. 2.1, 2.2, 2.3, 2.4, 2.5.

[2]rms defined as $\sqrt{\sum_i \left(x_i^2\right)}$

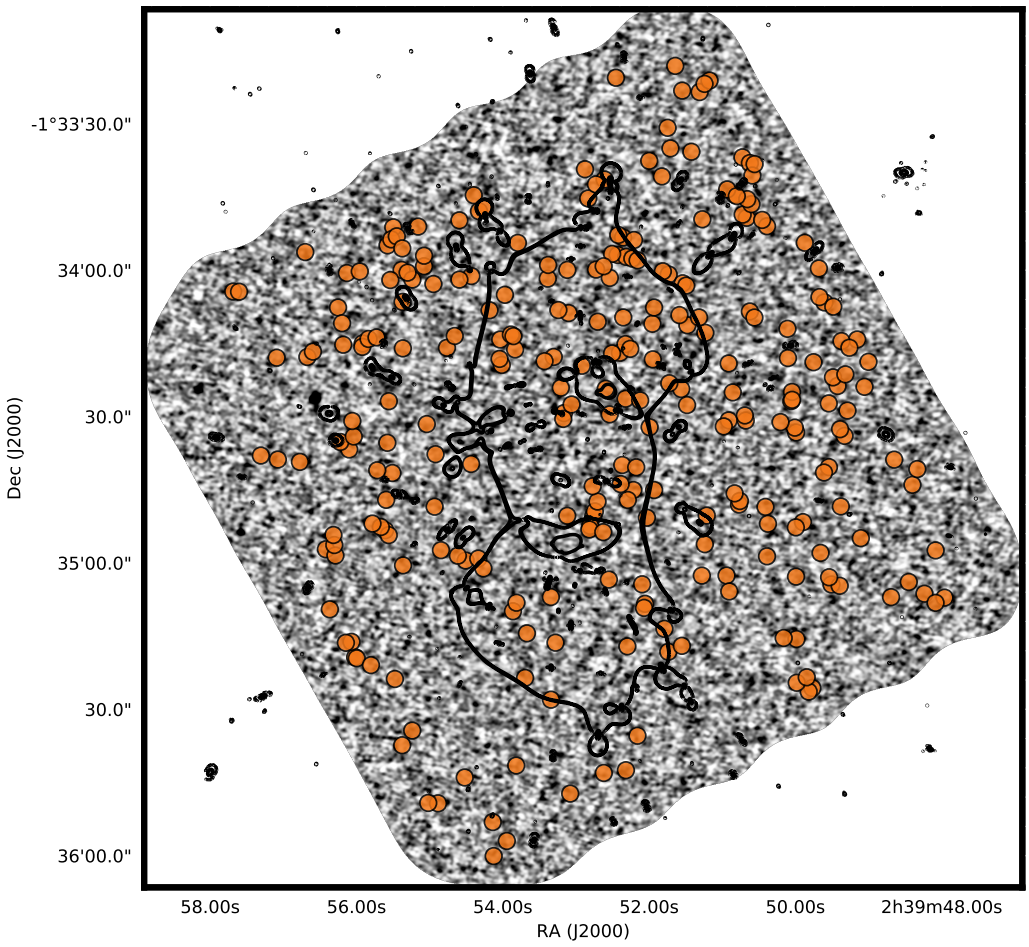

Figure 2.1: ALMA image of A370. Natural CLEANing was used to retrieve it. Orange circles show the positions of our selected LBG candidates. Black thick lines outline the zones of highest magnifications from the magnification map of the cluster. Color scale corresponds to -2σ and $+2\sigma$ from white to black.

2.2 ALMA Stacking Considerations

We used `stacker` (Lindroos et al., 2015) to perform the stacking of our candidates in the ALMA images (see §3.3). This program takes, as input, the lists of targets positions –R.A., Dec– and weights for the stacking process. Weights are drawn from the CASA `clean` pb-correction map –`.flux` extension file (cf. §2.9)–, which corresponds to the sky sensitivity

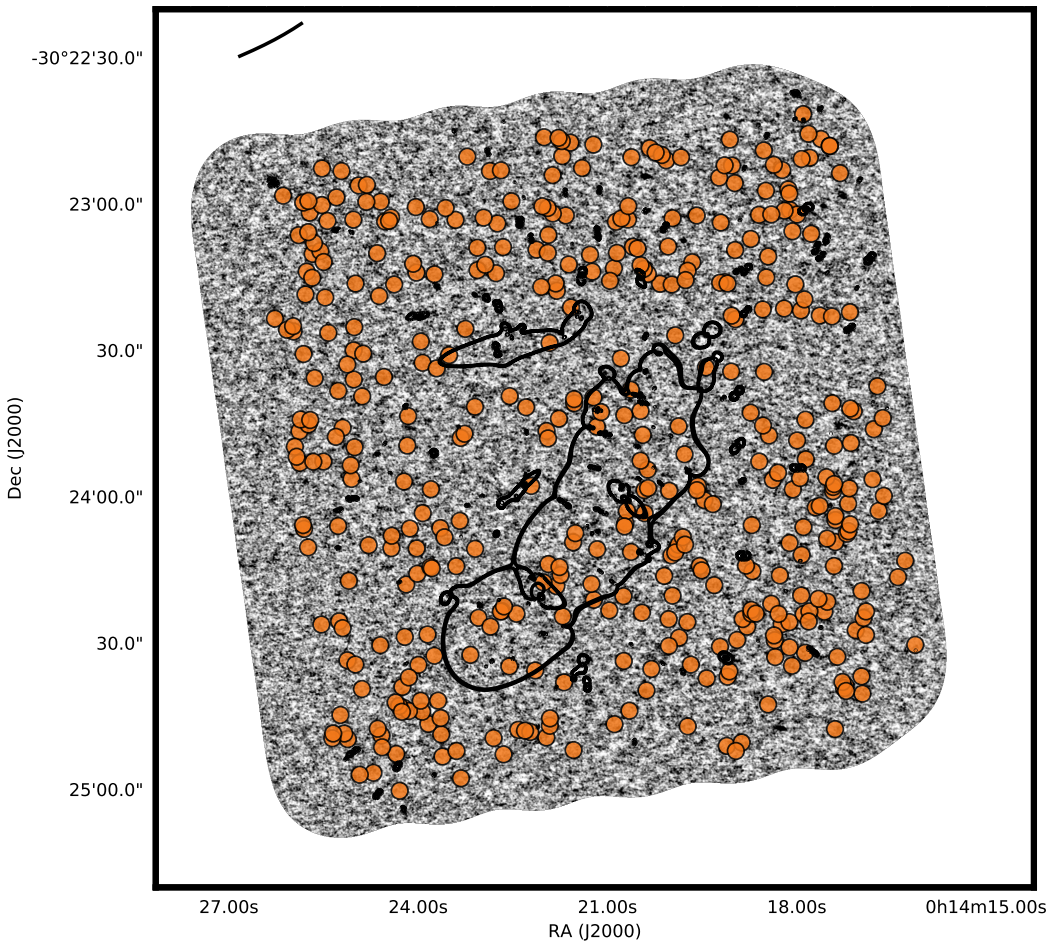

Figure 2.2: ALMA image of A2744. Natural CLEANing was used to retrieve it. Orange circles show the positions of our selected LBG candidates. Black thick lines outline the zones of highest magnifications from the magnification map of the cluster. Color scale corresponds to -2σ and $+2\sigma$ from white to black.

over the field. This weight is used for stacking in the image domain in the form of $1/\sigma^2$. This initial definition for the weight can be modified to any other values depending on the desire of the user (see §3.3). For this work, two weight schemes were used to improve the stacked signal according to the observed properties of the LBG candidates beyond the original weight, which only incorporates the sensitivity of the maps.

One important issue to consider is that the coordinates of the LBG candidates were ob-

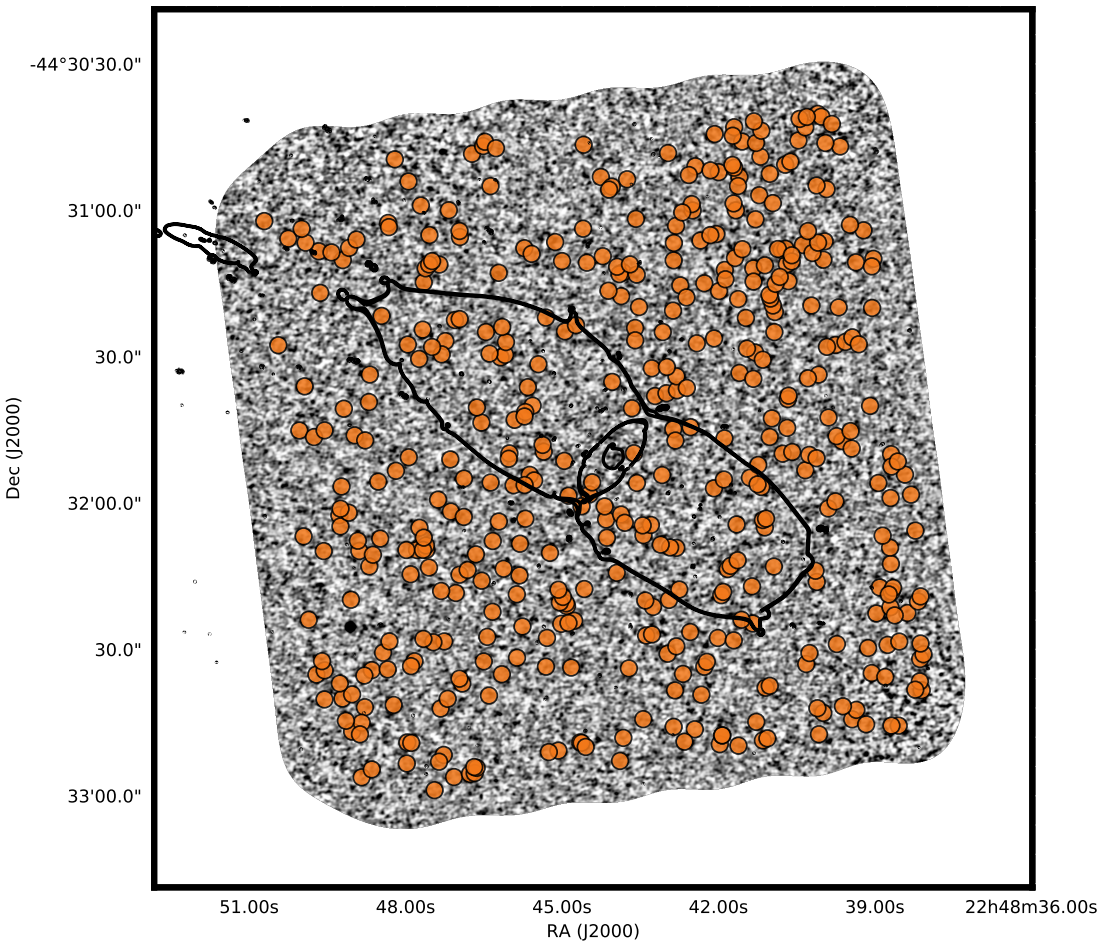

Figure 2.3: ALMA image of AS1063. Natural CLEANing was used to retrieve it. Orange circles show the positions of our selected LBG candidates. Black thick lines outline the zones of highest magnifications from the magnification map of the cluster. Color scale corresponds to -2σ and $+2\sigma$ from white to black.

tained using *HST* data. However, it is possible that potential mm/submm emission in the ALMA maps may arise from a somewhat different position than the optical counterpart, given the large difference in observed wavelengths and emission mechanisms. In particular, the more dust-rich regions that could give rise to submm emission would tend to extinct embedded stars, while nearby stars in less dust-rich regions might contribute more to the near-IR light.

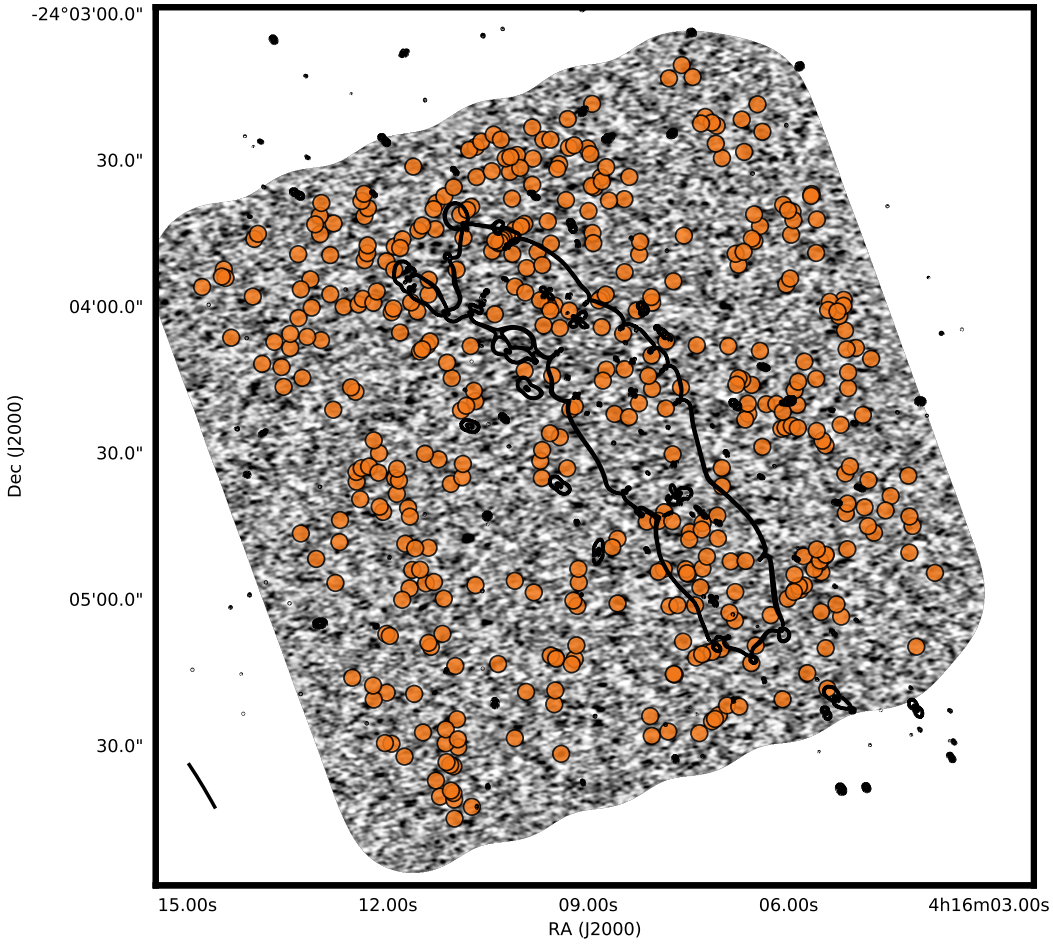

Figure 2.4: ALMA image of MACSJ0416. Natural CLEANing was used to retrieve it. Orange circles show the positions of our selected LBG candidates. Black thick lines outline the zones of highest magnifications from the magnification map of the cluster. Color scale corresponds to -2σ and $+2\sigma$ from white to black.

We argue, however, that such offsets are unlikely to affect our final results (i.e., the stacked flux), since the angular sizes of the LBG candidates are generally similar or smaller than the beam sizes of our ALMA observations (~1″) and spatial offsets between securely detected FIR/mm ALMA sources and optical/NIR counterparts are generally small (e.g., 0.″17±0.″02 González-López, Bauer, Romero-Cañizales, et al., 2017).

For the reasons above and to simplify calculations, no correction was performed regard-

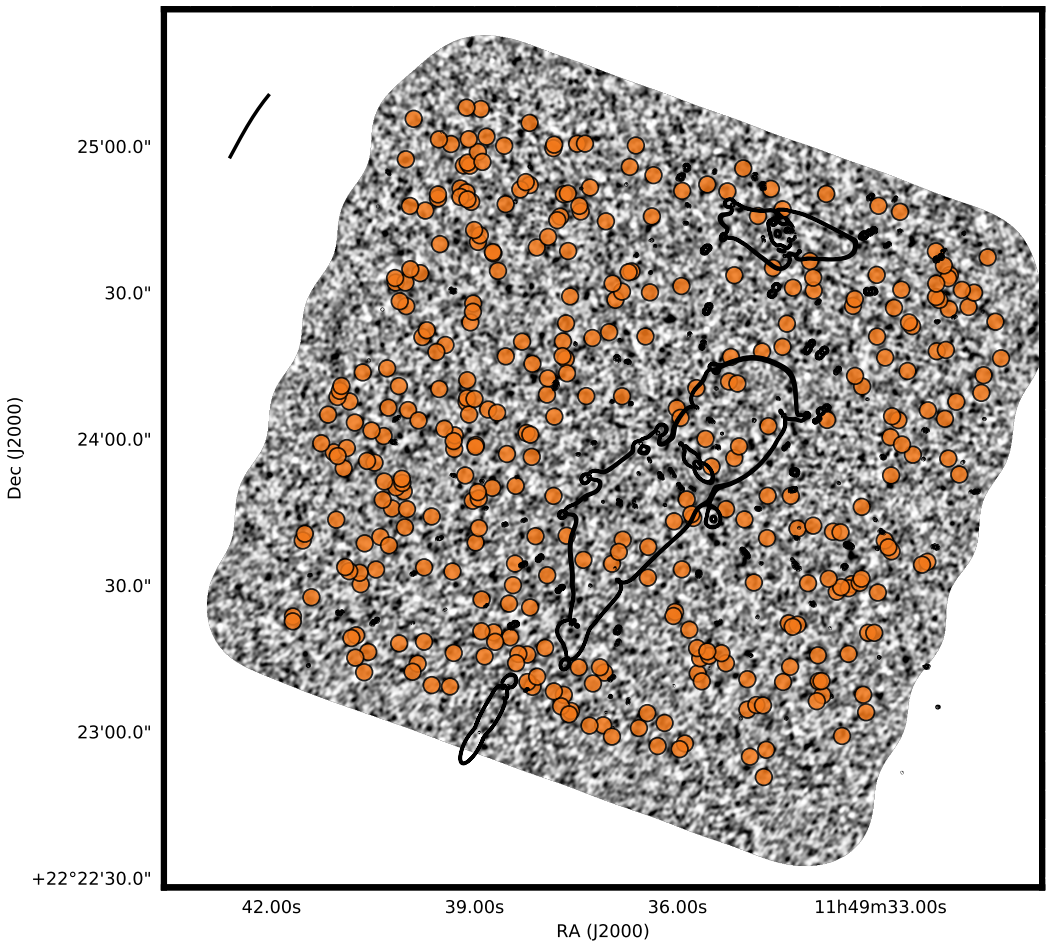

Figure 2.5: ALMA image of MACSJ1149. Natural CLEANing was used to retrieve it. Orange circles show the positions of our selected LBG candidates. Black thick lines outline the zones of highest magnifications from the magnification map of the cluster. Color scale corresponds to -2σ and $+2\sigma$ from white to black.

ing relative positional offsets. That being said, in order to obtain actual stacked and individual fluxes from the ALMA maps in §2.10, we will consider values at larger distances due to the influence of the synthesized beam.

2.3 LBG candidates

Deep *HST* images are available in seven broadband filters as part of the FFs campaign (Lotz et al., 2017): Advanced Camera for Surveys (ACS) filters $F435W$, $F606W$, $F814W$ –with 0.″4 aperture $5-\sigma$ depths of 28.8, 28.8 and 29.1 ABmag, respectively–; Wide Field Camera 3 (WFC3) IR filters $F105W$, $F125W$, $F140W$, $F160W$ –with 0.″4 aperture $5-\sigma$ depths of 28.9, 28.6, 28.6 and 28.7 ABmag, respectively–. Two additional deep images were obtained with WFC3 UVIS filters $F275W$ and $F336W$ –with 0.″4 aperture $5-\sigma$ depths of $\approx$27.5 – 28.0 ABmag, depending on the cluster– as part of a supporting UV campaign (PI: Siana; Alavi et al., 2016).

The success of the LBG drop-out technique (e.g, Steidel, Giavalisco, Dickinson, et al., 1996) arises from the strong flux difference between broadband filters which sample the blueward and redward sides of the Lyman Break, which occurs as a function of redshift at $912\times(1+z)$Å. For the given selection of *HST* filters observed in the FFs, we can detect these strong flux differences and obtain LBG candidates in crude redshift bins of $z\sim2, 3, 5, 6, 7$, and 8. These LBG samples were obtained adopting the strategies of Bouwens, Aravena, et al. (2016) for the $z\sim2-3$ range and Bouwens, Illingworth, Oesch, Trenti, et al. (2015) for the remaining redshift ranges. There is no LBG sample at $z\sim4$ due to the lack of photometric coverage around ~5500Å (e.g., $F555W$).

As examples, for the $z\sim2$ sample, the criteria are

$$\begin{aligned}&(\mathrm{UV}_{275}-\mathrm{U}_{336}>1)\wedge(\mathrm{U}_{336}-\mathrm{B}_{435}<1)\wedge\\&(\mathrm{V}_{606}-\mathrm{Y}_{105}<0.7)\wedge(S/N(\mathrm{UV}_{225})<1.5)\end{aligned}\tag{2.1}$$

Whereas, for $z\sim3$ galaxies,

$$\begin{aligned}&(\mathrm{U}_{336}-\mathrm{B}_{435}>1)\wedge(\mathrm{B}_{435}-\mathrm{V}_{606}<1.2)\wedge\\&(\mathrm{i}_{775}-\mathrm{Y}_{105}<0.7)\wedge(\chi^2_{\mathrm{UV}_{225},\mathrm{UV}_{275}}<2)\end{aligned}\tag{2.2}$$

where $\wedge$, $\vee$ and S/N represent the logical AND, OR and signal-to-noise respectively. The quantity $\chi^2_{\mathrm{UV}_{225},\mathrm{UV}_{275}}$ is defined as $\sum_i \mathrm{SGN}(f_i)(f_i/\sigma_i)^2$ with f_i being the flux in bands UV_{225} or UV_{275} in a small-scalable aperture, σ_i the uncertainty in this flux, and SGN(f_i) a function which is equal to 1 if $f_i > 0$ and -1 if $f_i < 0$.

An initial list of 2923 LBG candidates was produced based on the above equations, using the *HST* observations from the FFs. We expect the spatial distribution of our LBG candidates to be roughly uniform over the source plane of the selected FFs. This will translate to fewer sources in highly magnified regions –near critical lines on the magnification maps– in the image plane, as we are sampling smaller intrinsic space densities. However, critically, the magnification means we probe further down the luminosity function in these regions. Thus, we expect the targets to span an interesting range in properties (e.g., magnification, SFR, $M_\star$, redshift, etc.). This helps to build a statistically diverse set of LBG properties to study. Distributions of their attributes are presented in §2.4 and later sections.

2.4 Photometric redshifts

As a check on our LGB candidate selection, we used the photometry of each LBG candidate to obtain a photometric redshift estimate. For this purpose, we used code EAZY (Easy and Accurate Photometric Redshifts from Yale; Brammer et al., 2008) with a binsize of $\Delta z_{ph} = 0.01$. To assess the quality and reliability of the photometric redshift values obtained with EAZY, we performed the same process but with BPZ (Bayesian Photometric Redshifts; Benítez, 2000).

The results from EAZY and BPZ are shown in Fig. 2.6, indicating that the BPZ results tend to be lower than those from EAZY. We also separated the sample according to the drop-out band of the targets looking for any discrepancy in the derived values. For the EAZY values in the upper histogram, we can see that the sub-samples do not overlap strongly, as it does happen with BPZ calculations (right panel in Fig. 2.6), which also shows a large spread in redshift values. For instance, for drop-out bands at $z\sim7$ and $z\sim8$, they spread more than 4

redshift units. The redshift bands given by the drop-out technique are a good prior for the photometric values –since there is a good match between their values–, so we do not expect to have long deviations from them. Since `EAZY` does not show such results (large spread and strong overlap), we adopt their values as our primary input.

For statistical reasons and since studying our complete sample in one category will not give any conclusive result as opposed to separate it into smaller sub-groups, it is better to split our sample of LBG candidates. In that way, it is possible to obtain better constrained values for the aggregated properties of our objects.

Given the photometric redshift distribution shown in the upper histogram of Fig. 2.6, we can separate our candidates into two main sub-samples: high, $z_{ph} \geq 4.0$, and low, $z_{ph} < 4.0$, redshift. And, for the high-redshift sample, an extra division can be made for candidates with $z_{ph} > 7$. This division of three bins was used for the rest of the work.

Additionally, we were able to obtain a derived quantity from the photometric redshift values; it is possible to obtain a luminosity distance using part of the script written by James Schombert to resemble Ned Wright's Cosmological Calculator[3] (Wright, 2006).

The distribution of these distances is, as expected, very similar to that of z_{ph} as can be observed in Fig. 2.7.

2.5 Magnification factors

Magnification factors were obtained following the procedure from Coe et al. (2015) and the Python script offered by the FF team[4]. This code obtains the values from the weak lensing shear (γ) and mass surface density (κ) maps that are part of the lens models products for a given redshift value. We used the latest available cluster models from the CATS –Clusters As TelescopeS– team (`v4;` Jauzac et al., 2014; Richard et al., 2014). In this case, the code uses, also, the photometric redshift of the candidates and the confirmed redshift of the lensing

[3] `http://www.astro.ucla.edu/~wright/CosmoCalc.html`

[4] `https://archive.stsci.edu/prepds/frontier/lensmodels/#magcalc`

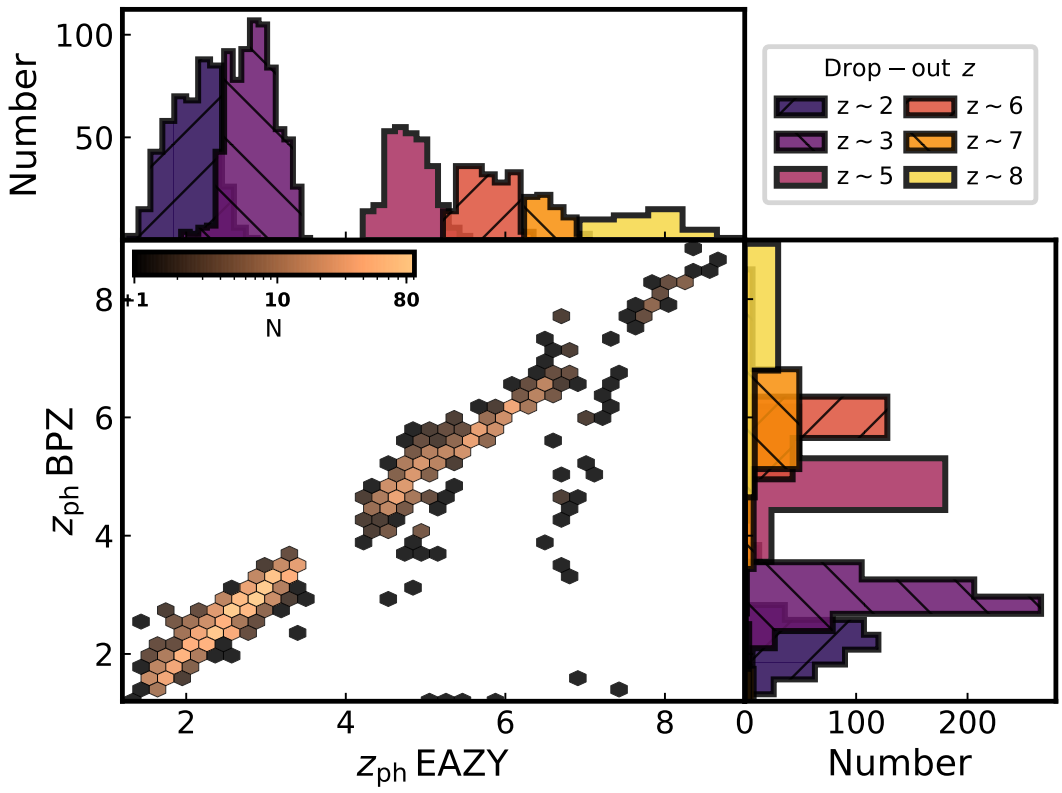

Figure 2.6: Comparison of photometric redshift values for our sample obtained with `EAZY` and `BPZ` software tools. Upper and right panels show the distribution of the values separately and colored by drop-out band. In the lower left panel, the color indicate the number of elements in each bin; the lighter the color, the higher the number of elements. The legend only applies to the histograms.

cluster (Table 2.1).

With these values, the magnification factor (μ) is obtained from the expression:

$$\frac{1}{\mu} = |(1-\kappa)^2 - \gamma^2| \tag{2.3}$$

As some targets can lie in positions very close to the critical curves of the model lenses, extreme magnification values were found ($\mu > 1000$) during the calculations. To avoid possible spurious results when using these targets in calculations –specially, when stacking

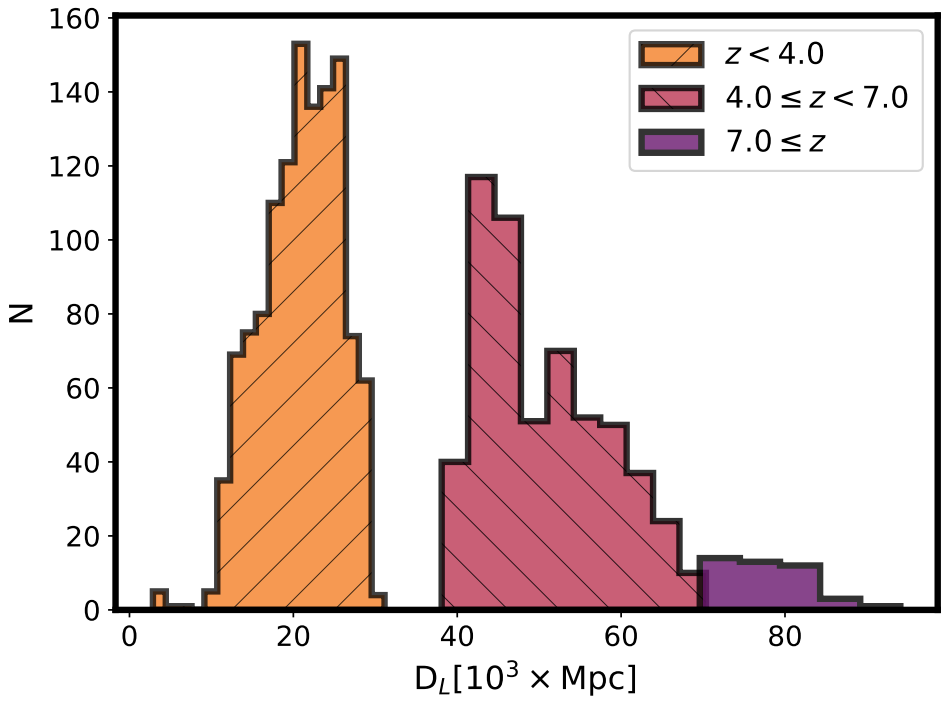

Figure 2.7: Distribution of luminosity distances for the LBG candidates per photometric redshift bin. Luminosity distances and their calculation are strongly related to the value of the photometric redshift and the distribution shown here is almost the same as the one that motivated the z binning.

with magnification factors as weights (see §3.3).–, their magnification factors were capped to the more conservative value $\mu = 10$. After this correction, magnification values can range from $\mu = 1$ to $\mu = 10$ with a manifest over-population at $\mu = 10$ for all three redshift bins, as displayed in Fig. 2.8.

2.6 UV-continuum slope

For each candidate, HST photometry was used to obtain UV-continuum slope (β) values, which correspond to the steepness of the ultraviolet part of the spectrum.

Several methods have been developed to calculate this value from different photometry

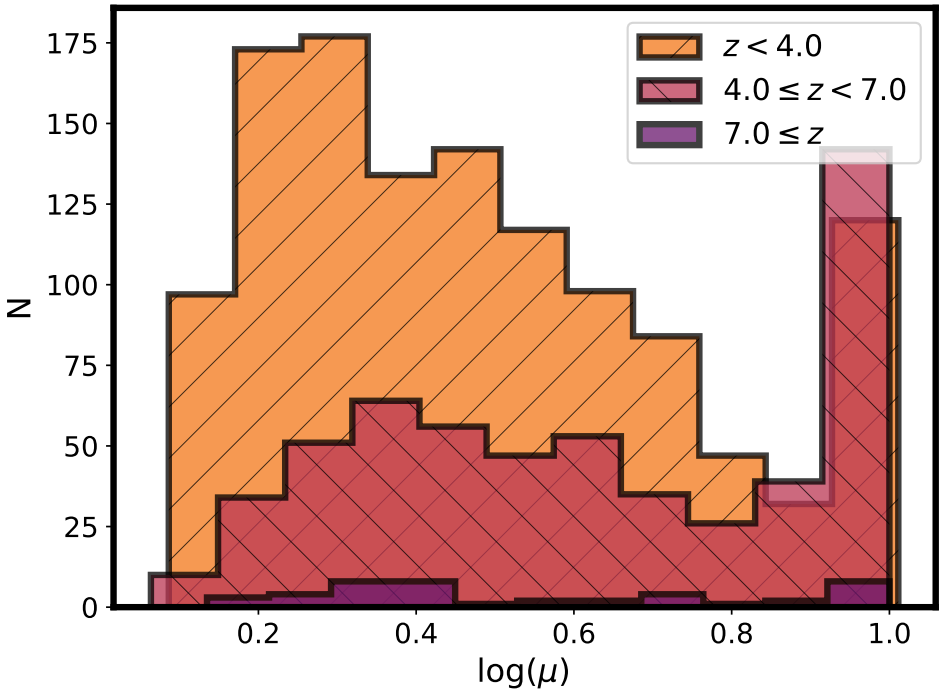

Figure 2.8: Distribution of magnification factors (μ) in our sample according to the three bins in photometric redshift.

bands (for a review, see Rogers et al. 2013, §2 and McLure et al. 2018, §2.7). In this case, we took advantage of the number of bands we have access to –nine of them– with a naive approach using the bands –and the flux in them– that lie in the expected UV-continuum region of each spectrum assuming the previously derived redshift. Bands with upper limit values were discarded for this calculation, as they were few compared to the full sample. A simple power law ($F_\lambda \propto \lambda^\beta$) was fit to the points with a basic maximum likelihood estimator.

In particular, for this work, we used the power law shown in Castellano et al. (2012). It has the following form:

$$m_i = -2.5 \times (\beta + 2.0) \times \log(\lambda_i) + c \tag{2.4}$$

where m_i is the AB magnitude (Oke and Gunn, 1983) in the i-th band at an effective wave-

length λ_i and c is the intercept. The distribution of β-slopes vs the UV magnitude is presented in the left panel of Fig. 2.9. Since the broad division in photometric redshift does not show any particular trend of β with the redshift of the targets, a different approach has to be given to understand any possible correlation. This is shown in Fig. 2.10 where our targets have been binned according to photometric redshift. There it can be seen that the UV-slopes of our LBG candidates show an increase up to redshift $z{\sim}4-5$ and then a drop is present until $z{\sim}7$. This behavior is compatible with the results of previous works such as Bouwens, Illingworth, Oesch, Franx, et al. (2012), Bouwens, Illingworth, Oesch, Labbé, van Dokkum, et al. (2014), and Finkelstein et al. (2012) in which targets with $z_{\rm ph}{\gtrsim}4$ have been studied and an evolution in redshift can be inferred. Given that the number of LBG candidates with $z_{\rm ph}{\gtrsim}8$ we have access to is considerably small, N=13, their overall behavior should be taken with caution. Due to this, we cannot either confirm or discard the claimed trend.

For the purposes of this work, we defined the UV magnitude, flux or luminosity ($m_{1600\text{Å}}$, $F_{1600\text{Å}}$, $L_{1600\text{Å}}$) to be that measured at 1600 Å (following, among others, Madau and Dickinson 2014, which give a range between 1400 Å and 1700 Å for a sensible UV wavelength). In our case, we use the photometric band which lies closest to that rest-frame wavelength.

2.7 Stellar Mass

Stellar masses were estimated using the C++ version[5] of FAST (Fitting and Assessment of Synthetic Templates; Kriek et al., 2009) which fits stellar population synthesis templates to photometric data. The input values were the magnitudes from our drop-outs catalog as well as the photometric redshift values from EAZY. For this work, we assumed a Chabrier stellar initial mass function (IMF; Chabrier, 2003), which has been derived from the Bruzual and Charlot (2003) SEDs. We also assumed an exponentially declining star formation history [SFH $\propto \exp(-t/\tau)$] with $\log_{10}(\tau/\text{yr})$=11 and a metallicity of $0.0040Z/Z_{\odot}$. Also, a Calzetti et al. (2000) dust attenuation law with $0.0 \leq A_V \leq 1.0$ was used. With these parameters, the

[5] FAST++. https://github.com/cschreib/fastpp

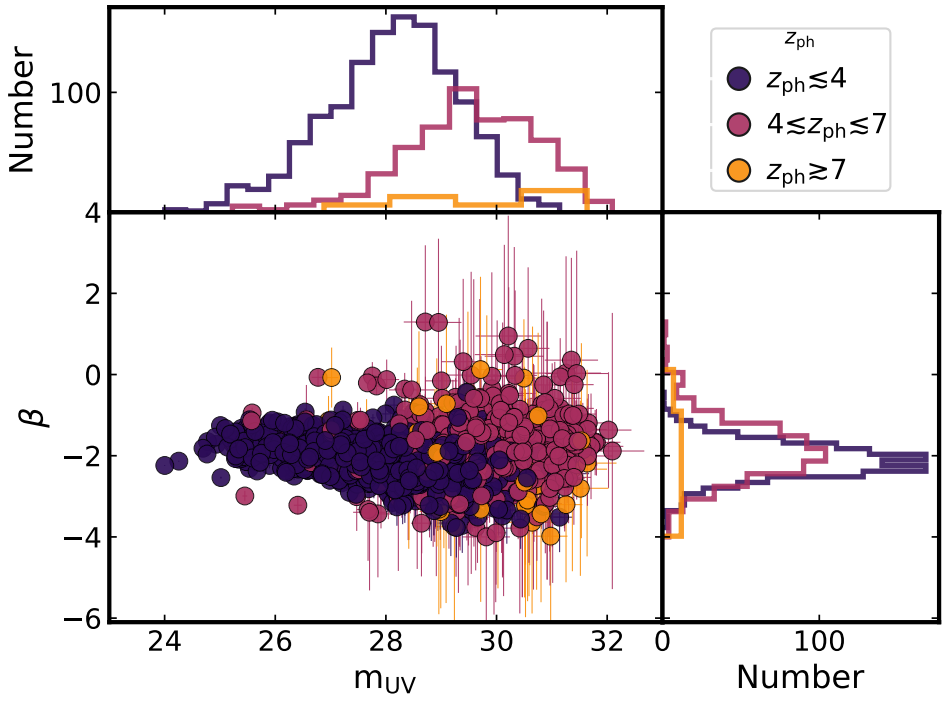

Figure 2.9: UV-slopes (β) from our selected sources as a function of UV magnitudes. Colors represent photometric redshift subsample of each candidate, as shown in the legend and in §2.4. In top and right panels, histograms of these values are shown separated by photometric redshift range too.

code outputs, apart from other relevant properties, a stellar mass estimate for each target.

These values have to be corrected by the magnification factors to avoid overestimations and further errors. In order to obtain the magnification-corrected stellar masses –or other property, as discussed further in the text–, the values given by `FAST++` –or any other similar software– have to be divided by the magnification factors. Using the logarithm of the stellar mass, it would look as the following:

$$\log_{10}(M_{\star,\mu-\text{corrected}}/M_{\odot}) = \log_{10}(M_{\star,\texttt{FAST}}/M_{\odot}) - \log_{10}(\mu) \tag{2.5}$$

For the rest of this work, we will refer to the magnification-corrected stellar mass as

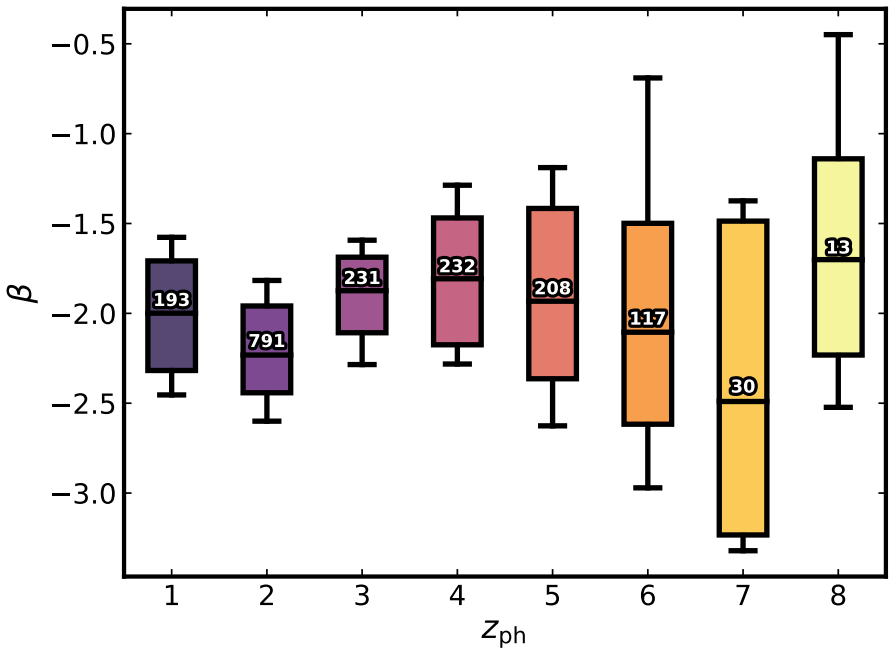

Figure 2.10: Distribution of β values according to photometric redshift. Heights of boxes represent the 25% and 75% quartiles of the data. Horizontal lines inside the box indicate median value for each redshift bin. Vertical lines span covering the central $2-\sigma$ of the data. Numbers above each box state the size of each bin. Data points outside of these limits are not shown.

stellar mass. The distribution of values for our three photometric redshift bins is plotted in Fig. 2.11.

2.8 (Specific) Star Formation Rates

One of the by-products of FAST++ is a Star Formation Rate (SFR) estimation. As with stellar mass, SFR values have to be corrected by lensing effects by dividing the derived value by the magnification value (μ).

$$\log_{10}\left(\mathrm{SFR}_{\mu-\mathrm{corrected}}/\mathrm{M}_{\odot}\mathrm{yr}^{-1}\right) = \log_{10}\left(\mathrm{SFR}_{\mathtt{FAST}}/\mathrm{M}_{\odot}\mathrm{yr}^{-1}\right) - \log_{10}\left(\mu\right) \tag{2.6}$$

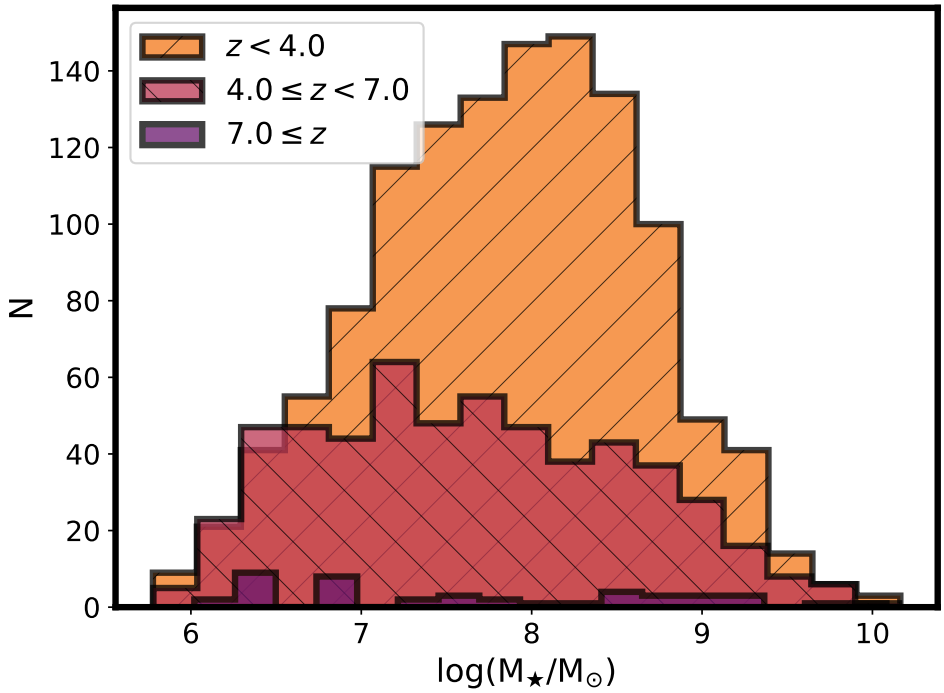

Figure 2.11: Distribution of stellar mass in our sample. The sample has been divided according to the photometric redshift bins defined in §2.4.

For the rest of this work, we will refer to the magnification-corrected star formation rate as star formation rate. Their distribution is shown in Fig. 2.12

From the star formation rates and the stellar mass from §2.7, the specific star formation rates (sSFR) can be, then, obtained as:

$$\log_{10}\left(\mathrm{sSFR/yr^{-1}}\right) = \log_{10}\left(\frac{\mathrm{SFR/M_{\odot}yr^{-1}}}{\mathrm{M_{\star}/M_{\odot}}}\right) \tag{2.7}$$

which is independent of the magnification factor of each LBG candidate. The distribution of values for our three photometric redshift bins can be seen in Fig. 2.13.

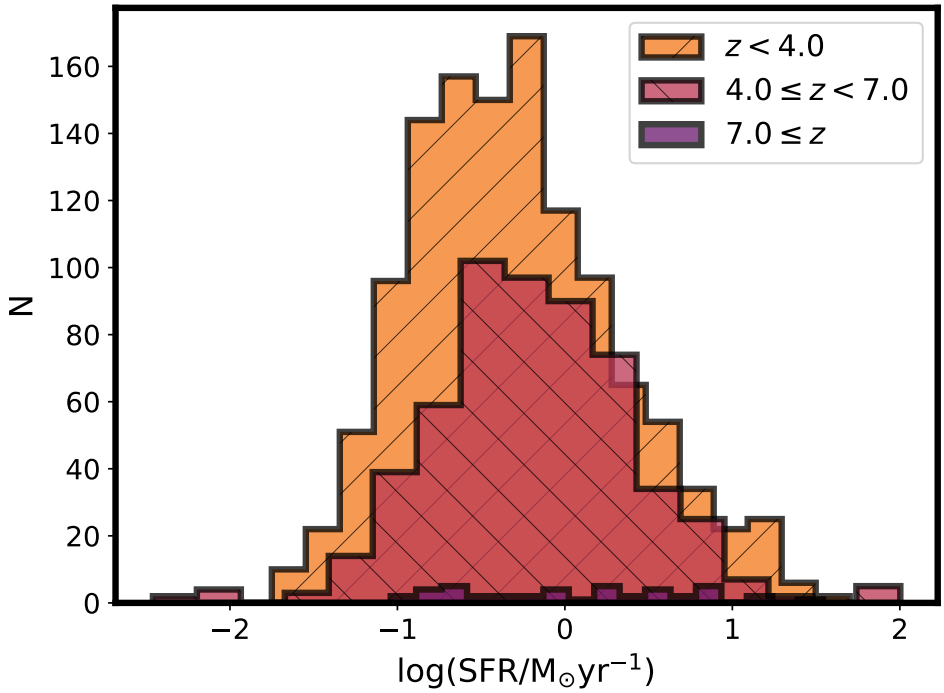

Figure 2.12: Distribution of star formation rates in our sample. The sample has been divided according to the photometric redshift bins defined in §2.4.

2.9 ALMA primary-beam corrections

To obtain images from interferometric observations, each element of the observation has to be corrected by the sensitivity of every antenna in the array. The concept can be roughly compared to the use of the point spread function (PSF) in optical observations.

With interferometric data, the process from obtaining the data from the observed source to the final image includes some deconvolution, rescaling, and calibrations. For some parts of this procedure, the primary beam has to be taken into account. After obtaining a *CLEANed* image –an image to which the *CLEAN* deconvolution algorithm has been applied–, the data can be corrected by the sensitivity of the observations. This sensitivity is quantified by the primary beam correction (see, for instance, Thompson et al., 2017; Wilson et al., 2013). Thus, any measured flux has to be corrected –in our case, divided– by the primary beam correction

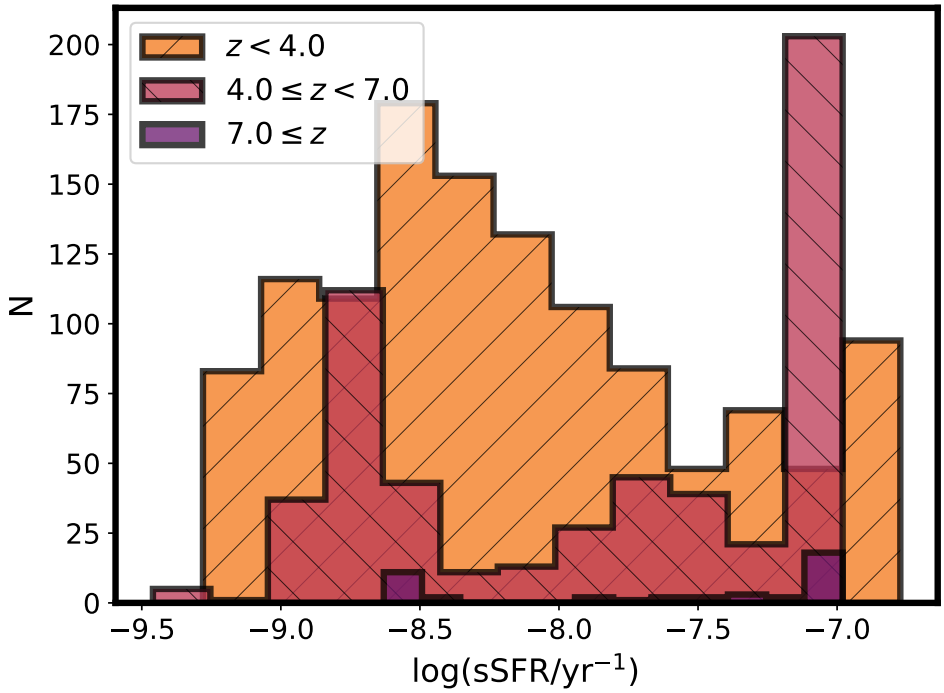

Figure 2.13: Distribution of intrinsic star formation rates in our sample. The sample has been divided according to the photometric redshift bins defined in §2.4.

factor.

As part of the ALMA products of the observations, a map of sensitivities is delivered which includes the primary-beam correction factors. After the final deconvolution –in our case, after CLEANing– a file with the extension `.flux` is produced. It has a map –in image space– of the values for each position in the field of view. Their values might range from 0.0 to 1.0, in which 1.0 shows that the position has the highest sensitivity of the map. Thus, the higher primary beam correction, the better quality the observation might be.

2.10 ALMA peak fluxes

For simplicity, we adopt peak flux measurements, $F^{\rm indiv}_{\rm ALMA,peak}$, since integrated fluxes require an assumption about the flux distribution shape, and since magnification effects are

involved, this becomes a highly arduous task. To assess these within the ALMA maps, we searched for the pixel with the maximum value within a 0.″5×0.″5 box (i.e., comparable to one synthesized beam) centered at the position of each LBG candidate. This procedure attempts to account for the influence of the synthesized beam, as well as possible extended emission, in the ALMA maps. The result is an observed peak flux for each candidate, $F^{\rm indiv,obs}_{\rm ALMA,peak}$. We correct this flux for the primary beam attenuation as:

$$F^{\rm indiv,obs}_{\rm ALMA,peak,pbcor} = \frac{F^{\rm indiv,obs}_{\rm ALMA,peak}}{pbcor^{\rm indiv}_{\rm ALMA}}. \tag{2.8}$$

Likewise we relate the *rms* error at the position of an individual source to the field rms, $rms_{\rm cluster}$, listed in §2 for each studied cluster, as

$$rms^{\rm indiv}_{\rm ALMA,pbcor} = \frac{rms^{\rm cluster}_{\rm ALMA}}{pbcor^{\rm indiv}_{\rm ALMA}}. \tag{2.9}$$

The bulk of our candidates have ALMA fluxes comparable to the *rms* values of their respective maps, but a few are associated with brighter peak fluxes. For this reason, we want to define clearly which targets are detected and for which we only have upper limits. As a first conservative approach, we search for LBG candidates with signal-to-noise ratios (SNRs) above 5.0 in each image, which roughly corresponds to the blind detection limit for the ALMA-FF maps (González-López, Bauer, Romero-Cañizales, et al., 2017). We define here the SNR as:

$$\mathrm{SNR} = \frac{F^{\rm indiv,obs}_{\rm ALMA,peak}}{rms^{\rm cluster}_{\rm ALMA}} = \frac{F^{\rm indiv,obs}_{\rm ALMA,peak,pbcor}}{rms^{\rm indiv}_{\rm ALMA,pbcor}}. \tag{2.10}$$

None of our targets fulfills this first condition, with a maximum value of SNR= 4.21 for a candidate in AS1063.

The blind detection limit, however, is with respect to a search of all positions on the map. But since we know the positions of the LBG candidates and they comprise only a small fraction of the overall map area, a more realistic estimate of the detection significance is to

evaluate the False Detection Rate (FDR or $p_{\rm FDR}$) for each ALMA map. To this end, following the procedures outlined in Muñoz Arancibia et al. (2017), we generated 1000 simulated maps for each ALMA field with a normal distribution in units of signal-to-noise. From these, we extracted the same number of simulated peak fluxes per cluster as we did for the LBG candidates, again choosing the highest peak flux within a square of 0.″5 on a side. We define $p_{\rm FDR}$(SNR) to be the fraction of simulated maps of a specific cluster where at least one sampled pixel was found above a given SNR. Fig. 2.14 shows the FDRs for our five ALMA maps.

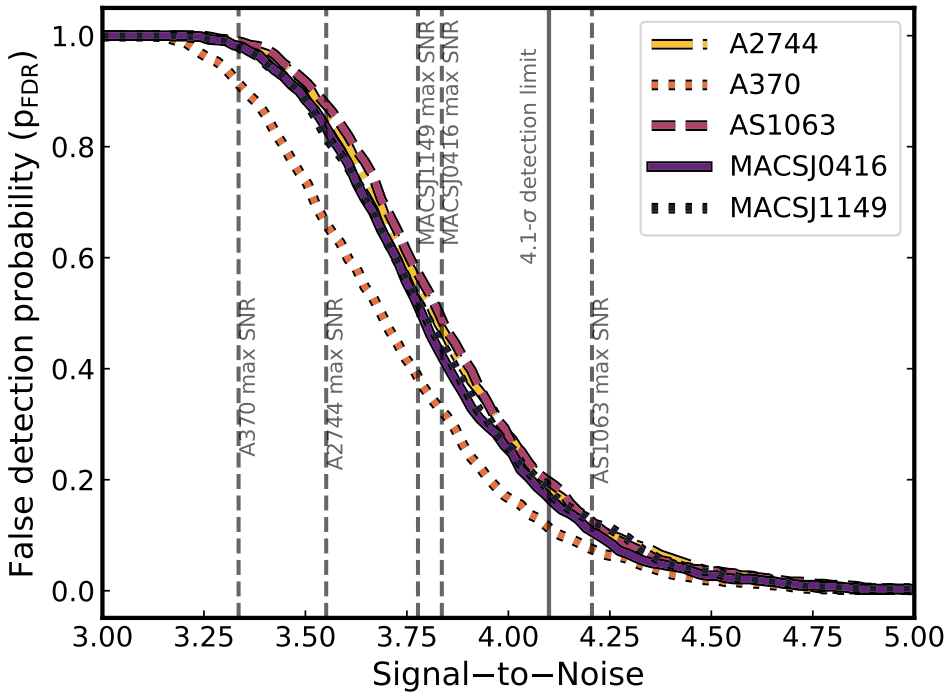

Figure 2.14: False detection rate, $p_{\rm FDR}$, for the five ALMA maps. Vertical dashed lines denote the highest detected SNR among the LBG candidates in each ALMA map. Vertical solid line denotes our adopted SNR cutoff of 4.1, which equates to a FDR around 15% among the cluster fields.

Based on the FDRs, we find that sources with SNR$\gtrsim$4.1 have a relatively low ($\lesssim$15%) chance of being false. For simplicity and uniformity, we consider all LBG candidates above this limit to be detected, while the LBG candidates below this are treated as upper limits.

We calculate individual detected peak fluxes following Eq. 2.8, while n-σ upper limits are calculated as

$$F^{\mathrm{indiv,obs\,n-}\sigma\,\mathrm{lim}}_{\mathrm{ALMA,peak,pbcor}} = \frac{(F^{\mathrm{indiv,obs}}_{\mathrm{ALMA,peak}} > 0) + \mathrm{n} \times rms^{\mathrm{cluster}}_{\mathrm{ALMA}}}{pbcor^{\mathrm{indiv}}_{\mathrm{ALMA}}}, \tag{2.11}$$

where the >0 expression indicates the fact that the observed peak flux from the ALMA map is only used if it is greater than zero. This implies that no single candidate will have a 1-σ, or higher, upper limit lower than the noise level of the map to which it belongs. The incorporation of local map noise, in addition to the average *rms*, yields a more conservative upper limit.

2.11 UV Luminosities

As mentioned in §2.6, we defined the UV luminosity as the 1600Å luminosity which is first calculated as a flux and then transformed into luminosity using the luminosity distances described in §2.4. Thus, the needed flux is calculated as $F_\lambda = \nu_\lambda \times f_\lambda$ for $\lambda = 1600\text{Å} \times (1+z)$. And then, the expression $L_\lambda = 4\pi D_L^2 F_\lambda$ is used to obtain the desired luminosity.

After using this definition, it is needed to post-process them to account for corrections related to the distances and ages involved in the environments of the candidates. In this manner, intrinsic luminosities will be derived; this, in the form of rest-frame properties.

The first correction is associated with the redshift values of the targets. The corresponding frequencies have to be derived to be rest-frame values. The same occurs with the overall flux –or luminosities– which will become smaller in intensity by a factor $(1 + z)$, coming from the use of luminosity distance as length scale. This type of correction is called K-correction (e.g., see §5.6.1 from Schneider, 2006).

A second adjustment involves the main reason to study LBGs –and other objects– in the Frontier Fields: magnification from the galaxy clusters will allow computing the intrinsic luminosities for each candidate. This will be attained dividing the chosen property by the already calculated magnification factors, as with the previously described properties.

2.12 IR Luminosities

With only one point of constraint from ALMA (our peak fluxes), the procedure to estimate the IR luminosity is more model-dependent than for the UV bands and it requires more steps than the UV luminosities. For this, we fit a modified blackbody (graybody) spectrum (e.g., Casey 2012; Schaerer, de Barros, and Sklias 2013) to the ALMA photometric data. We adopt typical fixed values of 35 K for the dust temperature (e.g., Kovács et al., 2006; Coppin et al., 2008), 2.0 for the mid-IR power-law slope, and 1.6 for the emissitivity (e.g., best-fit values for the GOALS survey; Casey, 2012). For simplicity, we adopt the same shape for every LBG candidate. The best-fitted rest-frame SED is integrated between 8μm and 1000μm to yield the rest-frame IR luminosity. In practical terms, we define a scale factor $f_{\rm IR}^{\rm ALMA}$ to convert observed ALMA peak flux to the magnification-corrected, rest-frame IR luminosity as

$$f_{\rm IR}^{\rm ALMA} = \left(\frac{F_{\rm ALMA,peak}^{\rm indiv,obs}}{F_{\rm 1.14mm/(1+z)}^{{\rm SED}\mu}} \right). \tag{2.12}$$

In this way, any derived infrared luminosity will be multiplied by $f_{\rm IR}^{\rm ALMA}$ to obtain the expected peak value for each LBG candidate.

We chose this method over the use of `FAST++` or `magphys` SED fitting to obtain IR luminosity estimates due to the fewer number of free parameters (e.g., dust temperature, attenuation, SED templates), which made for a more straightforward implementation and interpretation. In general, the luminosities derived from the best-fit modified blackbody to the ALMA data are a factor of 10–100 higher than rest-frame UV/optical based estimates from `FAST++` or `magphys`. In general, for the few detections our estimates are presumably more robust, while for the upper limits they should be considered as very conservative.

In addition to the aforementioned corrections for redshift and magnification, the IR luminosities (or fluxes) have additional dependence on the redshift of the candidate due to the impact of the Cosmic Microwave Background (CMB) temperature on the dust properties. Following the procedure and discussion of da Cunha et al. (2013), the derived IR luminosities

are divided by the factor

$$g_\nu^{\rm CMB} = \left[1 - \frac{B_\nu(T_{\rm CMB}(z))}{B_\nu(T_{\rm dust}(z))}\right], \tag{2.13}$$

where $B_\nu(T_{\rm dust})$ and $B_\nu(T{\rm CMB})$ correspond to the source and CMB blackbody contributions, respectively.

2.13 IRX relations

Sensitive millimeter facilities such as *Herschel* and ALMA have only become available in the last decade. Prior to these, it was generally difficult to measure IR luminosities for distant galaxies, and indirect methods were employed to understand and predict the IR emission. Principal among these is the so-called IR excess ratio (IRX), which is loosely defined as the quotient between the IR and UV luminosities (or fluxes) of a source (in this case, a galaxy). One of the most utilized definitions was developed by M99, which relates the UV and IR fluxes as:

$$\mathrm{IRX} = \frac{F_{\rm IR}}{F_{1600\text{Å}}} \tag{2.14}$$

where $F_{\rm IR}$ is the rest-frame 8–1000 μm IR flux and $F_{1600\text{Å}}$ is the rest-frame 1600 Å UV flux. This can be trivially extended for rest-frame luminosities instead of fluxes, leading to:

$$\mathrm{IRX} = \frac{L_{\rm IR}}{L_{1600\text{Å}}} \tag{2.15}$$

Among local galaxies, which were more easily observed and constrained with early facilities, a few correlations with IRX have been found. One such relation was derived by M99 (hereafter the M99 IRX-β relation), which empirically relates IRX to the UV continuum slope β as

$$\mathrm{IRX_{M99}} = 1.75 \times \left(10^{0.4\times(1.99\times(\beta+2.23))} - 1\right). \tag{2.16}$$

assuming the Calzetti et al. (2000) "absorption law". An alternative relation adopting a linear fit to the Small Magellanic Cloud (SMC) extinction data from Prevot et al. (1984) performed by Smit et al. (2016) yields the SMC IRX-β relationship:

$$\mathrm{IRX_{SMC}} = 10^{0.4\times(1.1\times(\beta+2.23))} - 1. \tag{2.17}$$

Other recent calibration that corrects aperture effects from M99 was developed, with a similar sample, by Takeuchi et al. (2012) and takes the form:

$$\mathrm{IRX_{Takeuchi}} = 1.66 \times \left(10^{0.4\times(1.58\times(\beta+1.94))} - 1\right). \tag{2.18}$$

Finally, an extension to the M99 IRX-β relation was obtained by Casey, Scoville, et al. (2014), who fit a large number of low redshift galaxies, incorporating a large range of SFR values as well as a correction for aperture effects, finding:

$$\mathrm{IRX_{Casey}} = 1.68 \times \left(10^{0.4\times(2.04\times(\beta+1.64))} - 1\right). \tag{2.19}$$

As already noted, these relations were developed using local galaxy data, but have been tested on a variety of distant (mostly massive) galaxy samples.

Similar to the IRX-β relations above, there have been a large number of studies arguing that the total stellar mass of a galaxy is strongly related to the degree of dust extinction, and hence IRX. We highlight below four recent published correlations between IRX and stellar mass by Heinis et al. (2014, hereafter H14), Fudamoto et al. (2017, hereafter F17), McLure et al. (2018, hereafter M18), and B16.

H14 used *Herschel* constraints of UV-selected galaxies at z~1.5, z~3 and z~4 with stellar masses in the range $10 < \log_{10}(M_\star/M_\odot) < 11$, to develop the following relation:

$$\log_{10}(IRX_{H14}) = 0.72 \times [\log_{10}(M_\star/M_\odot) - 10.35] + 1.32 \quad (2.20)$$

F17 used ALMA observations of 67 photometric-redshift selected galaxies with redshifts between z~3–6 and stellar masses of $\log_{10}(M_\star/M_\odot)$~10.7 to arrive at the relation:

$$\log_{10}(IRX_{F17}) = 0.72 \times [\log_{10}(M_\star/M_\odot) - 10.35] + 1.08. \quad (2.21)$$

Similarly, M18 used ALMA observations of 161 photometrically selected galaxies with redshifts between $2 < z < 3$ and stellar masses in the range $9.25 < \log_{10}(M_\star/M_\odot) < 10.75$ to obtain:

$$\log_{10}(IRX_{M18}) = 0.85 \times [\log_{10}(M_\star/M_\odot) - 10.00] + 0.99. \quad (2.22)$$

B16 employed deep ALMA imaging of 330 LBG candidates in the HUDF, with stellar masses below $10^{9.75}M_\odot$ and redshifts between z=2–10, to obtain:

$$\log_{10}(IRX_{B16}) = \log_{10}[M_\star/M_\odot] - 9.67. \quad (2.23)$$

Finally, B16 also derived a "consensus" IRX-$M_\star$ relation from a variety of previous studies in the redshift range $z \sim 0$ to $z \sim 3$ (e.g, Pannella et al., 2009; Reddy, Erb, et al., 2010), which takes the form:

$$\log_{10}(IRX_{Consensus}) = \log_{10}[M_\star/M_\odot] - 9.17. \quad (2.24)$$

The various IRX-$M_\star$ relations have relatively similar slopes and exhibit a typical dispersion of up to ~1 dex, excluding the strong deviation of H14 above $10^{10}M_\odot$. As such, they provide a potentially useful means of predicting dust attenuation as a function of stellar mass.

3

Methods

3.1 ALMA image retrieval

Observations from ALMA are delivered as visibilities –from the uv-plane– and after imaging them, an image-plane file is obtained. To compare results, two weighting modes were applied to the datasets in CASA when imaging, or *CLEANing*: Natural and Taper.

Natural weighting assigns equal weights to every visibility in the deconvolution process. These weights correspond to $1/\sigma^2$, where σ is the noise variance of the data –visibility–. It maximizes sensitivity for point sources.

The other *CLEANing* mode, uv tapering, creates an adjustable gaussian-like window function, $W(u, v) = \exp(-(u^2 + v^2)/t^2)$, with t the taper parameter. As it gives more weight to shorter baselines, it has more sensitivity to extended sources. For this work, a taper parameter of t=1.″5 was used. This value says that for a general point (u, v), data will be weighted with a Gaussian of width 1.″5.

Using both methods, we can look for eventually extended detections which cannot be observed using a natural deconvolution and vice versa.

Once the list of targets to stack has been defined, the next step is to remove (or avoid), in an appropriate way, the flux from other non-related or very bright positions in the ALMA maps in order to stay away from contamination produced by these sources.

One way to do that is using a combination of CASA tasks to remove the expected flux from other unwanted or unrelated sources up to a certain flux threshold.

In general, and after several tests, removing bright sources adds extra noise to the maps; the already mentioned procedure increases their noises by around one order of magnitude.

This effect can have its origin in the sensitivity properties of the edges of our maps, which can spread noisy values all over our mosaics. In principle, a method that incorporates this level of noise to the ALMA observations should not be included into the general data processing flow.

Another method to avoid the effect of bright sources from the maps in the stacking procedure is, simply, not using the candidates which are too close to the brightest sources. To get a list of such targets, we used the component lists tools from `CASA` which gather the positions of the brightest sources, $4-\sigma$, from the visibilities plane of our maps and converts it into an `ascii` table. Then, this table can be used in conjunction with the function `search_around_sky` from the `Python` package `Astropy`[1] to look for candidates which are close enough to the bright sources to suffer from eventual contamination from them. Regarding the way ALMA maps are constructed, one criterion to determine the distance at which bright sources do not affect our candidates is related to the size of the synthesized beam of each map.

The distance we chose to establish the limit is five times the major axis of the synthesized beam for each map. This value translates to roughly 5″. We also add an extra criterion to candidates which are still much closer to the already determined brightest sources. Any target which lies closer to 0.5 times the major beam from the synthesized beam from the source position will not be considered as to be close to it but rather be exactly the same source and it will be considered for further calculations.

This second method will discard some candidates from our sample, making it smaller by around a 15%. That corresponds to 410 candidates.

For the reason that we cannot control, completely, the behavior of the maps and their error properties after the sources removal, using the first method is not advised. And, given that with the first method we, in general, increase the noise of the maps which have been processed and well studied, we decided to use the second approach to avoid contamination

[1] `http://www.astropy.org`

from bright sources which have not been labeled as LBG candidates.

3.2 Target final sample

With all of the derived quantities in hand (§2), we now address the selection of the LBG candidates sample, in order to improve the reliability and trustworthiness of the estimated physical properties and stacking results.

We began by discarding a handful (13) of LBG candidates with UV-slopes $\beta < -4.0$ or $\beta > 1.5$ (see Fig. 2.9). These extremely low or high values arise at faint magnitudes, have large error bars, and are physically implausible for LBGs.

Prior to stacking, we also excluded the 410 LBG candidates which are in close proximity but unrelated to any $\geq$4-σ detected sources in the ALMA maps in order to avoid contamination in the stacked signal (§3.1). As already mentioned, we conservatively adopted a circular exclusion region equal to five times the major axis of the natural-weighted synthesized beam for each map (i.e., 3.″2–7.″6). We additionally removed all LBG candidates with primary-beam correction factors lower than 0.5 (see §2.9), as the edges of the ALMA maps have considerably higher noise and other observational artifacts which can adversely affect the sensitivity of the stacking.

Based on the FDR assessment in §2.10, we also identified three (3) LGB candidates associated with ALMA detections at SNR$\gtrsim$4.1, adopting a matching radius of 0.5 times the major axis of the natural-weighted synthesized beam for each map (i.e., 0.″3–0.″8). These sources, along with their key attributes are listed in Table 4.1 and they are not included in the main stacking and have been treated separately. For comparison, the typical positional uncertainties between ALMA and *HST* sources are $\lesssim$0.″1 (e.g., $\lesssim$10% of the beam size; González-López, Bauer, Romero-Cañizales, et al., 2017).

Finally, we considered whether LBG candidates are multiply imaged or not. We do not want to double-count the same source, as this could potentially distort our stacking results. Thus we removed all less constraining multiple images, leaving only the most sensitive image

available for stacking. To determine whether a candidate is multiply imaged, we matched the positions of our LBG candidates against the multiple-image catalogs from the CATS team (v4; see §2.5), which comprise a compilation of secure multiple images found via *HST* and/or ground-based spectroscopic confirmation (e.g., Smith et al., 2009; Merten et al., 2011; Zitrin, Broadhurst, et al., 2011; Zitrin, Meneghetti, et al., 2013; Jauzac et al., 2014; Richard et al., 2014; Kawamata, Oguri, et al., 2016; Caminha et al., 2017; Lagattuta et al., 2017; Kawamata, Ishigaki, et al., 2018; Mahler et al., 2018). In total, we removed 94 LBG candidates with positions conservatively lying within a 0.″5 radius of a known multiple image (63 lie within 0.″1) that had a more constraining multiple-image detection already in our sample.

Another source of multiple images has been developed by Kawamata, Oguri, et al. (2016) and Kawamata, Ishigaki, et al. (2018) which have used information from similar sources as the CATS team as well as multiple images detected from MUSE images of the FFs (Caminha et al., 2017; Mahler et al., 2018).

Since the calculations for the magnification factors have been performed using the information from the CATS team, we considered that avoiding these 94 multiple sources would be enough to limit the eventual contamination from multiple images already detected (not as LBGs).

We summarize our selection criteria in Table 3.1, which resulted in a sample of 1818 LBG non-detected candidates to stack: 404 from A2744; 386 from MACSJ0416; 347 from MACSJ1149; 248 from A370; and 433 from AS1063. For some specific results below, we restrict the sample even further; for instance, when considering stacking in bins of $M_\star$, we only consider 1805 candidates.

3.3 Stacking

To perform the stacking process for our ALMA data, we used the `stacker` code developed by Lindroos et al. (2015). It can stack interferometric data in both `uv` –i.e. visibilities– and image domains. For the image domain, the code uses median or mean stacking with

Table 3.1: LBG Candidate Selection Criteria

Property	Criterion
UV slope	$1.5 > \beta \geq -4$
ALMA pb correction	$pbcor_{\mathrm{ALMA}} > 0.5$
Bright source contamination	$dist_{\mathrm{SNR>4}} > 5 \times b_{\mathrm{maj}}$
FDR detections	$dist_{\mathrm{SNR>3.5}} < 0.5 \times b_{\mathrm{maj}}$
Multiple images	$dist_{\mathrm{mult}} < 0''.1$

weights depending on the user needs and on previously developed stacking methods, as commented in the start of this chapter. These weights can be fixed a priori or obtained from the pb-correction data present in ALMA datasets. The product of this stacking process in the visibility plane is an ALMA measurement set file, `.ms` extension, and an image, `.image` extension, file for the image stacking. The `.ms` file can be processed, if needed, to obtain a `.image` file. Within `CASA`, image files can be exported to `.fits` file if needed and processed as a standard astronomical image.

In the `uv` domain, the stack aligns the phases and then adds up the weighted visibilities following the relation

$$V_{\mathrm{stack}}(u,v,w) = V(u,v,w)\frac{\sum_{k=1}^{N} W_k \frac{1}{A_N(\hat{\mathbf{S}}_k)} e^{\frac{2\pi}{\lambda} i \mathbf{B}\cdot(\hat{\mathbf{S}}_0 - \hat{\mathbf{S}}_k)}}{\sum_{k=1}^{N} W_k} \tag{3.1}$$

in which $\hat{\mathbf{S}}_k$ and $\hat{\mathbf{S}}_0$ are unit vectors pointing to the stacking position and to the phase center of the image, respectively. $\mathbf{B}$ is the baseline of the visibility, W_k is the weight of the stacking position and $A_N(\hat{\mathbf{S}}_k)$ corresponds to the unitless primary-beam attenuation in the direction of $\hat{\mathbf{S}}_k$. For this work, `uv` domain stacking was performed as the main configuration.

As already mentioned, two different weight schemes were applied to the stacking code and further analysis. One uses the magnification-corrected ultraviolet flux and the other, the magnification factor of each source. To generate the weight factor, ALMA sensitivity maps

are also used.

For the UV-flux weight, the factor has the form:

$$W_k^{UV} = \frac{1}{\left(rms^{\rm indiv}_{\rm ALMA,pbcor}\right)^2} \times F_{UV}^2 \tag{3.2}$$

with F_{UV} defined in §2.11 and $rms^{\rm indiv}_{\rm ALMA,pbcor}$ the rms error associated to each target. From the way they are calculated (see Eq. 2.9), they incorporate to the weight the sensitivity of each position in the ALMA maps –the same primary beam correction values used to create the image with Natural *CLEAN*ing method–. This scheme will enhance the contribution from sources which show a higher ultraviolet flux and, by extension, a larger star formation activity. When using the magnification factor as part of the weight, the term is

$$W_k^{\mu} = \left(pbcor^{\rm indiv}_{\rm ALMA}\right)^2 \times \mu^2 \tag{3.3}$$

where μ is the magnification factor. This weight configuration takes advantage of the magnification power of the galaxy clusters. In this way, calculations do not consider intrinsic flux properties but how good the alignment is between the LBG candidate and the observer. Both schemes enhance the contributions from sources with better ALMA sensitivities.

This stacking produces an ALMA visibilities file (`.ms` extension) which can be transformed into an image file (`.image`) with the task `clean`. In this image, and given the manner `stacker` works, all the original baselines have been shifted to the $(u, v) = (0, 0)$ position and, by extension, the imaged data will concentrate its stacked flux in the central pixel if the objects are point-like. If extended sources are part of stacked targets other considerations must be taken into account.

After `stacker` is run for each dataset, every stacked image is inspected to determine if a detection has been achieved. We calculated the detection levels for each stacked image using the procedure described by González-López, Bauer, Romero-Cañizales, et al. (2017), in

which peaks (sources) with SNR > 5−σ are iteratively discarded until we arrive at a stable rms noise value.

On the other hand, to obtain stacked values of IRX, a different method must be employed in which the ALMA observations are not directly utilized. Each individually obtained IRX value will be stacked using the weights and methods presented earlier in this text. Following previous discussions from Bourne et al. (2017) and Koprowski et al. (2018), an appropriate option to determine the stacked IRX values is using the following formula.

$$\langle \mathrm{IRX} \rangle = \left\langle \frac{L_{\mathrm{IR}}}{L_{1600\text{Å}}} \right\rangle, \tag{3.4}$$

where, in our case, we produce a weighted "average" for each sub-sample. For our sample, in bins of redshift, stellar mass and UV-slope and using the median of the subsample rather than the mean to avoid extreme contribution from outliers. In this way, the stacked IRX can be obtained as

$$\overline{\mathrm{IRX}} = \overline{\left(\frac{L_{\mathrm{IR}}}{L_{1600\text{Å}}} \right)} \tag{3.5}$$

We adopt this indicator, since it is nontrivial to know, a priori, how the UV and IR luminosities are related. Thus, we stack the individual IRX values and not the separate luminosities. The calculated IR luminosities are provided using the procedure described in §2.12.

Finally, to investigate the relation between IRX and other parameters, the target stacking was binned as a function of three different quantities; UV-slope, stellar mass, and redshift.

With UV-slope, targets were stacked in the following five bins: $-4.0 \leq \beta < -3.0$, $-3.0 \leq \beta < -2.0$, $-2.0 \leq \beta < -1.0$, $-1.0 \leq \beta < 0.0$ and $0.0 \leq \beta < 1.5$. For stellar mass, targets were stacked in the following nine bins: $6.0 \leq \log(M_\star/M_\odot) < 6.5$, $6.5 \leq \log(M_\star/M_\odot) < 7.0$, $7.0 \leq \log(M_\star/M_\odot) < 7.5$, $7.5 \leq \log(M_\star/M_\odot) < 8.0$, $8.0 \leq \log(M_\star/M_\odot) < 8.5$, $8.5 \leq \log(M_\star/M_\odot) < 9.0$, $9.0 \leq \log(M_\star/M_\odot) < 9.5$, $9.5 \leq \log(M_\star/M_\odot) < 10.0$ and

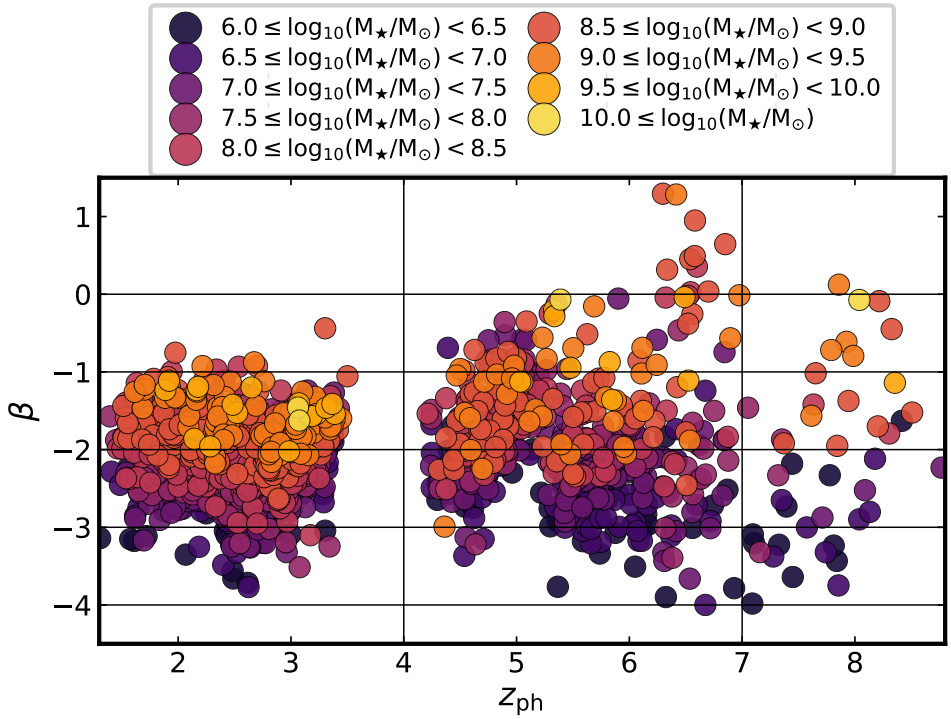

Figure 3.1: Selection of LBG candidates from UV-slope-photometric redshift plane. Color coding indicates stellar mass range in which each LBG candidate lies. Vertical and horizontal lines show divisions between bins in photometric redshift and UV-slope, respectively.

$\log(M_\star/M_\odot) \geq 10.0$. When binning by stellar mass, candidates with stellar masses less than $10^{6.0}$ $M_\odot$ were excluded from stacking calculations because of their very low expected luminosities, which will not only add little to the final stacked results but account for sources that cannot be reached with any existing or projected facility. Finally with redshift, three sub-samples were utilized: $z_{ph} < 4.0$, $4.0 \leq z_{ph} < 7.0$ and $z_{ph} \geq 7.0$. These divisions were adopted considering the apparent distribution of redshift values shown in upper panel of Fig. 2.6.

The choice of bin widths was driven by the compromise of having sufficient numbers of sources to reap the benefits of stacking and span a relatively wide range in parameter space.

With all the divisions, we have 42 bins with LBG candidates. These bins can be seen in Figs. 3.1 and 3.2 along with the five UV-slope bins for low-mass candidates. From Fig.

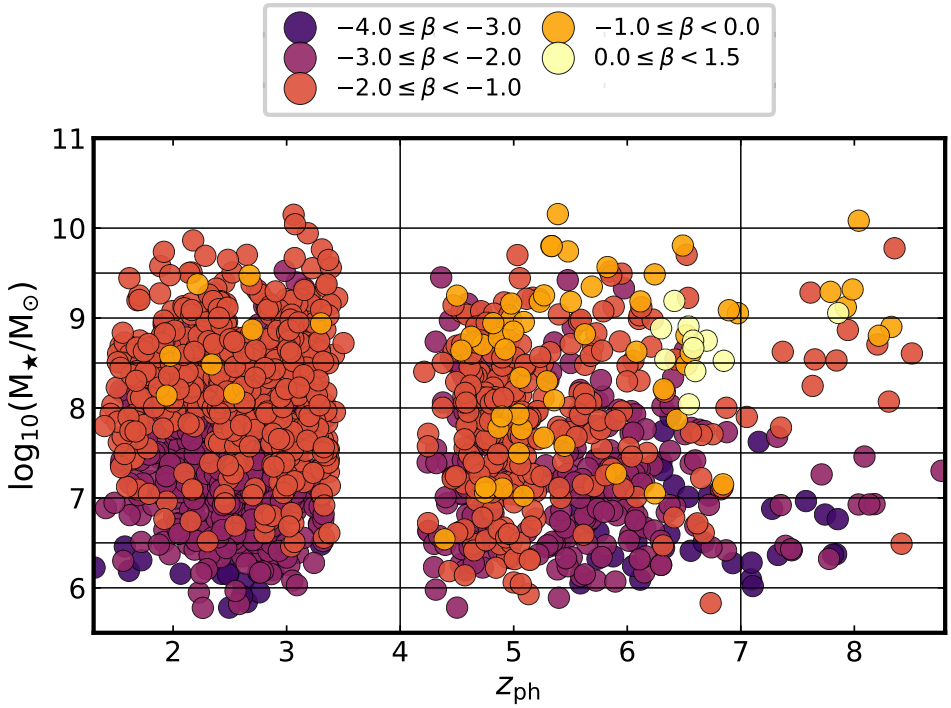

Figure 3.2: Selection of LBG candidates from stellar mass-photometric redshift plane. Color coding indicates UV-slope (β) range in which each LBG candidate lies. Vertical and horizontal lines show divisions between bins in photometric redshift and stellar mass, respectively.

3.2, we can note that only a small fraction of our candidates are not suitable for our stacking procedure and further analyses (13 low-mass sources, less than 1% of the total sample).

4

Results

We describe below the main results obtained for the individually detected sources previously reported in §2 as well as from stacking ALMA data and IRX values of our sample.

4.1 Individual results

With the individual luminosities obtained with the use of the graybody SED and our *HST* photometry, we are able to derive infrared excesses, or their upper limits, and compare them with previously calculated properties for each LBG candidate. Mainly, the comparisons will be performed with the UV slopes and the stellar masses of the targets.

Some properties from our ALMA detections (§3.2) are listed in Table 4.1. And a wider set of properties, for all of our candidates, is listed in the tables of Appendix B. Furthermore, stamps showing their ALMA fluxes and their surroundings can be seen in the figures of Appendix C.

4.1.1 Individual ALMA peak fluxes

The mean and peak distributions of SNR values for our 1821 candidates are shown in Figs. 4.1 and 4.2 respectively. As already mentioned in §2.10, all our targets exhibit SNR values lower than $|\pm 5.0|$. The mean SNR distributions for each redshift bin are centered around ~0 as expected, while the peak SNR distributions are centered around ~1 as a result of selecting the peak pixel which arises within half a beamwidth; this conservatively biases the maximum flux associated with a candidate to higher values. Both distributions appear

Table 4.1: Observed and derived properties for detected LBG candidates.

ID	R.A. [J2000] [hh:mm:ss.ss]	Dec. [J2000] [±dd:mm:ss.s]	cluster	$z_{\rm ph}$	μ	β	$\log(L_{\rm UV}/L_{\odot})$	$\log(L_{\rm IR}/L_{\odot})$	$\log(L_{\rm IR}/L_{\rm UV})$	$\log(M_{\star}/M_{\odot})$	$F^{\rm indiv,obs}_{\rm ALMA,peak,pbcor}$ [μJy]	$\rm SNR^{indiv}_{peak}$
1207	22:48:38.1	-44:32:32.0	AS1063	3.14	3.63	-2.01 ± 0.12	9.62	12.38	2.75	8.39	440 ± 107	4.11
2155	22:48:47.7	-44:32:09.6	AS1063	5.20	2.86	-1.22 ± 0.82	8.79	11.86	3.08	7.07	286 ± 68	4.21
2212	22:48:46.2	-44:31:12.8	AS1063	5.05	40.80	-1.61 ± 0.60	8.66	11.87	3.21	6.50	281 ± 68	4.11

roughly Gaussian. Their peak fluxes are distributed as shown in Fig. 4.3. Most of them are located between ~ -150 μJy and $\sim$250 μJy. They also exhibit one noticeable peak at 50 μJy.

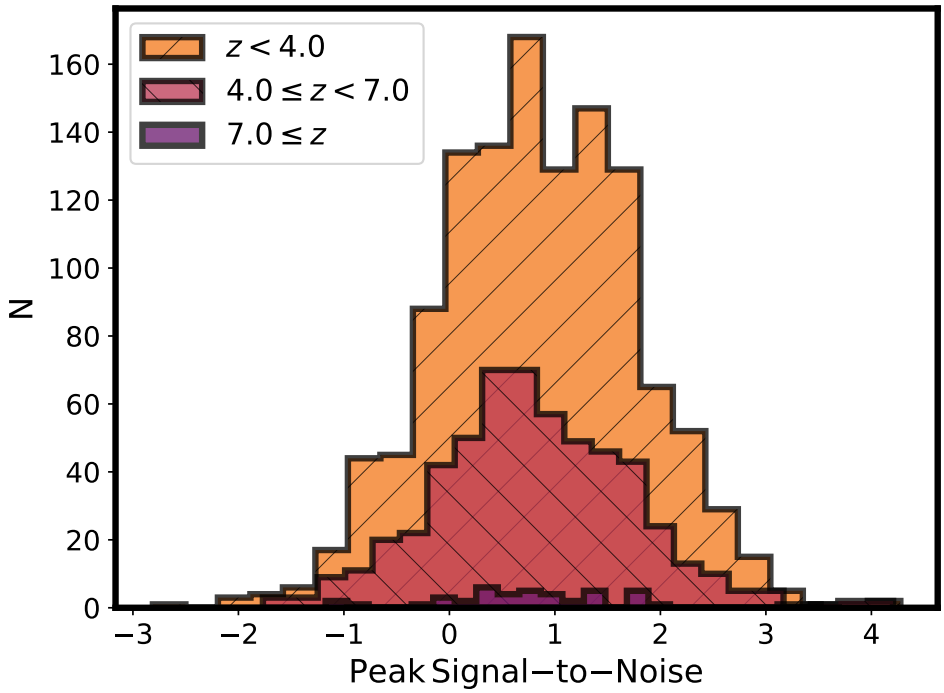

Figure 4.1: Distribution of peak signal-to-noise ratios for our candidates in the ALMA maps. Each sub-sample (represented by a different color) shows LBG candidates within each photometric redshift bin.

From our sample, we find three (3) candidates with $\mathrm{SNR}_{\mathrm{peak}}^{\mathrm{indiv}} > 4.1$ (see Table 4.1). Based on the results from §2.10, we expect about 0.5 candidates out of 3 will be false positives ($\rho_{\mathrm{FDR}} = 0.15$). Thus, with only have three detected candidates, we hardly expect one of them to be a false positive.

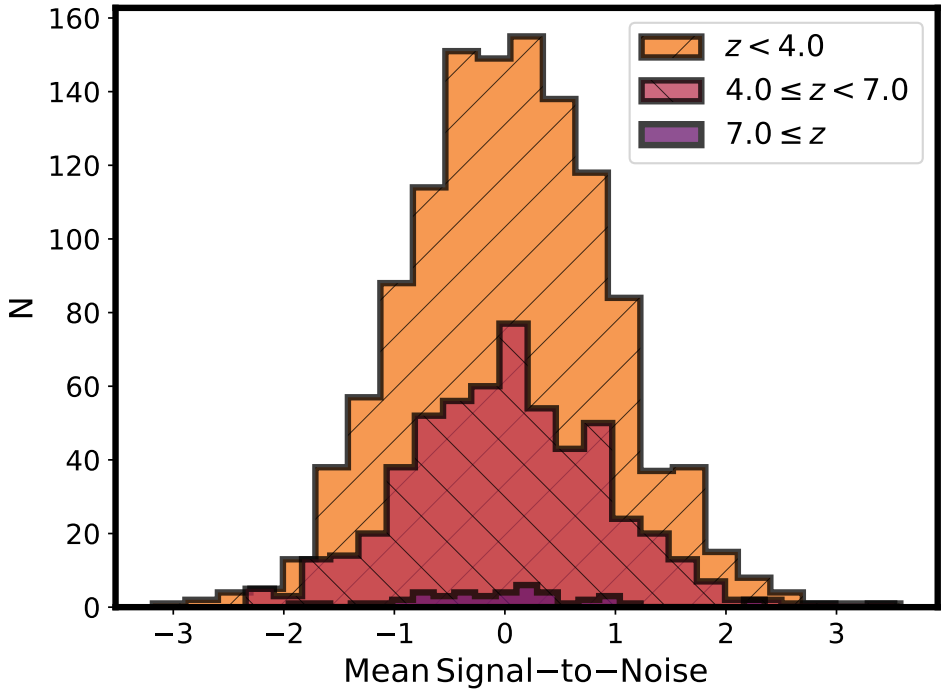

Figure 4.2: Distribution of mean signal-to-noise ratios for our candidates in the ALMA maps. Each sub-sample (represented by a different color) shows LBG candidates within each photometric redshift bin.

4.1.2 Individual UV and IR luminosities

Following the steps described in §2.11 and §2.12, the photometry measurements obtained with *HST* were utilized to calculate UV luminosities for each LBG candidate, and the modified blackbody SED for the IR luminosities. It is important to recall that the IR values have been rescaled to our ALMA peak fluxes with the use of Eq. 2.12.

The distributions of the individual UV and $2-\sigma$ upper limits for IR luminosities are shown in Figs. 4.4 and 4.5, respectively.

For the magnification-corrected UV luminosities, there is a broad peak at around $10^{9.2}\,L_{\odot}$ for the two lower redshift bins ($z < 4$ and $4 \leq z < 7$) and for the higher redshift bin, there is relatively flat source distribution between $10^{8.5}\,L_{\odot}$ and $10^{10}\,L_{\odot}$. For all three bins,

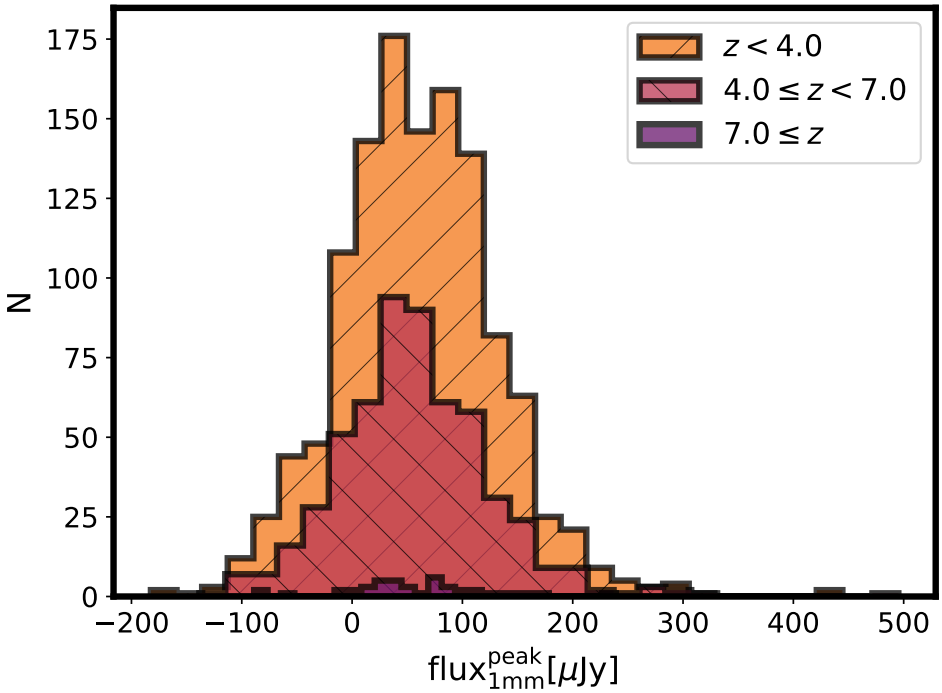

Figure 4.3: Distribution of peak fluxes for our candidates in the ALMA maps. Each sub-sample, represented by a different color, shows LBG candidates within each photometric redshift bin.

the values range from $10^{7.5}\,L_\odot$ to $10^{11}\,L_\odot$, effectively probing apparent SFRs in the range $\sim 0.005-20 M_\odot \mathrm{yr}^{-1}$ (e.g., Calzetti, 2013). We see that the peaks for each redshift range shift to slightly higher luminosities with redshift (but lower UV magnitude, as shown in Fig. 2.9). In the case of the three detections, UV luminosities range from $10^{8.6}\,L_\odot$ to $10^{9.6}\,L_\odot$. In general, the UV luminosities probed here are lower than the values presented in other works (see Narayanan et al., 2018; Reddy, Oesch, et al., 2018).

The magnification-corrected IR luminosity limits of the LBG candidates exhibit a somewhat different behavior from the UV luminosities. Due to the nature of the K-correction on the long wavelength side of the graybody SED, higher redshifts probe somewhat lower IR luminosities. Specifically, we find that the $z < 4$, $4 \leq z < 7$, and $z \geq 7$ bins are centered around values of $\sim 10^{12.2}$, $\sim 10^{11.6}$, and $\sim 10^{11.5}$ $L_\odot$, respectively. And with our imposed

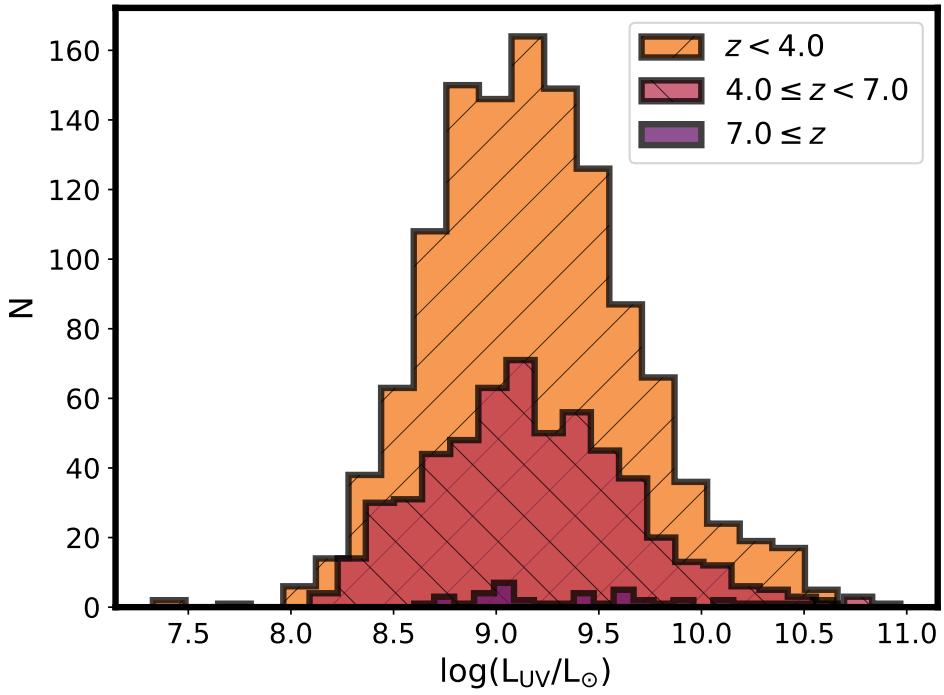

Figure 4.4: Distribution of UV luminosities in our sample. Each sub-sample (represented by a different color) shows LBG candidates within each photometric redshift bin.

maximum magnification of 10, coupled with the relatively uniform *rms* limits, we see that each photometric redshift subsample spans roughly 1 `dex` in luminosity. Thus, the two highest redshift bins probe IR luminosity limits of $\sim 10^{11.2}$–$10^{12.1}\,L_\odot$, or equivalently 30–300 $M_\odot\,yr^{-1}$, while the $z < 4$ bin probes to $\sim 10^{11.7}$–$10^{12.8}\,L_\odot$, or equivalently 90–900 $M_\odot\,yr^{-1}$ (e.g., Calzetti, 2013). Our detected LBGs have IR luminosities which range from $10^{11.8}\,L_\odot$ to $10^{12.4}\,L_\odot$, showing a narrower range than that of the upper limits.

4.1.3 Individual IRX-β relation

After obtaining UV-slope estimates, we compare them to other relevant properties of the LBG candidates in Fig. 4.6, adopting $2-\sigma$ upper limits.

The most prominent trends we see in the IRX-β diagram are with SFR and $M_\star$ (third

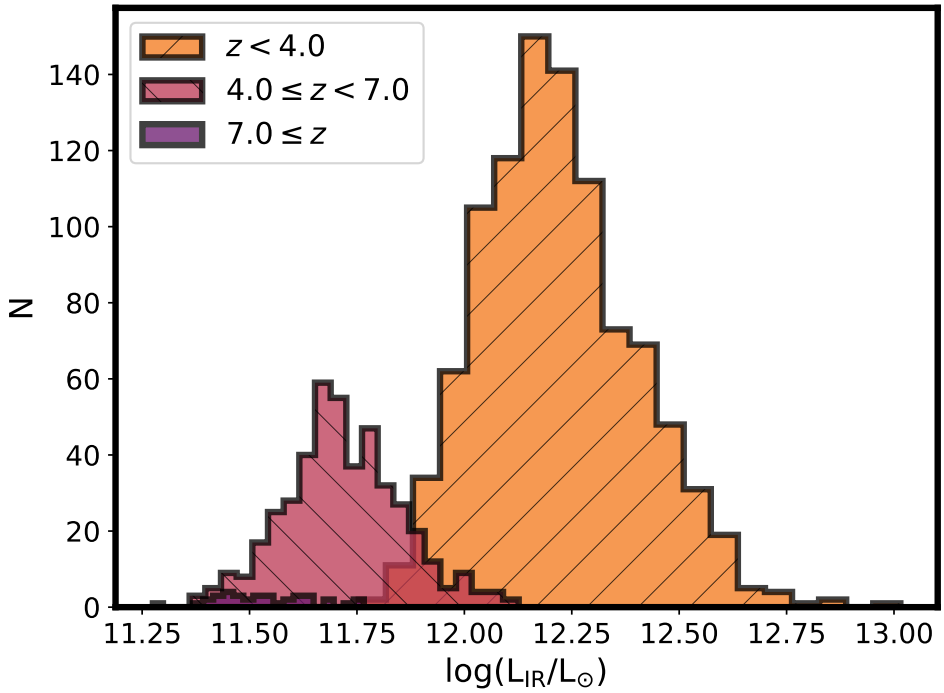

Figure 4.5: Distribution of IR luminosities ($2-\sigma$ upper limits) in our sample. Each of the three sub-samples (represented by different colors) shows LBG candidates within the corresponding photometric redshift bin.

and fourth panels in Fig. 4.6), where higher –lower– upper limits tend to lie to the lower right –upper left– closer –further away– from the local relations, respectively. This is due in part to observation bias, coupled with the $M_\star$-SFR main sequence relation. We detect LBG candidates spanning $\sim 3\,\mathtt{dex}$ in m_{UV} or L_{UV} (bottom panel), while our IR limits only span $1\,\mathtt{dex}$. Thus the highest $M_\star$-SFR sources have the lowest IRX limits, and vice versa. this trend extends into the z_{ph} and μ panels with lower redshift and higher μ sources (i.e., lower L_{UV} candidates) having higher IRX limits, respectively. There appears to be a mild intrinsic trend between higher –redder– β values and higher $M_\star$.

Apart from the individual results, in each subplot, we include four IRX-β relations from previous works presented in §2.13. A large proportion of our candidates lie above the curves, with only ten (10) LBGs located completely below at least one relation. Given the dispersion

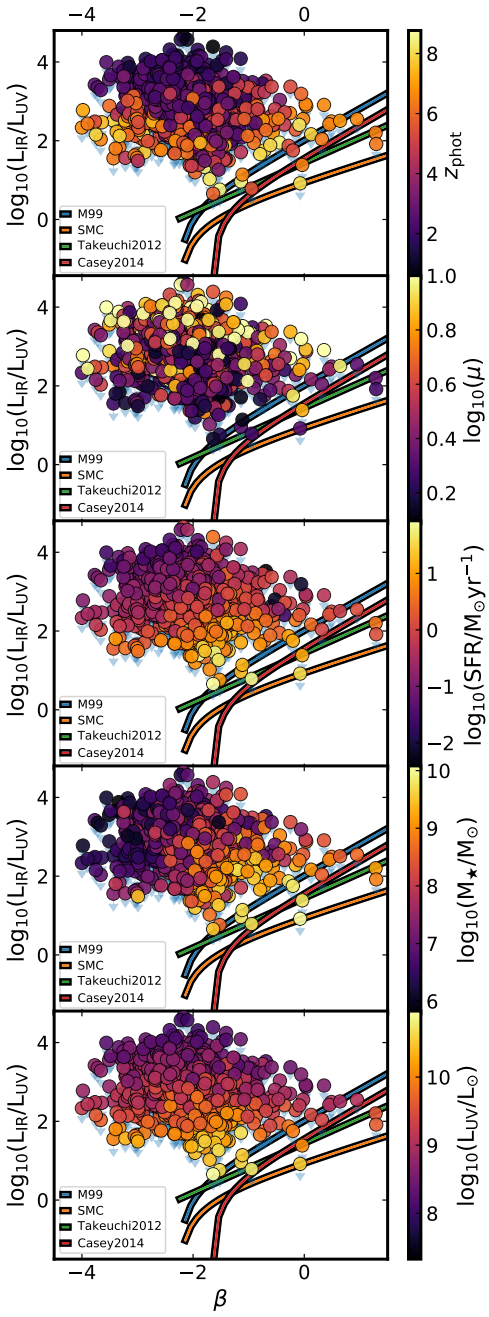

Figure 4.6: Infrared Excess (IRX) 2-σ upper limits vs. UV-slopes (β) for each LBG candidate. Downwards arrow lengths denote the 1-σ errors. From top to bottom, colors represent: photometric redshift (z_{ph}), magnification factor (μ), Star Formation Rate (SFR), Stellar Mass ($M_\star$) and UV Luminosity (L_{UV}). Local relations have been added.

in these local relations, however, all we can say is that our individual limits remain consistent with the relations.

4.1.4 Individual IRX-$M_\star$ relation

To analyze the correspondence between the IRX ratios and the stellar masses derived from FAST++, we can interpret the information represented in Fig. 4.7, which only depicts upper limits. We color-code the LBG candidates as functions of redshift, magnification, SFR, β, and $L_{\rm UV}$.

As in §4.1.3, we see a number of trends in the IRX-$M_\star$ diagram as functions of μ (second panel), SFR (third panel), β (fourth panel), and $L_{\rm UV}$ (fifth panel). Unsurprisingly, higher magnifications allow us to probe lower stellar masses. $M_\star$ is related to SFR and $L_{\rm UV}$ following from the star-formation main sequence. And we now see more clearly a $M_\star$ and β trend, such that more massive systems (which have built up more metals and dust) tend to show higher extinction.

We included, also, the curves for five IRX-M$_\star$ relations from previous works as described in §2.13. Again, the vast majority of our $2-\sigma$ upper limit IRX constraints lie above the relations, with only two objects located below at least one curve. Factoring in the dispersion in these relations, our individual limits remain consistent with the relations. The massive and luminous LBG candidates which lie closest to the relations all have high ($z\gtrsim6$) photometric redshifts and low magnifications, and hence comprise the rare, bright end of the high-z population.

4.2 Stacking results

To gain further insights into the LBG population, we used `stacker` to perform uv-stacking on all five ALMA cluster datasets. We stacked the LBG detections and non-detections separately. As cross-checks to determine if the `stacker` results are behaving as expected, we

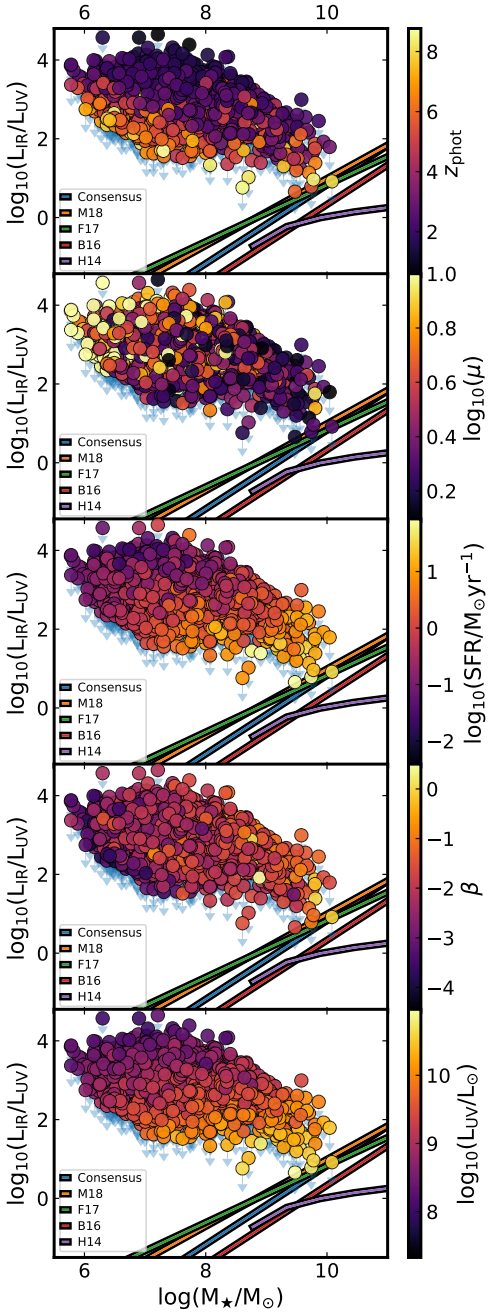

Figure 4.7: Infrared Excess (IRX) 2-σ upper limits vs. stellar masses for each LBG candidate. Downwards arrow lengths denote the 1-σ errors. From top to bottom, colors represent: photometric redshift (z_{ph}), magnification factor (μ), Star Formation Rate (SFR), UV slope (β) and UV Luminosity (L_{UV}). Local relations have been added.

Table 4.2: uv-stacking results for detected LBG candidates.

Weight[a]	$\log(L_{IR}/L_{UV})$[b]	CLEAN[c]	F_{peak}^{stack}[d,e] [μJy]	SNR_{peak}^{stack}[f]
μ	3.19	Natural	257 ± 60	4.28
		Taper	341 ± 82	4.16
F_{UV}	2.76	Natural	273 ± 69	3.96
		Taper	361 ± 173	2.09

[a] Weight associated to each candidate (see §3.3).

[b] Stacked IRX value (see §3.3).

[c] CASA CLEANing method used to obtain the stacked image stamp. [d] Peak flux density within a 0.″5×0.″5 box centered on the average source position in the stacked image.

[e] rms^{stack} derived following Eq. 2.9.

[f] $SNR_{peak}^{stack} = F_{peak}^{stack} / rms^{stack}$.

also performed image-stacking in a very simple manner (with the output files from *CLEAN*ing with CASA) using Python scripts and generated rough IRX (and IR luminosities) predictions based on local IRX-β and IRX-$M_\star$ relations.

Some caution has to be taken, in general, with stacked results (using some weight configuration) since they will be highly biased towards the candidates which have the highest weights in the process. Because of this, weighted stacking can be useful as to show the general trend our candidates follow rather than precise values.

4.2.1 Detected LBGs Stacking

ALMA data and IRX ratios from our three detected LBGs were stacked using both weights described previously. With only three objects before weighting, these stacking constraints are of limited utility.

The uv-stacking results for our three detected LBGs are presented in Table 4.2 and

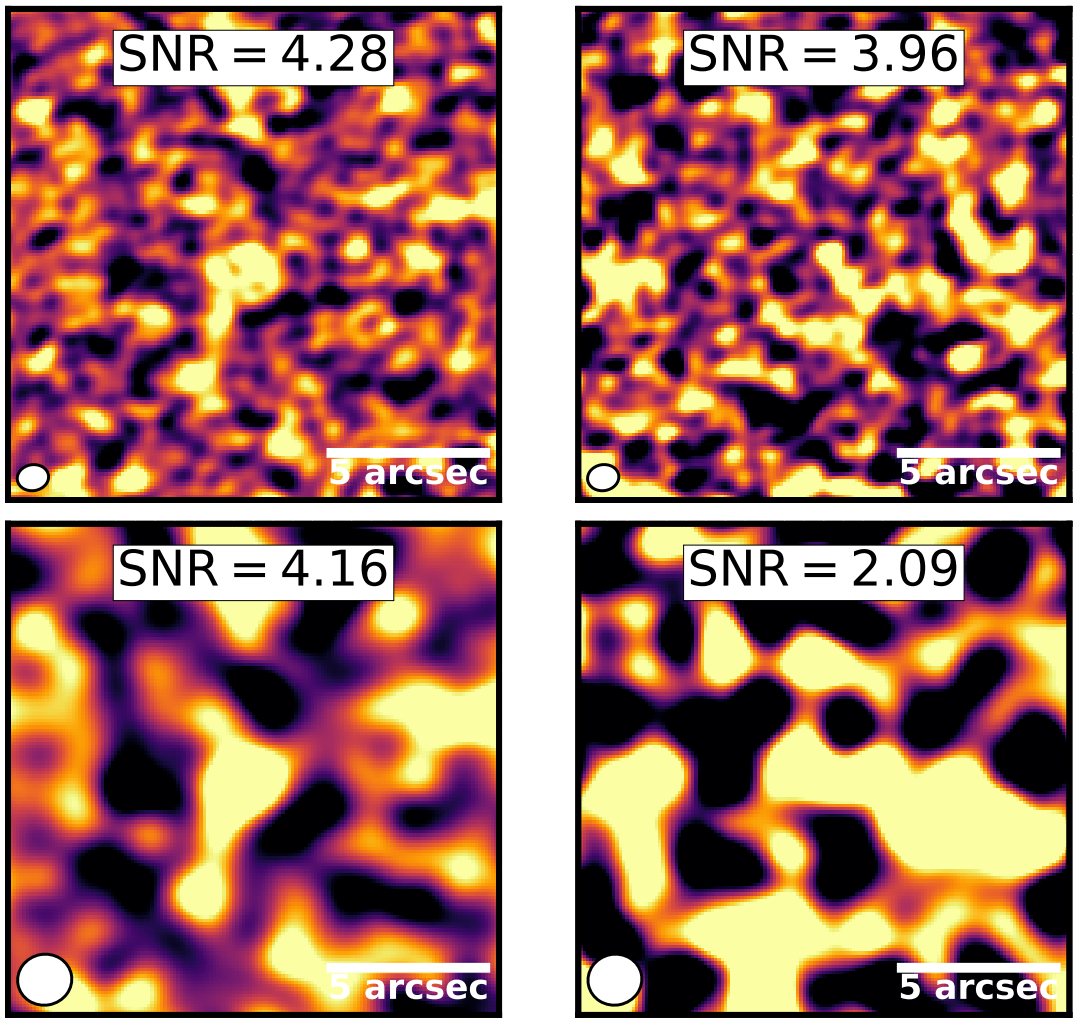

(a) Weight: μ (b) Weight: F_{UV}

Figure 4.8: uv-stacked image stamps for detected LBG candidates, where panels denote specific weighting configurations (*left*: μ; *right*: $F_{\rm UV}$) and CASA *CLEAN*ing procedures (*upper*: Natural; *lower*: Taper). Color scale spans $-100\,\mu$Jy to $+100\,\mu$Jy range. White ellipses represent the synthesized beam size, while white bars in the right corner denote 5″ scale.

Fig. 4.8. We see only very modest decreases in the stacked *rms* over the individual cluster *rms* (Table 2.1), due to the small numbers of sources contributing to the weighted stacked images coupled with the contributions from the PB-corrections. We find that the $F_{\rm UV}$-weighted stack

delivers marginal detection levels, with $SNR^{stack}_{peak} \approx 4.0$ for the natural image and $SNR^{stack}_{peak} \approx 2.1$ for the tapered image. This stack is dominated by the UV-brightest source (~80%), which has a $SNR^{indiv}_{peak} \approx 4.1$. The slightly lower SNR in the stack presumably reflects the fact that the individual values are obtained from arbitrary positions within a half beam of the LBG coordinates (maximum value pixel) and its relatively compact extension on the map. Thus when combining sources, the peak location from this source may be combined with relatively low values from other sources in the stack at that pixel. For the μ-weighted stack, we recover more secure detections, with $SNR^{stack}_{peak} \approx 4.3$ and ≈ 4.2 for the natural and tapered images, respectively. These are higher than the median SNR from the individual sources. This behavior complements the result from the F_{UV}-weighted stack since, the source with the highest μ-weight appears considerably more extended over the ALMA maps. Thus, the likelihood of obtaining stacked pixels with strong detection levels is higher.

Table 4.2 also presents the stacked IRX values for our detected LBGs. From their high infrared luminosities, elevated infrared excesses are obtained, with $\log(IRX) = 3.19$ and $\log(IRX) = 2.76$ for the μ-weighted and F_{UV}-weighted stacks, respectively.

4.2.2 Upper Limits ALMA Stacking

Stacked image stamps for two example configurations are presented in Fig. 4.9 ($4.0 \leq z < 7.0$ and $-4.0 \leq \beta < -3.0$) and Fig. 4.10 ($z \geq 7.0$ and $6.5 \leq \log(M_\star/M_\odot) < 7.0$).

We list the uv-stacking results for several different configurations in target binning we used –photometric redshift, stellar mass and UV-slope– in Tables A.1, A.2, and A.3 of Appendices A.1 and A.2, respectively.

As expected, there is a noticeable reduction in the rms errors for all stacked images which contain more than a few sources, and these are generally lower than the smallest rms from the individual maps. With the large number of undetected LBG candidates in some bins, we achieve stacked *rms* values as low as $\approx 5\,\mu$Jy. This highlights the power of stacking to reduce the errors and increase the signal accordingly by $\sim \sqrt{N}$.

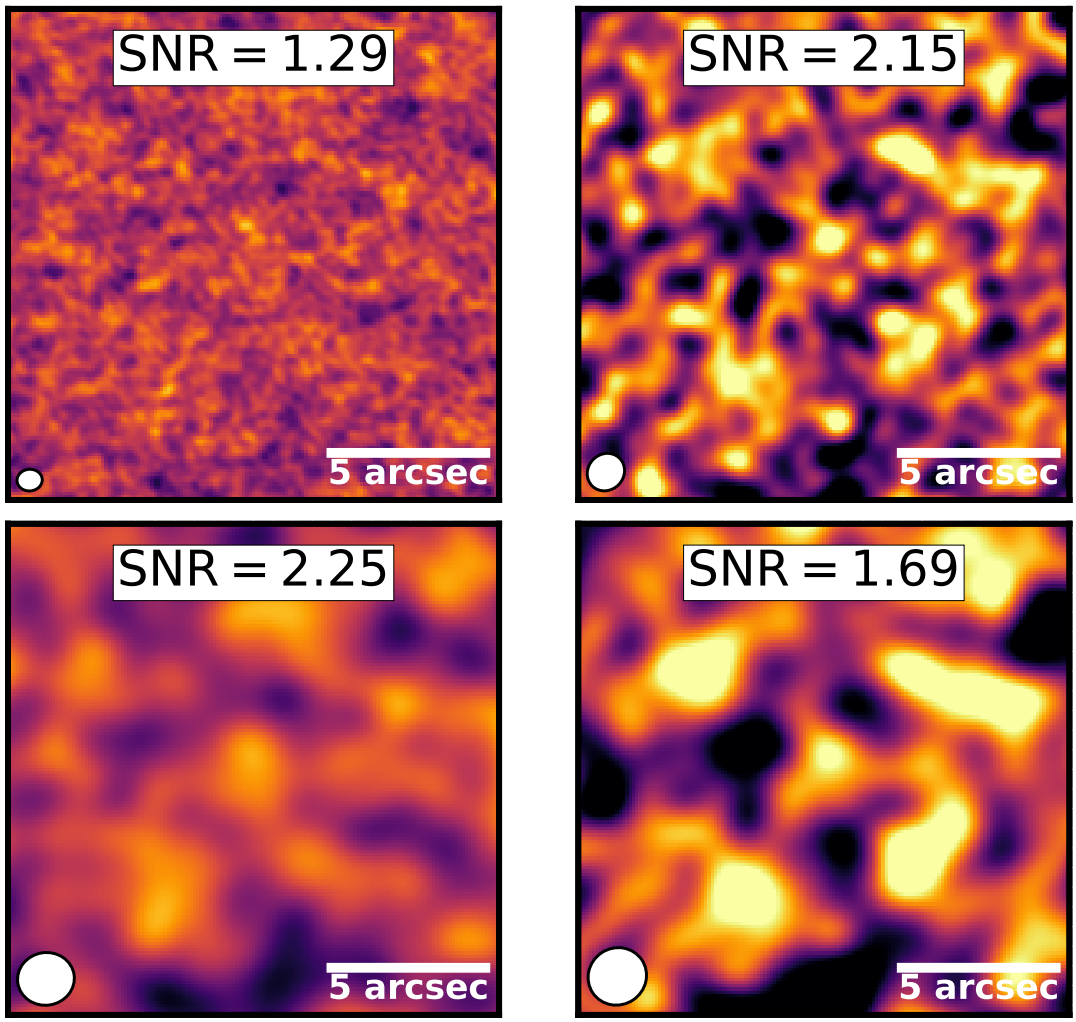

(a) Weight: μ (b) Weight: F_{UV}

Figure 4.9: Example stamps from uv-stacked LBG candidates using one specific UV-slope and z_{ph} –−4.0 ≤ β < −3.0 and 4.0 ≤ z < 7.0–. Upper row shows images using Natural CLEANing in `CASA` and lower row exhibits images with Taper CLEANing. Panels denote specific weighting configurations (*left*: μ; *right*: $F_{\rm UV}$) and CASA *CLEAN*ing procedures (*upper*: Natural; *lower*: Taper). Color scale spans −100 μJy to +100 μJy range. White ellipses represent the synthesized beam size, while white bars in the right corner denote 5″ scale.

An important detail to highlight is related to the signal enhancement that stacking can produce. Given that our method to obtain peak fluxes (cf. §2.10) involves looking for the

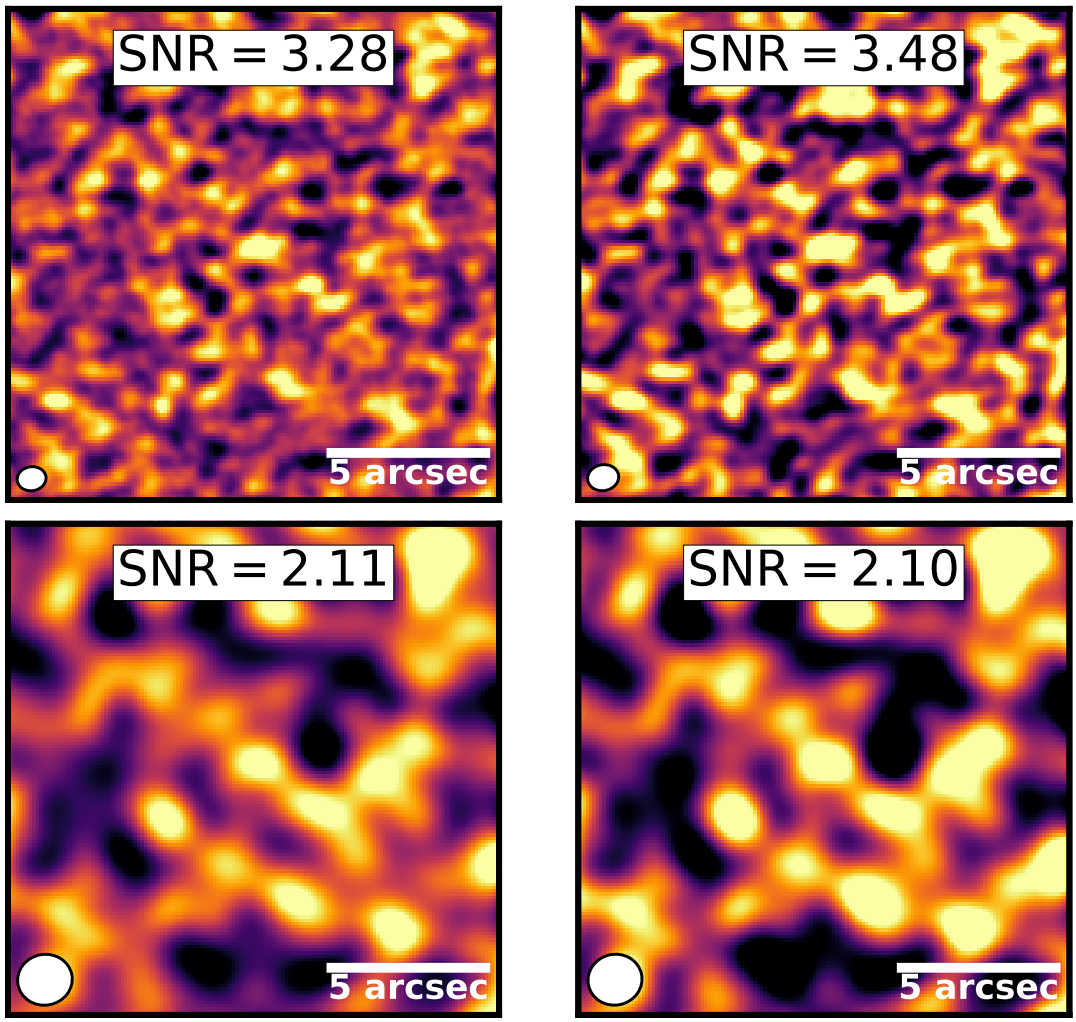

(a) Weight: μ (b) Weight: F_{UV}

Figure 4.10: Example stamps from uv-stacked LBG candidates using one specific Stellar Mass and z_{ph} –7.0 $\leq \log(M_\star/M_\odot) <$ 7.5 and $z \geq$ 7.0–. Panels denote specific weighting configurations (*left*: μ; *right*: $F_{\rm UV}$) and CASA *CLEAN*ing procedures (*upper*: Natural; *lower*: Taper). Color scale spans $-100\,\mu$Jy to $+100\,\mu$Jy range. White ellipses represent the synthesized beam size, while white bars in the right corner denote 5″ scale.

brightest pixel within a box, SNR values will not be obtained from the exact same position for each source. As a consequence, stacked SNR levels do not scale directly with each of the individual targets. With this in mind, after stacking ALMA upper limits, we find that none of

our β or $M_\star$ stacked bins result in clear detections. From Tables A.1 and A.1 and A.3, there are only a few bins with even a marginally significant result (i.e., SNR~3.5): 13 $z_{\rm ph} \geq 7.0$ targets with UV-slopes between $-2.0 \leq \beta < -1.0$ with μ weighting for Natural *CLEAN*ing; 8 $z_{\rm ph} \geq 7.0$ targets with stellar masses between $6.5 \leq M_\star/M_\odot < 7.0$ with $F_{\rm UV}$ weighting for Natural *CLEAN*ing.

4.2.3 Stacked IRX-β relation

Figure 4.11 shows the results of the stacking of the IRX values with respect to β bins and separated by photometric redshift ranges. For the sake of completeness, we also plot the ALMA detected LBG candidates alongside the stacking results and data for three local star-forming galaxies: M82 (Förster Schreiber et al., 2003; Dale et al., 2007; Greco et al., 2012), NGC7552 (Dale et al., 2007; Wood et al., 2015) and NGC7714 (González Delgado et al., 1999; Brandl et al., 2004; Brown et al., 2014). These local galaxies have a range of $\rm M_\star \sim 10^{8.7}$–$10^{10.7}$ $\rm M_\odot$ and SFR~1–10 $\rm M_\odot\,yr^{-1}$, with M82 being perhaps the most reasonable "match" to the more massive LBG candidates. Some β bins do not show points because there are no candidates which meet those redshift and β requirements. Related to the same issue –not enough number of candidates in some bins–, lower-β bins tend to show higher IRX limits because there are not enough sources to lower the IR luminosities, and, by extension, the stacked IRX values.

The detected LBG candidates generally have lower UV-slopes (less extinction), much lower stellar masses, and higher or comparable IRX values to the local objects. The limits for the $F_{\rm UV}$-weighted limits are systematically lower than the detections and show similar or lower IRX values than the local objects despite having similar stellar masses.

In all three redshift bins, we see that the $F_{\rm UV}$-weighting produces much lower median IRX constraints than the μ-weighting. This is perhaps no surprise, given the previously mentioned correlation between stellar mass and $L_{\rm UV}$ (or equivalently $F_{\rm UV}$ over limited redshift ranges) in §4.1.4. Indeed, the most massive and UV-luminous LBG candidates in Fig. 4.6 are

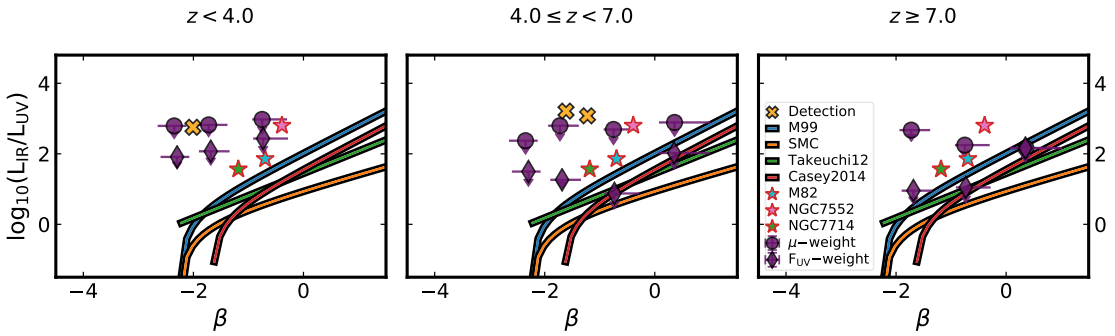

Figure 4.11: Stacked 2−σ infrared excess ratios upper limits vs. UV-slopes. Circles show the use of magnification factors and diamonds, the use of UV fluxes as weights (see §3.3). Each panel shows results for each bin in photometric redshift along with data points for local star-forming galaxies (M82, NGC7552 and, NGC7714). Downwards arrows show 1-σ errors in IRX. Horizontal errorbars indicate limits of the 16th and 84th percentiles of the β distribution in each bin. Yellow crosses show individual ALMA detections.

the ones with limits closest to the local relations. In contrast, the individual high magnification LBG candidates generally have high IRX values, and thus the stacked bins generally lie well above the $F_{\rm UV}$-weighting ones. Likewise, the lowest β bins ($\beta < -2$) have systematically higher IRX limits, mirroring the trend seen in the individual limits of Fig. 4.6.

The $F_{\rm UV}$-weighted limits at $z < 4$ remains well above the local IRX-β relations, demonstrating that at least 1-dex deeper IR constraints are needed to start placing meaningful constraints on even the most luminous z~2–4 LBGs, and 2–3 dex more for the bulk of the population. At higher redshifts, the results appear more encouraging, as the limits on the most UV-luminous objects are approaching those of the local relations. Unfortunately, the low numbers of sources in these high-redshift bins mean the results are subject to small number statistical uncertainties, and thus we can solely say that they remain marginally consistent with the local IRX-β relations at the depths we probe.

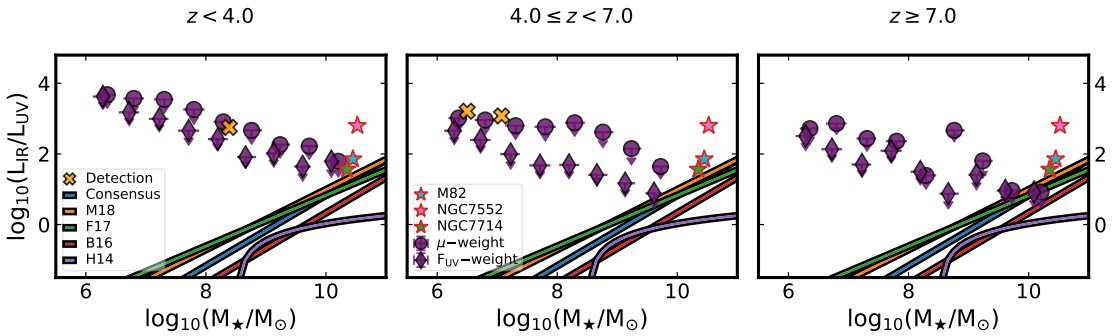

Figure 4.12: Stacked 2−σ infrared excess ratios upper limits vs. stellar mass. Circles show the use of magnification factors and diamonds, the use of UV fluxes as weights (see §3.3). Each panel shows results for each bin in photometric redshift along data for local star-forming galaxies (M82, NGC7552 and NGC7714). Downwards arrows show 1-σ errors in IRX. Horizontal errorbars indicate limits of the 16th and 84th percentiles of the $M_\star$ distribution in each bin. Yellow crosses show individual ALMA detections.

4.2.4 Stacked IRX-M$_\star$ relation

In Fig. 4.12, the results of the stacking of the IRX values are shown with respect to stellar mass bins and separated by photometric redshift ranges. For the sake of completeness, we also plot the ALMA detected LBG candidates alongside the stacking results.

Mirroring the individual trends found in §4.1.4, we see that lower stellar mass bins generally have higher IRX limits across all redshift ranges. This is related to the fact that $M_\star$ correlates with SFR, and hence LUV, following from the star-formation main sequence, as well as to the relative numbers of LBG candidates used.

An important point to highlight is that, just as mentioned in the previous section, stacking with μ-weighting gives higher IRX values than F_{UV}-weighting in general.

Again, the most massive and UV-luminous LBG candidates in Fig. 4.12 are the ones with limits closest to the consensus relations in each redshift regime. At the moment, our limits remain consistent with these relations, and IR limits at least 1-dex deeper will be needed to start placing meaningful constraints on the current consensus relations.

5

Discussion

5.1 Individual constraints

If we analyze the properties from our sample (UV-slope, stellar mass, UV magnitude), we can for instance compare their distribution with that from B16, where 330 LBGs were studied and six "detections" were obtained with ALMA observations. In their Fig. 2, they present the histograms for these properties as a function of drop-out bins. For the β values, a peak near $\beta \sim -2.2$ can be seen in their and our (Fig. 4.4) sample and the shapes of the overall distributions are analogous. The bulk of both distributions are located in the range $-3.5 \lesssim \beta \lesssim 0.5$.

For the stellar masses, both distributions (our and B16; see Fig. 2.11) peak at a similar value around $\log(M_\star/M_\odot) = 8$. However, our sample effectively probes one order of magnitude lower than B16 due to the magnifying power of galaxy clusters.

In the case of UV apparent magnitudes, our magnification-corrected magnitudes (upper histogram in Fig. 2.9) show a somewhat different arrangement from that in B16. Although both samples start at very similar magnitudes ($m_{UV} \sim 24$), our candidates reach two magnitudes deeper ($m_{UV} \sim 32$) than the ones from B16, which again is explained with the use of highly-magnified fields. One similarity both sets bear is related to the peak values. Data from B16 peaks in a range of magnitudes ($28 \lesssim m_{UV} \lesssim 29.5$). Interestingly, our low-redshift sample peaks at $m_{UV} \sim 28.5$ and the mid-redshift bin has its peak at $m_{UV} \sim 29.5$.

5.1.1 Detected LBGs

It is disappointing that so few of the LBGs are detected outright in the Frontier Fields sample, despite the potential opportunities for strongly lensed signals. Overall, we detect only three sources with SNR$\gtrsim$4.1, all from the AS1063 field. The latter fact may imply that these detections are an unusual anomaly rather than representative of the LBG population as a whole. With so few sources, the stacking results do not provide any insightful information. The non-detections in the other fields, particularly from ASPECS (B16) hints at the fact that the intrinsic IR emission from these objects is likely to be quite faint. Our results are consistent with many past works (Bouwens, Aravena, et al., 2016; Casey, Scoville, et al., 2014; Fudamoto et al., 2017; McLure et al., 2018; Takeuchi et al., 2012; Álvarez-Márquez et al., 2016; Heinis et al., 2014; Barisic et al., 2017; Bowler, Bourne, et al., 2018; Bourne et al., 2017).

Regardless of their scarcity, some comments can be still made on our detections. Stacked IRX values are depicted in Figs. 4.11 and 4.12. Given that they are detections, the IR luminosities they show are higher than an important fraction of our sample. For this reason, they appear in the upper regions of the plots.

5.1.2 Upper Limits and previous works

IRX-β and previous results

Figure 4.6 shows the distribution of our sample over the IRX-β plane color-coded by five different quantities. Along with this distribution, we included four different relations from past works which have been described in §2.13: M99 IRX-β relation by Meurer et al. (1999), SMC IRX-β relation (Smit et al., 2016), Takeuchi et al. (2012) and Casey, Scoville, et al. (2014) relations.

We can see that a large proportion of our candidates lie well above the relations already mentioned. Only ten (10) points are located below, at least, one of the curves. And only one of these lies beneath the SMC IRX relation. This shows that most of our upper limits are

compatible with all our studied IRX-β relations. It is pertinent to mention that the candidates situated between M99 and SMC relations have high photometric redshifts; they are in the interval $z_{\rm ph} = 5.36-7.84$ with a mean value of $z_{\rm ph} = 6.25$ and four of them show, exactly, the same photometric redshift: $z_{\rm ph} = 6.32$. The UV luminosities from these candidates lie in the rightmost side of their distribution –i.e. they tend to have higher ultraviolet luminosity values– and the contrary happens with their IR luminosities. The combination of both behaviors leads to having lower IRX values and, thus, being below some of the previous IRX-β relations.

Targets which lie below $\beta = -2.23$, which represents the intrinsic, non-dust-obscured, UV-slope value from Meurer et al. (1999), cannot be compared directly with the mentioned relations as they do not cover the same region of the parameter space. Previous relations were developed from sources which have UV-slopes values higher than the intrinsic value $\beta = -2.23$ and, as mentioned in §2.13, from local galaxies. Another reason to avoid a proper analysis of the candidates with low UV-slope values is our impossibility to reach targets with a combination of low UV-slopes and low IR luminosities with the currently available instrumentation. We do not have the capabilities to study the behavior of LBGs for very low β values and, eventually, extend known relations.

In addition to those barriers, having mostly upper limits makes the construction of a fit for our data more challenging than with regular data points. For this reason, we do not attempt the search for a mathematical expression of the correlation between IRX and β as well as $M_\star$.

Regarding a possible evolution of the IRX relations with redshift –as mentioned, for instance, by F17–, and given that most of our sources are IRX upper limits, it is not possible to establish a bona fide relation for their values as a function of redshift. We can only observe (uppermost panels in Figs. 4.6 and 4.7) that, roughly, upper limits with lower redshifts tend to exhibit higher IRX ratios. From this, the only viable interpretation is that our sources do not contradict what other works have concluded.

The sole feature it is possible to comment about low-β candidates is that they display, as a whole, the lack of targets with low IRX values. This might be a consequence of the

deficiency of bluer targets with, also, high enough infrared luminosities.

It is also possible to compare our upper limits in the IRX-β space with the values found by Salim and Boquien (2018). They examined more than 20,000 low-redshift galaxies ($z < 0.3$) from GALEX-SDSS-WISE Legacy Catalog 2 (GSWLC-D2). The loci of their galaxies in the IRX-β plane is consistent with an important fraction of our sample. More importantly, the presence of some of our upper limits for high β sources below M99 indicates a very good match with their results. This situation is not replicated with other works considered here –Takeuchi et al. (2012) and Casey, Scoville, et al. (2014)– in which their sources with $\beta > 0$ have higher IRX ratios. We can see that the sample used by Salim and Boquien (2018) is located, mostly, below M99 and it shows a less abrupt slope for galaxies with $\beta \gtrsim -0.5$ than that from the relations presented in 2.13. Our upper limits also exhibit this behavior but the only effect we can extract is that we put some constraints that can push previous results at high-redshift objects in the same way that Salim and Boquien (2018) do for local galaxies. In addition to this, we highlight that a significant minority of their sample are located above previous relations in the range $-2.0 \lesssim \beta \lesssim -0.5$. As mentioned in §4.1.3, we obtained 10 upper limits lying underneath M99 but only two of them cover the mentioned range in β. Despite their low number, they allow us to put relevant constraints and create some mild tension over that fraction of the local sample from Salim and Boquien (2018).

IRX-$M_\star$ and previous results

Individual results for IRX values vs. stellar mass are shown in Figure 4.7. Along with them, we have plotted five relations which come from previous works (F17; M18; B16; H14described with detail in §2.13). These relations have been depicted from a stellar mass value of $\log(M_\star/M_\odot) = 6.0$ since our stacking bins have the same starting point and the works already mentioned start their studies from that value and above.

It is relevant to mention that all but two upper limits lie above the curves. Two other points, which have the highest stellar masses, are close to the IRX-$M_\star$ relations. And, just as

the observed behavior with the UV-slope, candidates with lower stellar mass values do not reach to as low infrared excesses as their higher mass counterparts.

For the same reasons exposed in §5.1.2, we have not tried to fit a curve to our upper limits.

Most of the recent works shown here agree on the fact that star-forming galaxies up to around z∼3–4 follow more closely the M99 IRX-$M_\star$ relation than an SMC-like curve. Our IRX-$M_\star$ upper limits show that, for high β bins ($\beta \gtrsim -1.0$), the M99 relation is pushed strongly for higher photometric redshift bins. This is patent for some bins stacked with $F_{\rm UV}$ as weights. They go low enough to be more compatible with the SMC curve –as it has been suggested, for instance, by Koprowski et al. (2018) and Fudamoto et al. (2017)–.

Despite the fact that B16 have, in general, similar distribution in such important properties, the obtained results are not that similar in terms of how deep in IRX values we reach.

Individual upper limits from B16, their individual upper limits do not go higher than $\log(\mathrm{IRX}) = 2.8$ for their z∼2−3 sub-sample and $\log(\mathrm{IRX}) = 1.9$ for the z∼4−10 galaxies while our candidates reach higher infrared excess ratios by ∼1.5 `dex` for our $z < 4.0$ and $4.0 \leq z < 7.0$ bins and by ∼0.5 `dex` for the $7.0 \leq z$ LBGs. Regarding the lower part of the IRX distribution, our low redshift sample ($z < 4.0$) is located above the respective bin from B16 by ∼1.0 `dex` for all our bins.

Comparing our limits with what has been obtained by F17, we can notice that our IRX upper limits, for comparable β and $M_\star$ ranges, can reach ∼0.5 `dex` higher than their sources. Since they have similar noise levels for the ALMA observations, this discrepancy can be explained from the fact that their sample is composed of sources with higher stellar masses ($M_\star \sim 10^{10.7} M_\odot$). Our lower values are translated into lower L_{UV} which, as a consequence, return higher IRX ratios.

5.1.3 $M_\star$-β correlation

As mentioned in §4.1.4, we see a fairly clear trend between $M_\star$ and β. To place this in better context, we plot in Fig. 5.1 the relation between UV-slope and stellar mass directly for our sample. Under the assumption that all star-forming galaxies have similar intrinsic UV slopes, M18 used the values of β as a proxy for the UV attenuation (A_{1600}). They fit a third-order polynomial to a mass-complete sample of star-forming galaxies selected from the HUDF (with stellar masses in the range $8.5 < \log(M_\star/M_\odot) < 11.5$, with a 1.1mm depth of 35μJy beam^{-1}) and obtained the relation plotted in the dashed blue line in Fig. 5.1.

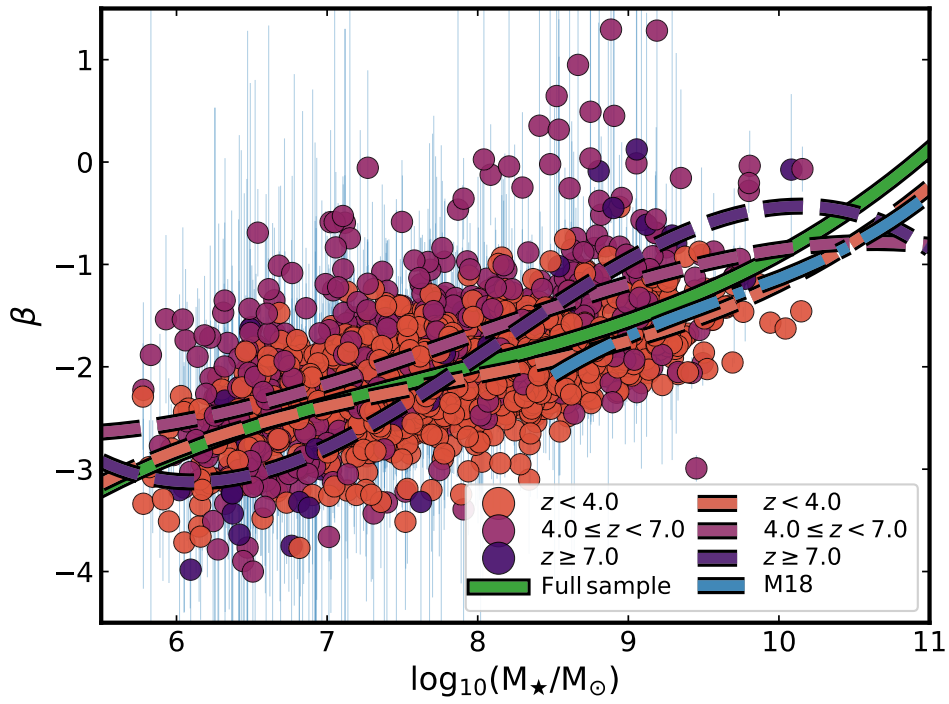

Figure 5.1: UV-slope (β) vs. stellar mass ($M_\star$) for our selected LBG candidates. Colors represent our bins in photometric redshift (both point and polynomial fitting lines). Blue dashed line represents fit from M18 for their sample with stellar masses $\log(M_\star/M_\odot) \geq 8.5$ and green solid line shows our third-order polynomial fit (Eq. 5.1).

We performed the same experiment using our full LBG sample down to a mass of

log ($M_\star/M_\odot$)=6.0. We caution that this limit is likely substantially below the nominal mass completeness threshold in the HFFs, which should be similar to that of the HUDF at $z\sim3$ (e.g.,$\gtrsim10^{8.5}\,M_\odot$; see Fig. 2.11). Due to the lensing amplification, we do expect to find at least some representative sources among the lower mass LBGs in our sample, but we could have strong selection effects that bias the resulting fitted relations at low stellar masses.

Nonetheless, applying a third-order polynomial fit to our $M_\star$ and β values, we find

$$\beta = -0.901 + 0.809X + 0.189X^2 + 0.027X^3, \tag{5.1}$$

in which $X = \log(M_\star/10^{10}M_\odot)$. Similar exercises were performed binning the sample in our adopted redshift bins. The $z < 4.0$ trend is nearly identical to the full sample, due in large part to the fact that such low-redshift sources account for the majority of our sample (1221 candidates). However, the trends found for the higher redshift bins remain consistent within the dispersion. Within the mass-complete range of $8.5 \lesssim \log(M_\star/M_\odot) \lesssim 10$, our fits appear to be consistent with that of M18, particularly in the low-redshift bin (within 0.25 dex), which is most comparable to the range they studied.

Pushing below stellar masses of $\sim10^{8.5}\,M_\odot$, we observe a smooth trend toward lower (bluer) β values, consistent with expectations from increasingly metal-poor stellar populations.

5.1.4 Candidates with $\log(M_\star/M_\odot) < 6.0$

When using stellar mass bins for the stacking, we only considered LBG candidates for which their value was higher than $10^6 M_\odot$. This was because we only wanted sources that were available to be detected, at least slightly, with an instrument as ALMA and to compare them with previous relations which have been developed for higher stellar masses.

From the 1818 non-detected candidates in our initial sample, 13 of them are in this low-mass range and were not considered for the results shown in §4.2 –which takes only 1805 candidates into account–. Regarding photometric redshift bins, eight of our low-mass

candidates have a z_{ph} below 4.0, five of them are in the range $4 \leq z_{ph} < 7.0$ and none of them have a photometric redshift higher than 7.0.

These candidates can be stacked in the same manner as the other samples –i.e. different weights and *CLEAN*ing methods–. The results of the uv-stacking are summarized in Table A.4. In general, the flux levels found after this process are not enough to consider them useful for our purposes. The highest obtained signal-to-noise ratio is 0.78 for mid-redshift candidates with Natural *CLEAN*ing. This confirms our initial decision of not using them for the stellar mass stacking.

5.2 Stacked properties

We can compare our stacked limits with other works. Stacked sources from B16 show IRX values which go as low as $\log(\mathrm{IRX}) = -0.2$ for upper limits and $\log(\mathrm{IRX}) = 0.5$ for detections. As it can be seen in Figs. 4.11 and 4.12, our stacked excessess can reach ~1.0 dex higher. Part of the factors that can have an effect on the large difference are associated to the depth in the ALMA and HST data they reach. Our noise levels for the ALMA observations of the five clusters go from 55μJy to 71μJy whereas B16 have a rms value of 12.7μJy (at least, four times lower than our deepest map). Thus, they have access to lower values in IR luminosities which, in turn, lead to lower IRX limits.

5.2.1 Considerations on stacking weighting

After stacking our data, we can, certainly, retrieve information from deeper objects and their properties. In spite of that, the obtained values have to be regarded with some reservations. Since we need to define the necessary weights to apply either a median or mean to the desired properties (see §3.3), any stacked result will be biased towards the candidates with the highest weights.

As a way to illustrate this mathematical effect, we can describe the case of IRX stacking

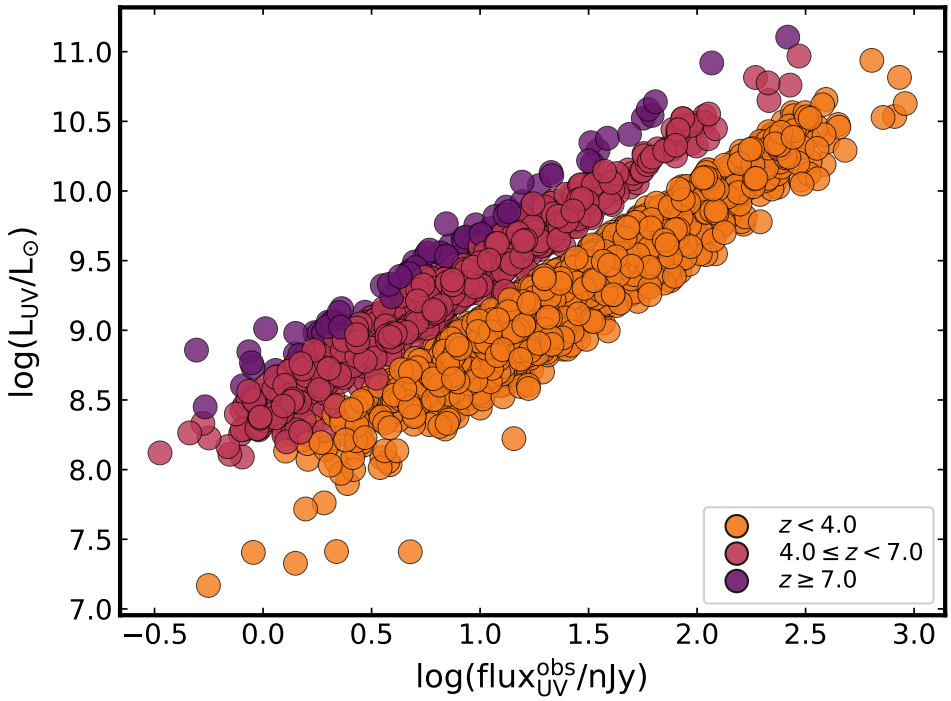

Figure 5.2: UV luminosities (§2.11) vs. UV fluxes (see §2.6) from our LBG sample. Colors represent the photometric redshift subsample of each candidate.

with UV fluxes as weights. Since there is a correlation between UV fluxes and UV luminosities (see Fig. 5.2), we can expect that stacking results will be skewed towards the candidates with higher UV fluxes and, thus, higher UV luminosities. This will result in lower stacked IRX values, which is not, necessarily, an expression of the behavior of most LBG candidates.

For this reason, any stacked IRX value has to be considered as a manifestation of the influence of the candidates with the highest weights and not as a true expression of the overall trend from the full studied sample.

In the same line, using different weighting and binning schemes can lead to several signal enhancements. We can deduce, from those results, that when using the appropriate blend of weights and bins, it is not completely necessary to have a large set of targets to reach acceptable signal levels. This has, as a downside, that reaching a useful signal level is the

result of an ad-hoc solution for the stacking and not the outcome of a standard procedure.

5.3 LBG density

To assess the quality of the sample we have examined, we calculate, roughly, the density of LBGs per angular area. The use of highly magnifying clusters affects the way background sources are observed. Thus, we need to obtain the source-plane observed area rather than the image-plane area to compute the desired density. A simple method to calculate this is through "demagnification" of each individual LBG surrounding area. For each candidate, we assume an area equal to the size of the synthesized beam of every ALMA map centered on their positions. Then, we divide this value by the magnification factor to retrieve the area of the observed LBG in the source plane. After this, we add all the individual LBG areas up to obtain a value which can be compared with that of the image plane. Finally, the ratio between the image and source planes areas can be utilized to retrieve an estimate of the total source plane area covered by our ALMA observations.

From this procedure, we obtain that the image-plane area covered by our observations is 2.86 times the source-plane area. Translating this into our full maps and recalling that each of HFF clusters was covered by a $\approx 2\farcs1 \times 2\farcs2$ ALMA mosaic (González-López, Bauer, Romero-Cañizales, et al., 2017), the effective source-plane area covered by us is $\approx 1\farcs24 \times 1\farcs3$ per cluster. This makes a total area of $\sim$8 arcmin^2, in contrast with the $\sim$23 arcmin^2 image-plane area reported by González-López, Bauer, Romero-Cañizales, et al. (2017) which is used in this work.

With this, we can obtain an estimate for the intrinsic density of LBGs per unit area. A simple ratio of our 1821 studied sources over the effective area covered by ALMA gives a value of, approximately, 230 LBGs per arcmin^2 (either as upper limits or as detections). To establish a reference with other ALMA observations, B16 studied 330 LBGs over a 1 arcmin^2 region of HUDF. And F17 examined 67 star-forming galaxies in an area of $39'' \times 39''$, which corresponds to a density of $\approx$160 sources per arcmin^2.

6

Conclusions

In this work, we utilized ALMA 1.1mm mosaic images from five out of six Frontier Fields clusters with rms values between 55μJy and 71μJy to place constraints the IR excesses of 1821 UV-selected LBGs as functions of their UV-slopes, stellar masses, star formation rates, and photometric redshifts. After correcting for magnification, we effectively probe LBG candidates with rest-frame UV magnitudes ranging from ~33 to ~23 ABmag.

Noise levels in the ALMA maps, as well as the intrinsic fluxes from each LBG candidate, did not allow to treat them all as proper detections. We set a detection threshold of 4.1$-\sigma$. More than 99% of our sample had to be considered as upper limits and the rest, three LBG candidates, were considered as proper detections. These three detections are all located in one cluster (AS1063).

Comparing our 1818 IRX 2-σ upper limits with previous IRX relations (IRX-β and IRX-$M_\star$), we find that the vast majority of our limits lie above locals and *Consensus* relations, with only 10 LBGs constrained to lie below the M99 IRX-β relation and only one below the M18 IRX-$M_\star$.

To increase the probabilities of obtaining useful results, we divided candidates into bins of stellar mass, UV-slope and photometric redshift, in order to perform stacking of their observations with ALMA using `stacker` software. Stacking allowed us to reach better sensitivities without using longer observation times.

`uv`-stacking was implemented with a weighted median to avoid extreme influence from outliers. Two weight schemes were devised; one combining the primary beam corrections and the magnification factors, and the other combining primary-beam-corrected rms errors and magnification-corrected UV fluxes. In this way, we explored, separately, the properties

from the galaxy clusters and the LBG candidates themselves. With these configurations, we stacked the ALMA observations and computed the stacked IRX values. We caution that our choice of weights can skew the stacking results to the more massive sources.

Despite all combinations of UV-slopes, stellar masses, photometric redshifts, and weights, the uv-stacking of ALMA upper limits failed to deliver any SNRs which could be considered as a detection.

The vast majority of our stacked IRX values lie above all local IRX-β and IRX-$M_\star$ relations, although we have a few bins constrained to lie below the M99 IRX-β and *Consensus* relations. Apart from these results, which create mild tension with previous relations, IRX stacking constraints are not in contradiction with previous results, given the likely scatter.

We also investigated the correlation between β and stellar mass for our candidates. Despite the significant spread and the incompleteness below stellar masses of $\sim 10^{8.5}\,M_\odot$, we observed a clear and smooth trend which extends to lower masses and bluer (lower) β values, which is consistent with expectations from previous works.

From the point of view of stacking, one consideration is related to our strategy of adopting stacking positions centered on the UV position of the LBG, as opposed to the peak pixel within one ALMA beam of the LBG. The former will deliver a less biased result, but could fail to account for potential physical offsets which might be expected since the peak of the unobscured star formation is unlikely to coincide exactly with the peak of the observed star formation.

In order to improve upon our results, we would need to extend considerably the depth and sensitivity of our observations to lower the average rms by at least a factor of several and ideally >1 dex. Since reducing noise levels to this extent is expensive in terms of observation time, one strategy that can be followed is to choose the positions of the most highly magnified LBG candidates and target these with single-pointing observations as opposed to the mosaic observations used for this work. In this way, significantly fewer pointings will be required but for longer times.

REFERENCES

Alavi, A., B. Siana, J. Richard, et al. (Nov. 2016). "The Evolution of the Faint End of the UV Luminosity Function during the Peak Epoch of Star Formation ($1 < z < 3$)". In: ApJ 832, 56, p. 56. DOI: 10.3847/0004-637X/832/1/56. arXiv: 1606.00469.

Álvarez-Márquez, J., D. Burgarella, S. Heinis, et al. (Mar. 2016). "Dust properties of Lyman-break galaxies at $z \sim 3$". In: A&A 587, A122, A122. DOI: 10.1051/0004-6361/201527190. arXiv: 1512.04120.

Anders, P. and U. Fritze-v. Alvensleben (Apr. 2003). "Spectral and photometric evolution of young stellar populations: The impact of gaseous emission at various metallicities". In: A&A 401, pp. 1063–1070. DOI: 10.1051/0004-6361:20030151. eprint: astro-ph/0302146.

Astropy Collaboration, T. P. Robitaille, E. J. Tollerud, et al. (Oct. 2013). "Astropy: A community Python package for astronomy". In: A&A 558, A33, A33. DOI: 10.1051/0004-6361/201322068. arXiv: 1307.6212 [astro-ph.IM].

Barisic, I., A. L. Faisst, P. L. Capak, et al. (Aug. 2017). "Dust Properties of C II Detected $z \sim 5.5$ Galaxies: New HST/WFC3 Near-IR Observations". In: ApJ 845, 41, p. 41. DOI: 10.3847/1538-4357/aa7eda. arXiv: 1707.02980.

Bell, E. F., C. Papovich, C. Wolf, et al. (May 2005). "Toward an Understanding of the Rapid Decline of the Cosmic Star Formation Rate". In: ApJ 625, pp. 23–36. DOI: 10.1086/429552. eprint: astro-ph/0502246.

Benítez, N. (June 2000). "Bayesian Photometric Redshift Estimation". In: ApJ 536, pp. 571–583. DOI: 10.1086/308947. eprint: astro-ph/9811189.

Boquien, M., V. Buat, A. Boselli, et al. (Mar. 2012). "The IRX-β relation on subgalactic scales in star-forming galaxies of the Herschel Reference Survey". In: A&A 539, A145, A145. DOI: 10.1051/0004-6361/201118624. arXiv: 1201.2405.

Bourne, N., J. S. Dunlop, E. Merlin, et al. (May 2017). "Evolution of cosmic star formation in the SCUBA-2 Cosmology Legacy Survey". In: MNRAS 467, pp. 1360–1385. DOI: 10.1093/mnras/stx031. arXiv: 1607.04283.

Bouwens, R. J., M. Aravena, R. Decarli, et al. (Dec. 2016). "ALMA Spectroscopic Survey in the Hubble Ultra Deep Field: The Infrared Excess of UV-Selected z = 2-10 Galaxies as a Function of UV-Continuum Slope and Stellar Mass". In: ApJ 833, 72, p. 72. DOI: 10.3847/1538-4357/833/1/72. arXiv: 1606.05280.

Bouwens, R. J., G. D. Illingworth, M. Franx, et al. (Nov. 2009). "UV Continuum Slope and Dust Obscuration from z ˜ 6 to z ˜ 2: The Star Formation Rate Density at High Redshift". In: ApJ 705, pp. 936–961. DOI: 10.1088/0004-637X/705/1/936. arXiv: 0909.4074.

Bouwens, R. J., G. D. Illingworth, P. A. Oesch, M. Franx, et al. (Aug. 2012). "UV-continuum Slopes at z ˜ 4-7 from the HUDF09+ERS+CANDELS Observations: Discovery of a Well-defined UV Color-Magnitude Relationship for z >= 4 Star-forming Galaxies". In: ApJ 754, 83, p. 83. DOI: 10.1088/0004-637X/754/2/83. arXiv: 1109.0994.

Bouwens, R. J., G. D. Illingworth, P. A. Oesch, I. Labbé, M. Trenti, et al. (Aug. 2011). "Ultraviolet Luminosity Functions from 132 z ˜ 7 and z ˜ 8 Lyman-break Galaxies in the Ultra-deep HUDF09 and Wide-area Early Release Science WFC3/IR Observations". In: ApJ 737, 90, p. 90. DOI: 10.1088/0004-637X/737/2/90. arXiv: 1006.4360.

Bouwens, R. J., G. D. Illingworth, P. A. Oesch, I. Labbé, P. G. van Dokkum, et al. (Oct. 2014). "UV-continuum Slopes of >4000 z ˜ 4-8 Galaxies from the HUDF/XDF, HUDF09, ERS, CANDELS-South, and CANDELS-North Fields". In: ApJ 793, 115, p. 115. DOI: 10.1088/0004-637X/793/2/115. arXiv: 1306.2950.

Bouwens, R. J., G. D. Illingworth, P. A. Oesch, M. Trenti, et al. (Apr. 2015). "UV Luminosity Functions at Redshifts z˜4 to z˜10: 10,000 Galaxies from HST Legacy Fields". In: ApJ 803, 34, p. 34. DOI: 10.1088/0004-637X/803/1/34. arXiv: 1403.4295.

Bowler, R. A. A., N. Bourne, J. S. Dunlop, R. J. McLure, and D. J. McLeod (Dec. 2018). "Obscured star formation in bright z ≃ 7 Lyman-break galaxies". In: MNRAS 481, pp. 1631–1644. DOI: 10.1093/mnras/sty2368. arXiv: 1802.05720.

Bowler, R. A. A., R. J. McLure, J. S. Dunlop, et al. (July 2017). "No evidence for Population III stars or a Direct Collapse Black Hole in the z = 6.6 Lyman-α emitter 'CR7'". In: MNRAS 469, pp. 448–458. DOI: 10.1093/mnras/stx839. arXiv: 1609.00727.

Brammer, G. B., P. G. van Dokkum, and P. Coppi (Oct. 2008). "EAZY: A Fast, Public Photometric Redshift Code". In: ApJ 686, 1503-1513, pp. 1503–1513. DOI: 10.1086/591786. arXiv: 0807.1533.

Brandl, B. R., D. Devost, S. J. U. Higdon, et al. (Sept. 2004). "Spitzer Infrared Spectrograph Spectroscopy of the Prototypical Starburst Galaxy NGC 7714". In: ApJS 154, pp. 188–192. DOI: 10.1086/422101. eprint: astro-ph/0406171.

Brown, M. J. I., J. Moustakas, J.-D. T. Smith, et al. (June 2014). "An Atlas of Galaxy Spectral Energy Distributions from the Ultraviolet to the Mid-infrared". In: ApJS 212, 18, p. 18. DOI: 10.1088/0067-0049/212/2/18. arXiv: 1312.3029.

Bruzual, G. and S. Charlot (Oct. 2003). "Stellar population synthesis at the resolution of 2003". In: MNRAS 344, pp. 1000–1028. DOI: 10.1046/j.1365-8711.2003.06897.x. eprint: astro-ph/0309134.

Calzetti, D. (Oct. 2013). "Star Formation Rate Indicators". In: *Secular Evolution of Galaxies*. Ed. by J. Falcón-Barroso and J. H. Knapen, p. 419.

Calzetti, D., L. Armus, R. C. Bohlin, et al. (Apr. 2000). "The Dust Content and Opacity of Actively Star-forming Galaxies". In: ApJ 533, pp. 682–695. DOI: 10.1086/308692. eprint: astro-ph/9911459.

Caminha, G. B., C. Grillo, P. Rosati, et al. (Apr. 2017). "A refined mass distribution of the cluster MACS J0416.1-2403 from a new large set of spectroscopic multiply lensed sources". In: A&A 600, A90, A90. DOI: 10.1051/0004-6361/201629297. arXiv: 1607.03462.

Capak, P. L., C. Carilli, G. Jones, et al. (June 2015). "Galaxies at redshifts 5 to 6 with systematically low dust content and high [C II] emission". In: Nature 522, pp. 455–458. DOI: 10.1038/nature14500. arXiv: 1503.07596.

Casey, C. M. (Oct. 2012). "Far-infrared spectral energy distribution fitting for galaxies near and far". In: MNRAS 425, pp. 3094–3103. DOI: 10.1111/j.1365-2966.2012.21455.x. arXiv: 1206.1595.

Casey, C. M., D. Narayanan, and A. Cooray (Aug. 2014). "Dusty star-forming galaxies at high redshift". In: Phys. Rep. 541, pp. 45–161. DOI: 10.1016/j.physrep.2014.02.009. arXiv: 1402.1456.

Casey, C. M., N. Z. Scoville, D. B. Sanders, et al. (Dec. 2014). "Are Dusty Galaxies Blue? Insights on UV Attenuation from Dust-selected Galaxies". In: ApJ 796, 95, p. 95. DOI: 10.1088/0004-637X/796/2/95. arXiv: 1410.0702.

Castellano, M., A. Fontana, A. Grazian, et al. (Apr. 2012). "The blue UV slopes of z ˜ 4 Lyman break galaxies: implications for the corrected star formation rate density". In: A&A 540, A39, A39. DOI: 10.1051/0004-6361/201118050. arXiv: 1109.1757.

Chabrier, G. (July 2003). "Galactic Stellar and Substellar Initial Mass Function". In: PASP 115, pp. 763–795. DOI: 10.1086/376392. eprint: astro-ph/0304382.

Coe, D., L. Bradley, and A. Zitrin (Feb. 2015). "Frontier Fields: High-redshift Predictions and Early Results". In: ApJ 800, 84, p. 84. DOI: 10.1088/0004-637X/800/2/84. arXiv: 1405.0011.

Coppin, K., M. Halpern, D. Scott, et al. (Mar. 2008). "The SCUBA HAlf Degree Extragalactic Survey - VI. 350-μm mapping of submillimetre galaxies". In: MNRAS 384, pp. 1597–1610. DOI: 10.1111/j.1365-2966.2007.12808.x. arXiv: 0711.0274.

da Cunha, E., B. Groves, F. Walter, et al. (Mar. 2013). "On the Effect of the Cosmic Microwave Background in High-redshift (Sub-)millimeter Observations". In: ApJ 766, 13, p. 13. DOI: 10.1088/0004-637X/766/1/13. arXiv: 1302.0844.

Daddi, E., D. M. Alexander, M. Dickinson, et al. (Nov. 2007). "Multiwavelength Study of Massive Galaxies at z˜2. II. Widespread Compton-thick Active Galactic Nuclei and the Concurrent Growth of Black Holes and Bulges". In: ApJ 670, pp. 173–189. DOI: 10.1086/521820. arXiv: 0705.2832.

Daddi, E., M. Dickinson, G. Morrison, et al. (Nov. 2007). "Multiwavelength Study of Massive Galaxies at z˜2. I. Star Formation and Galaxy Growth". In: ApJ 670, pp. 156–172. DOI: 10.1086/521818. arXiv: 0705.2831.

Dale, D. A., A. Gil de Paz, K. D. Gordon, et al. (Feb. 2007). "An Ultraviolet-to-Radio Broadband Spectral Atlas of Nearby Galaxies". In: ApJ 655, pp. 863–884. DOI: 10.1086/510362. eprint: astro-ph/0610688.

Dunlop, J. S. (2013). "Observing the First Galaxies". In: *The First Galaxies*. Ed. by T. Wiklind, B. Mobasher, and V. Bromm. Vol. 396. Astrophysics and Space Science Library, p. 223. DOI: 10.1007/978-3-642-32362-1_5. arXiv: 1205.1543.

Eldridge, J. J., E. R. Stanway, L. Xiao, et al. (Nov. 2017). "Binary Population and Spectral Synthesis Version 2.1: Construction, Observational Verification, and New Results". In: *PASA* 34, e058, e058. DOI: 10.1017/pasa.2017.51. arXiv: 1710.02154 [astro-ph.SR].

Finkelstein, S. L., C. Papovich, B. Salmon, et al. (Sept. 2012). "Candels: The Evolution of Galaxy Rest-frame Ultraviolet Colors from z = 8 to 4". In: ApJ 756, 164, p. 164. DOI: 10.1088/0004-637X/756/2/164. arXiv: 1110.3785.

Förster Schreiber, N. M., R. Genzel, D. Lutz, and A. Sternberg (Dec. 2003). "The Nature of Starburst Activity in M82". In: ApJ 599, pp. 193–217. DOI: 10.1086/379097. eprint: astro-ph/0309357.

Fudamoto, Y., P. A. Oesch, E. Schinnerer, et al. (Nov. 2017). "The dust attenuation of star-forming galaxies at z˜3 and beyond: New insights from ALMA observations". In: MNRAS 472, pp. 483–490. DOI: 10.1093/mnras/stx1948. arXiv: 1705.01559.

Giavalisco, M. (2002). "Lyman-Break Galaxies". In: ARA&A 40, pp. 579–641. DOI: 10.1146/annurev.astro.40.121301.111837.

González Delgado, R. M., M. L. García-Vargas, J. Goldader, C. Leitherer, and A. Pasquali (Mar. 1999). "Multiwavelength Study of the Starburst Galaxy NGC 7714. I. Ultraviolet-Optical Spectroscopy". In: ApJ 513, pp. 707–719. DOI: 10.1086/306893. eprint: astro-ph/9810331.

González-López, J., F. E. Bauer, M. Aravena, et al. (Dec. 2017). "The ALMA Frontier Fields Survey. III. 1.1 mm emission line identifications in Abell 2744, MACSJ 0416.1-2403, MACSJ 1149.5+2223, Abell 370, and Abell S1063". In: A&A 608, A138, A138. DOI: 10.1051/0004-6361/201730961. arXiv: 1704.03007.

González-López, J., F. E. Bauer, C. Romero-Cañizales, et al. (Jan. 2017). "The ALMA Frontier Fields Survey. I. 1.1 mm continuum detections in Abell 2744, MACS J0416.1-2403 and MACS J1149.5+2223". In: A&A 597, A41, A41. DOI: 10.1051/0004-6361/201628806. arXiv: 1607.03808.

Greco, J. P., P. Martini, and T. A. Thompson (Sept. 2012). "Measurement of the Mass and Stellar Population Distribution in M82 with the LBT". In: ApJ 757, 24, p. 24. DOI: 10.1088/0004-637X/757/1/24. arXiv: 1202.0824 [astro-ph.CO].

Hashimoto, T., N. Laporte, K. Mawatari, et al. (May 2018). "The onset of star formation 250 million years after the Big Bang". In: Nature 557, pp. 392–395. DOI: 10.1038/s41586-018-0117-z. arXiv: 1805.05966.

Heap, S. R. (Aug. 2012). "What can the UV SED tell us about primitive galaxies?" In: *The Spectral Energy Distribution of Galaxies - SED 2011*. Ed. by R. J. Tuffs and C. C. Popescu. Vol. 284. IAU Symposium, pp. 49–52. DOI: 10.1017/S174392131200871X.

Heinis, S., V. Buat, M. Béthermin, et al. (Jan. 2014). "HerMES: dust attenuation and star formation activity in ultraviolet-selected samples from $z\tilde{}4$ to$\tilde{}1.5$". In: MNRAS 437, pp. 1268–1283. DOI: 10.1093/mnras/stt1960. arXiv: 1310.3227.

Hoag, A., M. Bradač, G. Brammer, et al. (Feb. 2018). "HST Grism Observations of a Gravitationally Lensed Redshift 9.5 Galaxy". In: ApJ 854, 39, p. 39. DOI: 10.3847/1538-4357/aaa9c2. arXiv: 1709.03992.

Hunter, J. D. (2007). "Matplotlib: A 2D graphics environment". In: *Computing In Science & Engineering* 9.3, pp. 90–95. DOI: 10.1109/MCSE.2007.55.

Jauzac, M., B. Clément, M. Limousin, et al. (Sept. 2014). "Hubble Frontier Fields: a high-precision strong-lensing analysis of galaxy cluster MACSJ0416.1-2403 using$\tilde{}$200 multiple

images". In: MNRAS 443, pp. 1549–1554. DOI: 10.1093/mnras/stu1355. arXiv: 1405.3582.

Kawamata, R., M. Ishigaki, K. Shimasaku, et al. (Mar. 2018). "Size—Luminosity Relations and UV Luminosity Functions at z=6—9 Simultaneously Derived from the Complete Hubble Frontier Fields Data". In: ApJ 855, 4, p. 4. DOI: 10.3847/1538-4357/aaa6cf. arXiv: 1710.07301.

Kawamata, R., M. Oguri, M. Ishigaki, K. Shimasaku, and M. Ouchi (Mar. 2016). "Precise Strong Lensing Mass Modeling of Four Hubble Frontier Field Clusters and a Sample of Magnified High-redshift Galaxies". In: ApJ 819, 114, p. 114. DOI: 10.3847/0004-637X/819/2/114. arXiv: 1510.06400.

Koprowski, M. P., K. E. K. Coppin, J. E. Geach, et al. (Oct. 2018). "A direct calibration of the IRX-β relation in Lyman-break Galaxies at z = 3-5". In: MNRAS 479, pp. 4355–4366. DOI: 10.1093/mnras/sty1527. arXiv: 1801.00791.

Kovács, A., S. C. Chapman, C. D. Dowell, et al. (Oct. 2006). "SHARC-2 350 μm Observations of Distant Submillimeter-selected Galaxies". In: ApJ 650, pp. 592–603. DOI: 10.1086/506341. eprint: astro-ph/0604591.

Kriek, M., P. G. van Dokkum, I. Labbé, et al. (July 2009). "An Ultra-Deep Near-Infrared Spectrum of a Compact Quiescent Galaxy at z = 2.2". In: ApJ 700, pp. 221–231. DOI: 10.1088/0004-637X/700/1/221. arXiv: 0905.1692 [astro-ph.CO].

Lagattuta, D. J., J. Richard, B. Clément, et al. (Aug. 2017). "Lens modelling Abell 370: crowning the final frontier field with MUSE". In: MNRAS 469, pp. 3946–3964. DOI: 10.1093/mnras/stx1079. arXiv: 1611.01513.

Laporte, N., R. S. Ellis, F. Boone, et al. (Mar. 2017). "Dust in the Reionization Era: ALMA Observations of a z = 8.38 Gravitationally Lensed Galaxy". In: ApJ 837, L21, p. L21. DOI: 10.3847/2041-8213/aa62aa. arXiv: 1703.02039.

Le Floc'h, E., C. Papovich, H. Dole, et al. (Oct. 2005). "Infrared Luminosity Functions from the Chandra Deep Field-South: The Spitzer View on the History of Dusty Star Formation

at 0 <˜ z <˜ 1". In: ApJ 632, pp. 169–190. DOI: 10.1086/432789. eprint: astro-ph/0506462.

Lindroos, L., K. K. Knudsen, W. Vlemmings, J. Conway, and I. Martí-Vidal (Feb. 2015). "Stacking of large interferometric data sets in the image- and uv-domain - a comparative study". In: MNRAS 446, pp. 3502–3515. DOI: 10.1093/mnras/stu2344. arXiv: 1411.1410.

Lotz, J. M., A. Koekemoer, D. Coe, et al. (Mar. 2017). "The Frontier Fields: Survey Design and Initial Results". In: ApJ 837, 97, p. 97. DOI: 10.3847/1538-4357/837/1/97. arXiv: 1605.06567.

Madau, P. and M. Dickinson (Aug. 2014). "Cosmic Star-Formation History". In: ARA&A 52, pp. 415–486. DOI: 10.1146/annurev-astro-081811-125615. arXiv: 1403.0007.

Magnelli, B., P. Popesso, S. Berta, et al. (May 2013). "The deepest Herschel-PACS far-infrared survey: number counts and infrared luminosity functions from combined PEP/GOODS-H observations". In: A&A 553, A132, A132. DOI: 10.1051/0004-6361/201321371. arXiv: 1303.4436.

Mahler, G., J. Richard, B. Clément, et al. (Jan. 2018). "Strong-lensing analysis of A2744 with MUSE and Hubble Frontier Fields images". In: MNRAS 473, pp. 663–692. DOI: 10.1093/mnras/stx1971. arXiv: 1702.06962.

McLeod, D. J., R. J. McLure, and J. S. Dunlop (July 2016). "The z = 9-10 galaxy population in the Hubble Frontier Fields and CLASH surveys: the z = 9 luminosity function and further evidence for a smooth decline in ultraviolet luminosity density at z≥ 8". In: MNRAS 459, pp. 3812–3824. DOI: 10.1093/mnras/stw904. arXiv: 1602.05199.

McLure, R. J., J. S. Dunlop, F. Cullen, et al. (May 2018). "Dust attenuation in 2 < z < 3 star-forming galaxies from deep ALMA observations of the Hubble Ultra Deep Field". In: MNRAS 476, pp. 3991–4006. DOI: 10.1093/mnras/sty522. arXiv: 1709.06102.

McMullin, J. P., B. Waters, D. Schiebel, W. Young, and K. Golap (Oct. 2007). "CASA Architecture and Applications". In: *Astronomical Data Analysis Software and Systems XVI*. Ed. by R. A. Shaw, F. Hill, and D. J. Bell. Vol. 376. Astronomical Society of the Pacific Conference Series, p. 127.

Merten, J., D. Coe, R. Dupke, et al. (Oct. 2011). "Creation of cosmic structure in the complex galaxy cluster merger Abell 2744". In: MNRAS 417, pp. 333–347. DOI: 10.1111/j.1365-2966.2011.19266.x. arXiv: 1103.2772 [astro-ph.CO].

Meurer, G. R., T. M. Heckman, and D. Calzetti (Aug. 1999). "Dust Absorption and the Ultraviolet Luminosity Density at z ˜ 3 as Calibrated by Local Starburst Galaxies". In: ApJ 521, pp. 64–80. DOI: 10.1086/307523. eprint: astro-ph/9903054.

Muñoz Arancibia, A. M., J. González-López, E. Ibar, et al. (Dec. 2017). "The ALMA Frontier Fields Survey - IV. Lensing-corrected 1.1 mm number counts in Abell 2744, MACSJ0416.1-2403 and MACSJ1149.5+2223". In: *ArXiv e-prints*. arXiv: 1712.03983.

Narayanan, D., R. Davé, B. D. Johnson, et al. (Feb. 2018). "The IRX-β dust attenuation relation in cosmological galaxy formation simulations". In: MNRAS 474, pp. 1718–1736. DOI: 10.1093/mnras/stx2860. arXiv: 1705.05858.

Oesch, P. A., R. J. Bouwens, G. D. Illingworth, I. Labbé, and M. Stefanon (Mar. 2018). "The Dearth of z ∼ 10 Galaxies in All HST Legacy Fields—The Rapid Evolution of the Galaxy Population in the First 500 Myr". In: ApJ 855, 105, p. 105. DOI: 10.3847/1538-4357/aab03f. arXiv: 1710.11131.

Oke, J. B. and J. E. Gunn (Mar. 1983). "Secondary standard stars for absolute spectrophotometry". In: ApJ 266, pp. 713–717. DOI: 10.1086/160817.

Oliver, S. J., J. Bock, B. Altieri, et al. (Aug. 2012). "The Herschel Multi-tiered Extragalactic Survey: HerMES". In: MNRAS 424, pp. 1614–1635. DOI: 10.1111/j.1365-2966.2012.20912.x. arXiv: 1203.2562.

Pannella, M., C. L. Carilli, E. Daddi, et al. (June 2009). "Star Formation and Dust Obscuration at z ≈ 2: Galaxies at the Dawn of Downsizing". In: ApJ 698, pp. L116–L120. DOI: 10.1088/0004-637X/698/2/L116. arXiv: 0905.1674 [astro-ph.CO].

Pelló, R. (Dec. 2016). "High-z galaxies & Reionization". In: *SF2A-2016: Proceedings of the Annual meeting of the French Society of Astronomy and Astrophysics*. Ed. by C. Reylé, J. Richard, L. Cambrésy, et al., pp. 417–422.

Pettini, M., M. Kellogg, C. C. Steidel, et al. (Dec. 1998). "Infrared Observations of Nebular Emission Lines from Galaxies at Z ˜= 3". In: ApJ 508, pp. 539–550. DOI: 10.1086/306431. eprint: astro-ph/9806219.

Pettini, M., A. E. Shapley, C. C. Steidel, et al. (June 2001). "The Rest-Frame Optical Spectra of Lyman Break Galaxies: Star Formation, Extinction, Abundances, and Kinematics". In: ApJ 554, pp. 981–1000. DOI: 10.1086/321403. eprint: astro-ph/0102456.

Prevot, M. L., J. Lequeux, E. Maurice, L. Prevot, and B. Rocca-Volmerange (Mar. 1984). "The typical interstellar extinction in the Small Magellanic Cloud". In: A&A 132, pp. 389–392.

Reddy, N. A., D. K. Erb, M. Pettini, C. C. Steidel, and A. E. Shapley (Apr. 2010). "Dust Obscuration and Metallicity at High Redshift: New Inferences from UV, Hα, and 8 μm Observations of z ˜ 2 Star-forming Galaxies". In: ApJ 712, pp. 1070–1091. DOI: 10.1088/0004-637X/712/2/1070. arXiv: 1002.0837.

Reddy, N. A., P. A. Oesch, R. J. Bouwens, et al. (Jan. 2018). "The HDUV Survey: A Revised Assessment of the Relationship between UV Slope and Dust Attenuation for High-redshift Galaxies". In: ApJ 853, 56, p. 56. DOI: 10.3847/1538-4357/aaa3e7. arXiv: 1705.09302.

Reddy, N. A., C. C. Steidel, D. Fadda, et al. (June 2006). "Star Formation and Extinction in Redshift z˜2 Galaxies: Inferences from Spitzer MIPS Observations". In: ApJ 644, pp. 792–812. DOI: 10.1086/503739. eprint: astro-ph/0602596.

Reddy, N. A., C. C. Steidel, M. Pettini, et al. (Mar. 2008). "Multiwavelength Constraints on the Cosmic Star Formation History from Spectroscopy: The Rest-Frame Ultraviolet, Hα, and Infrared Luminosity Functions at Redshifts 1.9 lesssim z lesssim 3.4". In: ApJS 175, pp. 48–85. DOI: 10.1086/521105. arXiv: 0706.4091.

Richard, J., M. Jauzac, M. Limousin, et al. (Oct. 2014). "Mass and magnification maps for the Hubble Space Telescope Frontier Fields clusters: implications for high-redshift studies". In: MNRAS 444, pp. 268–289. DOI: 10.1093/mnras/stu1395. arXiv: 1405.3303.

Robitaille, T. and E. Bressert (Aug. 2012). *APLpy: Astronomical Plotting Library in Python*. Astrophysics Source Code Library. ascl: 1208.017.

Rogers, A. B., R. J. McLure, and J. S. Dunlop (Mar. 2013). "The unbiased measurement of ultraviolet spectral slopes in low-luminosity galaxies at z ≈ 7". In: MNRAS 429, pp. 2456–2468. DOI: 10.1093/mnras/sts515. arXiv: 1209.4636.

Salim, S. and M. Boquien (Dec. 2018). "Diversity of Galaxy Dust Attenuation Curves Drives the Scatter in the IRX-beta Relation". In: *arXiv e-prints*. arXiv: 1812.05606.

Santini, P., A. Fontana, M. Castellano, et al. (Sept. 2017). "The Star Formation Main Sequence in the Hubble Space Telescope Frontier Fields". In: ApJ 847, 76, p. 76. DOI: 10.3847/1538-4357/aa8874. arXiv: 1706.07059.

Schaerer, D. and S. de Barros (Aug. 2009). "The impact of nebular emission on the ages of z≈ 6 galaxies". In: A&A 502, pp. 423–426. DOI: 10.1051/0004-6361/200911781. arXiv: 0905.0866.

Schaerer, D., S. de Barros, and P. Sklias (Jan. 2013). "Properties of z ∼ 3-6 Lyman break galaxies. I. Testing star formation histories and the SFR-mass relation with ALMA and near-IR spectroscopy". In: A&A 549, A4, A4. DOI: 10.1051/0004-6361/201220002. arXiv: 1207.3074.

Schneider, P. (2006). *Extragalactic Astronomy and Cosmology*. Springer. ISBN: 9783540331742.

Shapley, A. E., C. C. Steidel, M. Pettini, and K. L. Adelberger (May 2003). "Rest-Frame Ultraviolet Spectra of z˜3 Lyman Break Galaxies". In: ApJ 588, pp. 65–89. DOI: 10.1086/373922. eprint: astro-ph/0301230.

Smit, R., R. J. Bouwens, I. Labbé, et al. (Dec. 2016). "Inferred H#9082 Flux as a Star Formation Rate Indicator at z ˜ 4-5: Implications for Dust Properties, Burstiness, and the z = 4-8 Star Formation Rate Functions". In: ApJ 833, 254, p. 254. DOI: 10.3847/1538-4357/833/2/254. arXiv: 1511.08808.

Smith, G. P., H. Ebeling, M. Limousin, et al. (Dec. 2009). "Hubble Space Telescope Observations of a Spectacular New Strong-Lensing Galaxy Cluster: MACS J1149.5+2223 at z = 0.544". In: ApJ 707, pp. L163–L168. DOI: 10.1088/0004-637X/707/2/L163. arXiv: 0911.2003.

Stark, D. P. (Sept. 2016). "Galaxies in the First Billion Years After the Big Bang". In: ARA&A 54, pp. 761–803. DOI: 10.1146/annurev-astro-081915-023417.

Stark, D. P., M. A. Schenker, R. Ellis, et al. (Feb. 2013). "Keck Spectroscopy of 3 < z < 7 Faint Lyman Break Galaxies: The Importance of Nebular Emission in Understanding the Specific Star Formation Rate and Stellar Mass Density". In: ApJ 763, 129, p. 129. DOI: 10.1088/0004-637X/763/2/129. arXiv: 1208.3529.

Steidel, C. C., K. L. Adelberger, M. Giavalisco, M. Dickinson, and M. Pettini (July 1999). "Lyman-Break Galaxies at z>˜4 and the Evolution of the Ultraviolet Luminosity Density at High Redshift". In: ApJ 519, pp. 1–17. DOI: 10.1086/307363. eprint: astro-ph/9811399.

Steidel, C. C., M. Giavalisco, M. Dickinson, and K. L. Adelberger (Aug. 1996). "Spectroscopy of Lyman Break Galaxies in the Hubble Deep Field". In: AJ 112, p. 352. DOI: 10.1086/118019. eprint: astro-ph/9604140.

Steidel, C. C., M. Giavalisco, M. Pettini, M. Dickinson, and K. L. Adelberger (May 1996). "Spectroscopic Confirmation of a Population of Normal Star-forming Galaxies at Redshifts Z > 3". In: ApJ 462, p. L17. DOI: 10.1086/310029. eprint: astro-ph/9602024.

Takeuchi, T. T., F.-T. Yuan, A. Ikeyama, K. L. Murata, and A. K. Inoue (Aug. 2012). "Reexamination of the Infrared Excess-Ultraviolet Slope Relation of Local Galaxies". In: ApJ 755, 144, p. 144. DOI: 10.1088/0004-637X/755/2/144. arXiv: 1206.3905.

Thompson, A. R., J. M. Moran, and G. W. Swenson Jr. (2017). *Interferometry and Synthesis in Radio Astronomy, 3rd Edition*. Astronomy and Astrophysics Library. Springer International Publishing. DOI: 10.1007/978-3-319-44431-4.

Wilson, T. L., K. Rohlfs, and S. Hüttemeister (2013). *Tools of Radio Astronomy*. Astronomy and Astrophysics Library. Springer Berlin Heidelberg. DOI: 10.1007/978-3-642-39950-3.

Wood, C. M., C. A. Tremonti, D. Calzetti, et al. (Sept. 2015). "Supernova-driven outflows in NGC 7552: a comparison of H α and UV tracers". In: MNRAS 452, pp. 2712–2730. DOI: 10.1093/mnras/stv1471. arXiv: 1507.00346.

Wright, E. L. (Dec. 2006). "A Cosmology Calculator for the World Wide Web". In: PASP 118, pp. 1711–1715. DOI: 10.1086/510102. eprint: astro-ph/0609593.

Zitrin, A., T. Broadhurst, R. Barkana, Y. Rephaeli, and N. Benítez (Jan. 2011). "Strong-lensing analysis of a complete sample of 12 MACS clusters at z > 0.5: mass models and Einstein radii". In: MNRAS 410, pp. 1939–1956. DOI: 10.1111/j.1365-2966.2010.17574.x. arXiv: 1002.0521 [astro-ph.CO].

Zitrin, A., M. Meneghetti, K. Umetsu, et al. (Jan. 2013). "CLASH: The Enhanced Lensing Efficiency of the Highly Elongated Merging Cluster MACS J0416.1-2403". In: ApJ 762, L30, p. L30. DOI: 10.1088/2041-8205/762/2/L30. arXiv: 1211.2797 [astro-ph.CO].

Appendices

A

Stacking Results

Here are included the results for the stacking process in two different configuration of the LBG candidates.

Each configuration shows four results as different stacking weights and CLEANing methods were used.

A.1 UV slope binning

Candidates were divided into five UV-slope (β) bins as described in §3. Targets with stellar masses below 10^6 $M_\odot$ were not included to avoid low brightness elements and to keep consistency with stellar mass stacking.Each configuration shows four results as different stacking weights and *CLEAN*ing methods were used (see §3).

Values obtained after stacking each different configuration are shown in Table A.1.

A.2 Stellar mass binning

The values obtained after stacking each different configuration are shown in Tables A.2 and A.3.

In Table A.4, we also report the results for the stacking with the low-mass candidates.

Table A.1: uv-stacking results for different beta and photometric redshift bins for our sample.

UV-slope	z_{ph}	Sources #[a]	Weight[b]	CLEAN[c]	Flux[d,e] [μJy]	SNR[f]
$-4.0 \leq \beta < -3.0$	$z < 4.0$	40	μ	Natural	1 ± 18	0.06
				Taper	-40 ± 26	-1.54
			F_{UV}	Natural	84 ± 53	1.58
				Taper	61 ± 90	0.68
	$4.0 \leq z < 7.0$	30	μ	Natural	27 ± 21	1.29
				Taper	63 ± 28	2.25
			F_{UV}	Natural	114 ± 53	2.15
				Taper	105 ± 62	1.69
	$7.0 \leq z$	12	μ	Natural	18 ± 26	0.69
				Taper	16 ± 37	0.43
			F_{UV}	Natural	5 ± 24	0.21
				Taper	10 ± 32	0.31
$-3.0 \leq \beta < -2.0$	$z < 4.0$	708	μ	Natural	0 ± 5	0.00
				Taper	-4 ± 8	-0.50
			F_{UV}	Natural	-22 ± 25	-0.88
				Taper	-42 ± 32	-1.31
	$4.0 \leq z < 7.0$	215	μ	Natural	7 ± 8	0.88
				Taper	-3 ± 10	-0.30
			F_{UV}	Natural	3 ± 14	0.21
				Taper	-6 ± 19	-0.32

Table A.1 continued.

UV-slope	z_{ph}	Sources #[a]	Weight[b]	CLEAN[c]	Flux[d,e] [μJy]	SNR[f]
$-2.0 \leq \beta < -1.0$	$7.0 \leq z$	11	μ	Natural	76 ± 32	2.38
				Taper	30 ± 43	0.70
			F_{UV}	Natural	64 ± 29	2.21
				Taper	20 ± 37	0.54
	$z < 4.0$	464	μ	Natural	10 ± 6	1.67
				Taper	12 ± 10	1.20
			F_{UV}	Natural	28 ± 59	0.47
				Taper	7 ± 76	0.09
	$4.0 \leq z < 7.0$	250	μ	Natural	6 ± 7	0.86
				Taper	−3 ± 10	−0.30
			F_{UV}	Natural	7 ± 10	0.70
				Taper	−1 ± 14	−0.07
	$7.0 \leq z$	13	μ	Natural	123 ± 35	3.51
				Taper	124 ± 56	2.21
			F_{UV}	Natural	30 ± 59	0.51
				Taper	11 ± 70	0.16
$-1.0 \leq \beta < 0.0$	$z < 4.0$	8	μ	Natural	17 ± 23	0.74
				Taper	12 ± 34	0.35
			F_{UV}	Natural	12 ± 44	0.27
				Taper	29 ± 58	0.50

Table A.1 continued.

UV-slope	z_{ph}	Sources #[a]	Weight[b]	CLEAN[c]	Flux[d,e] [μJy]	SNR[f]
$0.0 \leq \beta < 1.5$	$4.0 \leq z < 7.0$	50	μ	Natural	11 ± 17	0.65
				Taper	1 ± 22	0.05
			F_{UV}	Natural	20 ± 21	0.95
				Taper	20 ± 28	0.71
	$7.0 \leq z$	6	μ	Natural	51 ± 43	1.19
				Taper	75 ± 57	1.32
			F_{UV}	Natural	12 ± 64	0.19
				Taper	9 ± 105	0.09
	$z < 4.0$	0	μ	Natural	...	...
				Taper	...	...
			F_{UV}	Natural	...	...
				Taper	...	...
	$4.0 \leq z < 7.0$	10	μ	Natural	26 ± 30	0.87
				Taper	-11 ± 48	-0.23
			F_{UV}	Natural	38 ± 40	0.95
				Taper	-14 ± 61	-0.23
	$7.0 \leq z$	1	μ	Natural	57 ± 71	0.80
				Taper	93 ± 125	0.74
			F_{UV}	Natural	57 ± 71	0.80
				Taper	93 ± 125	0.74

[a] Where sources # is zero (0), no stacking was performed.

[b] Weight associated to each candidate, as explained in §3.3. [c] Method used in `CASA` to obtain final image. [d] Maximum value from a $0\farcs5 \times 0\farcs5$ box in the stacked images. Rounded values.

[e] *rms* errors from Eq. 2.9. Rounded values. [f] SNR = $\text{Flux}_{\text{peak}}$ / *rms*

Table A.2: uv-stacking results for different stellar mass and photometric redshift bins for our sample.

Stellar Mass[a]	z_{ph}	Sources #	Weight[b]	CLEAN[c]	Flux[d,e] [μJy]	SNR[f]
$6.0 \leq \log(M_\star/M_\odot) < 6.5$	$z < 4.0$	50	μ	Natural	1 ± 15	0.07
				Taper	-38 ± 20	-1.90
			F_{UV}	Natural	-21 ± 29	-0.72
				Taper	-57 ± 35	-1.63
	$4.0 \leq z < 7.0$	58	μ	Natural	21 ± 12	1.75
				Taper	26 ± 16	1.62
			F_{UV}	Natural	31 ± 15	2.07
				Taper	26 ± 21	1.24
	$7.0 \leq z$	11	μ	Natural	18 ± 23	0.78
				Taper	5 ± 34	0.15
			F_{UV}	Natural	5 ± 20	0.25
				Taper	2 ± 28	0.07
$6.5 \leq \log(M_\star/M_\odot) < 7.0$	$z < 4.0$	117	μ	Natural	2 ± 10	0.20
				Taper	-4 ± 14	-0.29
			F_{UV}	Natural	13 ± 42	0.31
				Taper	-23 ± 60	-0.38
	$4.0 \leq z < 7.0$	84	μ	Natural	14 ± 11	1.27
				Taper	18 ± 15	1.20
			F_{UV}	Natural	25 ± 19	1.32
				Taper	13 ± 25	0.52

Table A.2 continued.

Stellar Mass[a]	z_{ph}	Sources #	Weight[b]	CLEAN[c]	Flux[d,e] [μJy]	SNR[f]
$7.0 \leq \log(M_\star/M_\odot) < 7.5$	$7.0 \leq z$	8	μ	Natural	154 ± 47	3.28
				Taper	135 ± 64	2.11
			F_{UV}	Natural	230 ± 66	3.48
				Taper	181 ± 86	2.10
	$z < 4.0$	224	μ	Natural	18 ± 8	2.25
				Taper	21 ± 12	1.75
			F_{UV}	Natural	15 ± 8	1.88
				Taper	16 ± 11	1.45
	$4.0 \leq z < 7.0$	114	μ	Natural	11 ± 10	1.10
				Taper	−5 ± 14	−0.36
			F_{UV}	Natural	−4 ± 15	−0.27
				Taper	−7 ± 20	−0.35
$7.5 \leq \log(M_\star/M_\odot) < 8.0$	$7.0 \leq z$	3	μ	Natural	66 ± 64	1.03
				Taper	32 ± 86	0.37
			F_{UV}	Natural	58 ± 59	0.98
				Taper	25 ± 83	0.30
	$z < 4.0$	268	μ	Natural	5 ± 7	0.71
				Taper	6 ± 11	0.55
			F_{UV}	Natural	26 ± 42	0.62
				Taper	13 ± 66	0.20

Table A.2 continued.

Stellar Mass[a]	z_{ph}	Sources #	Weight[b]	CLEAN[c]	Flux[d,e] [μJy]	SNR[f]
	$4.0 \leq z < 7.0$	99	μ	Natural	7 ± 11	0.64
				Taper	-7 ± 16	-0.44
			F_{UV}	Natural	6 ± 19	0.32
				Taper	3 ± 26	0.12
	$7.0 \leq z$	4	μ	Natural	105 ± 47	2.23
				Taper	23 ± 69	0.33
			F_{UV}	Natural	78 ± 51	1.53
				Taper	38 ± 58	0.66

[a] Stacked images involved mid-mass candidates ($6.0 \leq \log(M_\star/M_\odot) \leq 8.0$).

[b] Weight associated to each candidate, as explained in §3.3. [c] Method used in `CASA` to obtain final image.

[d] Maximum value from a $0\farcs5 \times 0\farcs5$ box in the stacked images. Rounded values.

[e] *rms* errors from Eq. 2.9. Rounded values. [f] SNR = $\text{Flux}_{\text{peak}}$ / *rms*

Table A.3: uv-stacking results for different stellar mass and photometric redshift bins for our sample.

Stellar Mass[a]	z_{ph}	Sources #	Weight[b]	CLEAN[c]	Flux[d,e] [μJy]	SNR[f]
$8.0 \leq \log(M_\star/M_\odot) < 8.5$	$z < 4.0$	291	μ	Natural	4 ± 7	0.57
				Taper	-1 ± 11	-0.09
			F_{UV}	Natural	12 ± 13	0.92
				Taper	-11 ± 18	-0.61
	$4.0 \leq z < 7.0$	79	μ	Natural	7 ± 12	0.58
				Taper	-3 ± 16	-0.19
			F_{UV}	Natural	20 ± 18	1.11
				Taper	4 ± 24	0.17
	$7.0 \leq z$	2	μ	Natural	131 ± 83	1.58
				Taper	23 ± 149	0.15
			F_{UV}	Natural	131 ± 83	1.58
				Taper	23 ± 149	0.15
$8.5 \leq \log(M_\star/M_\odot) < 9.0$	$z < 4.0$	172	μ	Natural	11 ± 10	1.10
				Taper	13 ± 15	0.87
			F_{UV}	Natural	73 ± 27	2.70
				Taper	58 ± 36	1.61
	$4.0 \leq z < 7.0$	72	μ	Natural	10 ± 16	0.62
				Taper	9 ± 22	0.41
			F_{UV}	Natural	8 ± 67	0.12
				Taper	-93 ± 89	-1.04

Table A.3 continued.

Stellar Mass[a]	z_{ph}	Sources #	Weight[b]	CLEAN[c]	Flux[d,e] [μJy]	SNR[f]
$9.0 \leq \log(M_\star/M_\odot) < 9.5$	$7.0 \leq z$	8	μ	Natural	110 ± 38	2.89
				Taper	159 ± 55	2.89
			F_{UV}	Natural	30 ± 59	0.51
				Taper	11 ± 70	0.16
	$z < 4.0$	72	μ	Natural	31 ± 14	2.21
				Taper	42 ± 20	2.10
			F_{UV}	Natural	17 ± 15	1.13
				Taper	5 ± 20	0.25
	$4.0 \leq z < 7.0$	35	μ	Natural	28 ± 30	0.93
				Taper	−54 ± 40	−1.35
			F_{UV}	Natural	4 ± 36	0.11
				Taper	−16 ± 48	−0.33
	$7.0 \leq z$	5	μ	Natural	−9 ± 35	−0.26
				Taper	12 ± 51	0.24
			F_{UV}	Natural	−33 ± 34	−0.97
				Taper	−24 ± 48	−0.50
$9.5 \leq \log(M_\star/M_\odot) < 10.0$	$z < 4.0$	16	μ	Natural	59 ± 20	2.95
				Taper	63 ± 28	2.25
			F_{UV}	Natural	63 ± 28	2.25
				Taper	63 ± 36	1.75

Table A.3 continued.

Stellar Mass[a]	z_{ph}	Sources #	Weight[b]	CLEAN[c]	Flux[d,e] [μJy]	SNR[f]
$\log(M_\star/M_\odot) \geq 10.0$	$4.0 \leq z < 7.0$	8	μ	Natural	38 ± 46	0.83
				Taper	38 ± 74	0.51
			F_{UV}	Natural	94 ± 36	2.61
				Taper	70 ± 53	1.32
	$7.0 \leq z$	1	μ	Natural	71 ± 68	1.04
				Taper	-23 ± 117	-0.20
			F_{UV}	Natural	71 ± 68	1.04
				Taper	-23 ± 117	-0.20
	$z < 4.0$	2	μ	Natural	147 ± 92	1.60
				Taper	215 ± 114	1.89
			F_{UV}	Natural	147 ± 92	1.60
				Taper	215 ± 114	1.89
	$4.0 \leq z < 7.0$	1	μ	Natural	-104 ± 74	-1.41
				Taper	-131 ± 88	-1.49
			F_{UV}	Natural	-104 ± 74	-1.41
				Taper	-131 ± 88	-1.49
	$7.0 \leq z$	1	μ	Natural	17 ± 68	0.25
				Taper	14 ± 118	0.12
			F_{UV}	Natural	17 ± 68	0.25
				Taper	14 ± 118	0.12

[a] Stacked images involved high-mass candidates ($\log(M_\star/M_\odot) \geq 8.0$). [b] Weight associated to each candidate, as explained in §3.3. [c] Method used in `CASA` to obtain final image. [d] Maximum value from a $0\farcs5 \times 0\farcs5$ box in the stacked images. Rounded values. [e] *rms* errors from Eq. 2.9. Rounded values. [f] SNR = $\text{Flux}_{\text{peak}}$ / *rms*

Table A.4: Properties of low stellar mass ($\log(M_\star/M_\odot) \leq 6.0$) stacked LBG candidates

z_{ph}	Sources #[a]	Weight[b]	CLEAN[c]	Flux[d,e] [μJy]	SNR[f]
$z < 4.0$	8	μ	Natural	7 ± 27	0.26
			Taper	-19 ± 34	-0.56
		F_{UV}	Natural	-21 ± 28	-0.75
			Taper	-43 ± 35	-1.23
$4.0 \leq z < 7.0$	5	μ	Natural	29 ± 37	0.78
			Taper	-34 ± 57	-0.60
		F_{UV}	Natural	24 ± 43	0.56
			Taper	-74 ± 66	-1.12
$7.0 \leq z$	0	μ	Natural	...	...
			Taper	...	...
		F_{UV}	Natural	...	...
			Taper	...	...

[a] Where sources # is zero (0), no stacking was performed.

[b] Weight associated to each candidate, as explained in §3.3.

[c] Method used in `CASA` to obtain final image.

[d] Maximum value from a $0\farcs5 \times 0\farcs5$ box in the stacked images.

[e] *rms* errors from Eq. 2.9. [f] SNR = $\text{Flux}_{\text{peak}}$ / *rms*.

B

Individual Properties

The individual properties of the first 10 of 1821 selected LBG candidates are presented in Tables B.1, B.2, B.3, B.4 and B.5. Properties for the remaining targets are available online.

Table B.1: HST photometry for first 10 selected LBG candidates. Full table available online

ID	R.A [J2000]	Dec [J2000]	z_{ph}	F_{F275W}	F_{F336W}	F_{F435W}	F_{F606W}	F_{F814W}	F_{F105W}	F_{F125W}	F_{F140W}	F_{F160W}
	[hh:mm:ss.ss]	[± dd:mm:ss.ss]		[uJy]	[uJy]	[uJy]	[uJy]	[uJy]	[uJy]	[uJy]	[uJy]	[uJy]
0001	00:14:23.61	-30:24:53.28	2.39	0.2 ± 11.8	22.2 ± 7.2	30.6 ± 2.6	48.4 ± 3.0	43.2 ± 2.0	43.5 ± 3.4	66.4 ± 4.9	75.9 ± 4.8	92.0 ± 4.7
0002	00:14:24.58	-30:24:48.97	2.30	3.0 ± 12.8	33.9 ± 7.8	54.8 ± 3.3	56.0 ± 3.6	47.9 ± 2.3	39.5 ± 3.1	59.3 ± 4.8	56.0 ± 4.7	72.5 ± 4.6
0004	00:14:22.41	-30:24:47.81	2.32	14.4 ± 9.3	36.7 ± 5.5	61.4 ± 1.9	61.0 ± 2.3	51.5 ± 1.5	40.7 ± 2.4	46.0 ± 3.7	36.3 ± 3.6	52.5 ± 3.7
0005	00:14:23.99	-30:24:34.50	2.21	18.8 ± 13.2	64.3 ± 7.8	130.5 ± 3.1	154.8 ± 3.4	161.0 ± 2.3	241.9 ± 3.0	314.9 ± 4.5	367.9 ± 4.5	393.1 ± 4.4
0007	00:14:23.04	-30:24:24.85	2.18	−3.0 ± 7.5	19.0 ± 4.3	21.5 ± 2.3	27.7 ± 2.6	23.5 ± 1.7	21.7 ± 1.8	26.7 ± 2.8	43.0 ± 2.7	31.4 ± 2.6
0008	00:14:22.67	-30:24:23.45	1.89	−2.9 ± 11.3	10.9 ± 7.0	30.3 ± 3.3	24.7 ± 3.9	13.8 ± 2.7	17.3 ± 2.4	21.6 ± 3.5	14.2 ± 3.5	12.2 ± 3.4
0012	00:14:19.11	-30:24:51.09	1.52	40.8 ± 23.7	113.1 ± 14.3	150.1 ± 4.4	157.5 ± 5.3	191.1 ± 3.6	369.6 ± 4.6	450.1 ± 7.4	466.6 ± 6.6	509.7 ± 6.5
0013	00:14:18.87	-30:24:50.40	2.35	−20.5 ± 10.6	12.6 ± 6.2	32.6 ± 1.9	30.8 ± 2.2	23.0 ± 1.5	20.1 ± 2.7	15.2 ± 4.5	18.9 ± 4.2	13.9 ± 4.2
0014	00:14:21.97	-30:24:49.38	2.31	−11.8 ± 16.5	67.8 ± 10.0	105.2 ± 3.4	127.8 ± 4.1	118.0 ± 2.7	123.8 ± 3.4	172.7 ± 5.4	194.3 ± 5.0	269.8 ± 5.0
0015	00:14:19.43	-30:24:37.26	1.61	−4.7 ± 10.2	27.9 ± 6.4	37.7 ± 1.9	37.2 ± 2.3	38.9 ± 1.6	61.4 ± 2.3	68.7 ± 3.6	67.4 ± 3.5	65.9 ± 3.4

Table B.2: ALMA properties for first 10 selected LBG candidates. Full table available online

ID	Cluster	$F^{\mathrm{indiv,obs}}_{\mathrm{ALMA,peak,pbcor}}$ [c]	$rms^{\mathrm{indiv}}_{\mathrm{ALMA,pbcor}}$ [b]	$F^{\mathrm{indiv,obs,2-}\sigma\mathrm{lim}}_{\mathrm{ALMA,peak,pbcor}}$ [c]	SNR[d]	pbcor[e]
		[uJy]	[uJy]	[uJy]		
0001	A2744	59	68	195	0.87	0.81
0002	A2744	74	60	193	1.25	0.92
0004	A2744	179	62	303	2.87	0.88
0005	A2744	48	56	160	0.85	0.98
0007	A2744	57	56	170	1.01	0.98
0008	A2744	76	56	189	1.35	0.98
0012	A2744	5	98	201	0.05	0.56
0013	A2744	110	95	300	1.16	0.58
0014	A2744	127	66	259	1.91	0.83
0015	A2744	−5	56	113	−0.08	0.98

[a] Calculated from Eq. 2.8. [b] Obtained from with Eq. 2.9. [c] 2−σ upper limits for the ALMA observed fluxes (Eq. 2.11). [d] SNR = $F^{\mathrm{indiv,obs}}_{\mathrm{ALMA,peak,pbcor}}/rms^{\mathrm{indiv}}_{\mathrm{ALMA,pbcor}}$ [e] Primary beam correction for each position in `.flux` files.

Table B.3: Derived properties for first 10 selected LBG candidates. Full table available online

ID	β[a]	μ[b]	D_l[c] [Mpc]
0001	-1.60 ± 0.29	4.901	19310
0002	-2.20 ± 0.25	4.817	18430
0004	-2.28 ± 0.15	6.040	18620
0005	-1.69 ± 0.09	14.643	17550
0007	-1.92 ± 0.39	7.970	17260
0008	-3.18 ± 0.58	5.413	14500
0012	-1.60 ± 0.12	2.461	11090
0013	-2.55 ± 0.28	2.674	18920
0014	-1.85 ± 0.14	4.962	18530
0015	-1.95 ± 0.22	3.671	11900

[a] UV-slope calculated as stated in §2.6.

[b] Magnification factors following Coe et al. (2015) without capping.

[c] Luminosity distances after Wright (2006).

Table B.4: Properties obtained from FAST for first 10 selected LBG candidates. Values have been corrected for magnification factors. Full table available online

ID	$\log_{10}(M_\star/M_\odot)$	$\log(\mathrm{SFR}/\mathrm{M}_\odot\mathrm{yr}^{-1})$	$\log(\mathrm{sSFR}/\mathrm{yr}^{-1})$
0001	7.610	-0.380	-8.680
0002	7.287	-0.793	-8.763
0004	6.639	-0.701	-8.131
0005	7.204	0.224	-8.146
0007	6.799	-1.191	-8.891
0008	5.917	-1.063	-7.713
0012	8.359	-0.001	-8.751
0013	6.503	-0.847	-7.777
0014	7.934	-0.156	-8.776
0015	6.915	-0.065	-7.545

* Magnification-corrected values from FAST.

Table B.5: Luminosities from *HST* photometry and modified blackbody (graybody) spectrum for first 10 selected LBG candidates. Full table available online

ID	$\log(\mathrm{L}_{\mathrm{UV}}/\mathrm{L}_\odot)$	$\log(\mathrm{L}_{\mathrm{IR}}{}^{2-\sigma}/\mathrm{L}_\odot)$	$\log(\mathrm{L}_{\mathrm{IR}}{}^{2-\sigma}/\mathrm{L}_{\mathrm{UV}})$	$\log(\mathrm{F}_{\mathrm{UV}}/\mu\mathrm{Jy})$	$\log(\mathrm{F}_{\mathrm{IR}}{}^{2-\sigma}/\mu\mathrm{Jy})$
0001	8.834	12.206	3.372	-3.1350	-0.960
0002	8.876	12.227	3.351	-3.1041	-0.932
0004	8.821	12.416	3.595	-3.2076	-0.841
0005	8.969	12.168	3.199	-3.3973	-1.308
0007	8.310	12.203	3.893	-3.2906	-1.174
0008	8.317	12.333	4.016	-3.0395	-0.876
0012	9.268	12.473	3.205	-2.5782	-0.394
0013	8.888	12.403	3.515	-2.8614	-0.500
0014	9.225	12.351	3.126	-3.1196	-0.821
0015	8.541	12.194	3.653	-2.7823	-0.846

C

Detected LBG Candidates

Individual stamps from ALMA observations of the three LBG candidates which are considered as detected according to §2.10. Their properties are listed in Table 4.1.

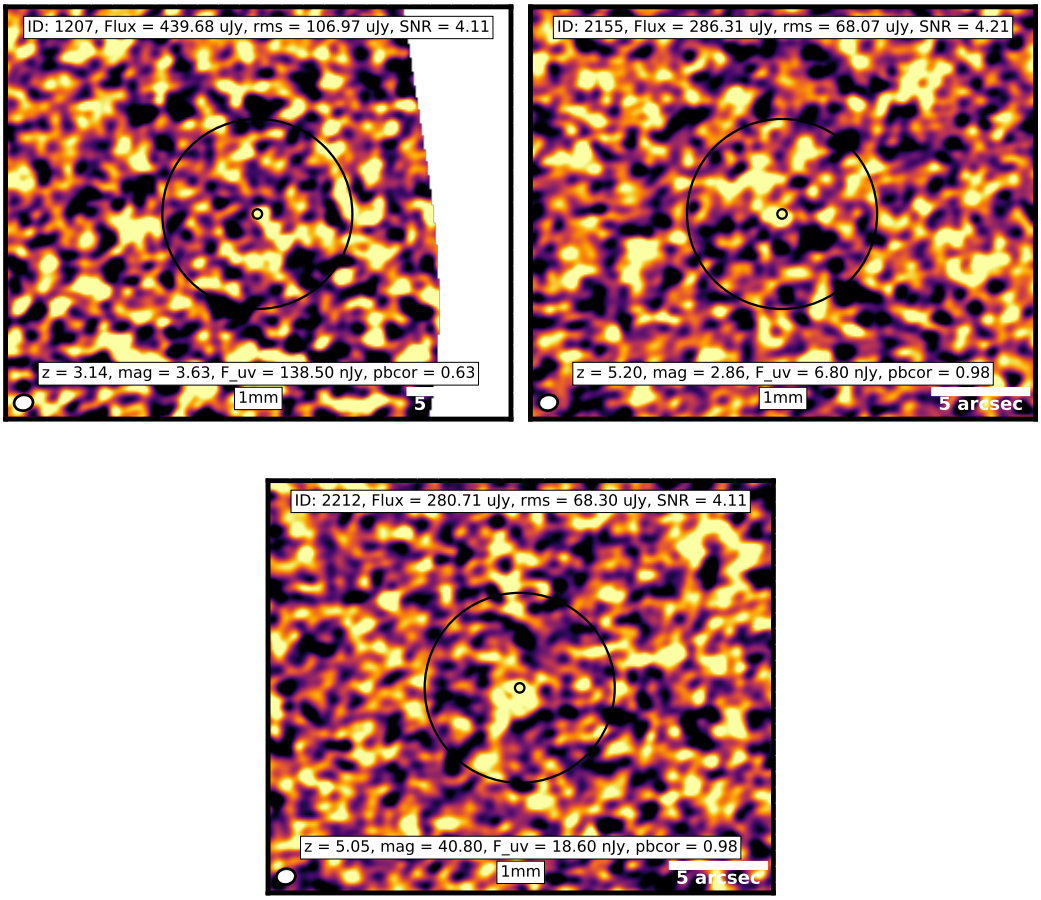

Figure C.1: Stamps of detected LBGs. Small circle in the middle shows area where source flux has been calculated. Large circle shows region of radius $5 \times b_{maj}$ where no other bright sources are expected. White ellipse in the lower-left corner shows primary beam size and bar in the lower-right corner shows scale of 5″.